Harvey, T, Conselice, CJ, Adams, NJ, Austin, D, Juodžbalis, I, Trussler, J, Li, Q, Ormerod, K, Ferreira, L, Lovell, CC, Duan, Q, Westcott, L, Harris, H, Bhatawdekar, R, Coe, D, Cohen, SH, Caruana, J, Cheng, C, Driver, SP, Frye, B, Furtak, LJ, Grogin, NA, Hathi, NP, Holwerda, BW, Jansen, RA, Koekemoer, AM, Marshall, MA, Nonino, M, Vijayan, AP, Wilkins, SM, Windhorst, R, Willmer, CNA, Yan, H and Zitrin, A

 EPOCHS. IV. SED Modeling Assumptions and Their Impact on the Stellar Mass Function at 6.5 ≤ z ≤ 13.5 Using PEARLS and Public JWST Observations

http://researchonline.ljmu.ac.uk/id/eprint/26251/

Article

For more information please contact researchonline@ljmu.ac.uk

https://doi.org/10.3847/1538-4357/ad8c29

EPOCHS. IV. SED Modeling Assumptions and Their Impact on the Stellar Mass Function at $6.5 \leqslant z \leqslant 13.5$ Using PEARLS and Public JWST Observations

Thomas Harvey[1], Christopher J. Conselice[1], Nathan J. Adams[1], Duncan Austin[1], Ignas Juodžbalis[1,2], James Trussler[1], Qiong Li[1], Katherine Ormerod[1,3], Leonardo Ferreira[4], Christopher C. Lovell[5], Qiao Duan[1], Lewi Westcott[1], Honor Harris[1], Rachana Bhatawdekar[6], Dan Coe[7], Seth H. Cohen[8], Joseph Caruana[9,10], Cheng Cheng[11,12], Simon P. Driver[13], Brenda Frye[14], Lukas J. Furtak[15], Norman A. Grogin[16], Nimish P. Hathi[16], Benne W. Holwerda[17], Rolf A. Jansen[8], Anton M. Koekemoer[16], Madeline A. Marshall[18,19], Mario Nonino[20], Aswin P. Vijayan[21,22,23], Stephen M. Wilkins[22], Rogier Windhorst[8], Christopher N. A. Willmer[24], Haojing Yan[25], and Adi Zitrin[26]

[1] Jodrell Bank Centre for Astrophysics, University of Manchester, Oxford Road, Manchester M13 9PL, UK
[2] Kavli Institute for Cosmology, University of Cambridge, Cambridge, Madingley Road, Cambridge, CB3 0HA, UK
[3] Astrophysics Research Institute, Liverpool John Moores University, 146 Brownlow Hill, Liverpool, L3 5RF, UK
[4] Department of Physics & Astronomy, University of Victoria, Finnerty Road, Victoria, British Columbia, V8P 1A1, Canada
[5] Institute of Cosmology and Gravitation, University of Portsmouth, Burnaby Road, Portsmouth, PO1 3FX, UK
[6] European Space Agency (ESA), European Space Astronomy Centre (ESAC), Camino Bajo del Castillo s/n, 28692 Villanueva de la Cañada, Madrid, Spain
[7] AURA for the European Space Agency (ESA), Space Telescope Science Institute, 3700 San Martin Drive, Baltimore, MD 21218, USA
[8] School of Earth and Space Exploration, Arizona State University, Tempe, AZ 85287-1404, USA
[9] Department of Physics, University of Malta, Msida MSD 2080, Malta
[10] Institute of Space Sciences & Astronomy, University of Malta, Msida MSD 2080, Malta
[11] Chinese Academy of Sciences South America Center for Astronomy, National Astronomical Observatories, CAS, Beijing 100101, People's Republic of China
[12] 2 CAS Key Laboratory of Optical Astronomy, National Astronomical Observatories, Chinese Academy of Sciences, Beijing 100101, People's Republic of China
[13] International Centre for Radio Astronomy Research (ICRAR) and the International Space Centre (ISC), The University of Western Australia, M468, 35 Stirling Highway, Crawley, WA 6009, Australia
[14] University of Arizona, Department of Astronomy/Steward Observatory, 933 N Cherry Avenue, Tucson, AZ 85721, USA
[15] Physics Department, Ben-Gurion University of the Negev, P. O. Box 653, Be'er-Sheva, 8410501, Israel
[16] Space Telescope Science Institute, 3700 San Martin Drive, Baltimore, MD 21218, USA
[17] Department of Physics and Astronomy, University of Louisville, 102 Natural Sciences Building, Louisville, KY 40292, USA
[18] National Research Council of Canada, Herzberg Astronomy & Astrophysics Research Centre, 5071 West Saanich Road, Victoria, BC V9E 2E7, Canada
[19] ARC Centre of Excellence for All Sky Astrophysics in 3 Dimensions (ASTRO 3D), Australia
[20] INAF-Osservatorio Astronomico di Trieste, Via Bazzoni 2, I-34124 Trieste, Italy
[21] Cosmic Dawn Center (DAWN), Denmark
[22] Astronomy Centre, Department of Physics and Astronomy, University of Sussex, Brighton, BN1 9QH, UK
[23] DTU-Space, Technical University of Denmark, Elektrovej 327, DK-2800 Kgs. Lyngby, Denmark
[24] Steward Observatory, University of Arizona, 933 N Cherry Avenue, Tucson, AZ 85721-0009, USA
[25] Department of Physics and Astronomy, University of Missouri, Columbia, MO 65211, USA
[26] Department of Physics, Ben-Gurion University of the Negev, P.O. Box 653, Be'er-Sheva 84105, Israel
Received 2024 March 6; revised 2024 September 13; accepted 2024 October 27; published 2024 December 26

Abstract

We utilize deep JWST Near Infrared Camera (NIRCam) observations for the first direct constraints on the Galaxy Stellar Mass Function (GSMF) at $z > 10$. Our EPOCHS v1 sample includes 1120 galaxy candidates at $6.5 < z < 13.5$ taken from a consistent reduction and analysis of publicly available deep JWST NIRCam data covering the Prime Extragalactic Areas for Reionization Science, CEERS, GLASS, JADES GOOD-S, NGDEEP, and SMACS0723 surveys, totaling 187 arcmin^2. We investigate the impact of spectral energy distribution fitting methods, assumed star formation histories (SFHs), dust laws, and priors on galaxy masses and the resultant GSMF. While our fiducial GSMF agrees with the literature at $z < 13.5$, we find that the assumed SFH model has a large impact on the GSMF and stellar mass density (SMD), finding a 0.75 dex increase in the SMD at $z = 10.5$ between a flexible nonparametric and standard parametric SFH. Overall, we find a flatter SMD evolution at $z \geqslant 9$ than some studies predict, suggesting a rapid buildup of stellar mass in the early Universe. We find no incompatibility between our results and those of standard cosmological models, as suggested previously, although the most massive galaxies may require a high star formation efficiency. We find that the "little red dot" galaxies dominate the $z = 7$ GSMF at high masses, necessitating a better understanding of the relative contributions of active galactic nucleus and stellar emission. We show that assuming a theoretically motivated top-heavy initial mass function (IMF) reduces stellar mass by 0.5 dex without affecting fit quality, but our results remain consistent with existing cosmological models with a standard IMF.

Unified Astronomy Thesaurus concepts: Galaxy counts (588); High-redshift galaxies (734); Lyman-break galaxies (979); Galaxy photometry (611); Galaxy masses (607)

1. Introduction

The James Webb Space Telescope (JWST) has pushed backed the redshift frontier when searching for the earliest galaxies. The highly sensitive Near Infrared Camera (NIRCam)

on JWST has led to an influx of high-redshift galaxy candidates through photometry, in surveys such as CEERS, GLASS, Prime Extragalactic Areas for Reionization Science (PEARLS), NGDEEP, and JADES (M. Castellano et al. 2022; N. J. Adams et al. 2023; D. Austin et al. 2023; R. A. Windhorst et al. 2023; M. B. Bagley et al. 2024; K. N. Hainline et al. 2024a). The wavelength coverage from 0.6 to 5 μm enables identification of Lyman-break galaxies at redshifts $z \geqslant 6.5$ by their photometry. In the first 18 months of science operations, tens of candidates above $z \geqslant 10$ have been identified (M. Castellano et al. 2022; R. P. Naidu et al. 2022a, 2022b; N. J. Adams et al. 2023; H. Atek et al. 2023; D. Austin et al. 2023; C. T. Donnan et al. 2023; S. L. Finkelstein et al. 2023, 2024; L. J. Furtak et al. 2023b; Y. Harikane et al. 2023; I. Labbé et al. 2023; G. C. K. Leung et al. 2023; P. G. Pérez-González et al. 2023; K. N. Hainline et al. 2024a; D. J. McLeod et al. 2024; C. J. Willott et al. 2024), including a spectroscopically confirmed galaxy at $z = 13.27$ (E. Curtis-Lake et al. 2023) and candidates at $z \geqslant 16$ (e.g., H. Atek et al. 2023; L. J. Furtak et al. 2023b; H. Yan et al. 2023; K. N. Hainline et al. 2024a).

An immediate result was a potential overabundance of high-redshift galaxies compared to theoretical predictions and extrapolations of Hubble Space Telescope (HST)/Spitzer results (M. Haslbauer et al. 2022; R. P. Naidu et al. 2022b; C. A. Mason et al. 2023; V. Mauerhofer & P. Dayal 2023). The mere existence of some of the galaxies at the inferred redshifts and stellar masses, ($\geqslant 10^{10.5} M_{\odot}$ at $z \geqslant 7.5$) seems to be in tension with standard ΛCDM cosmology, given the small areas currently probed with JWST (M. Boylan-Kolchin 2023; I. Labbé et al. 2023; C. C. Lovell et al. 2023; G. Desprez et al. 2024). However, spectroscopic observations of some of the highest-mass candidates in I. Labbé et al. (2023) have reduced their redshifts and stellar masses, or hinted at the presence of Active Galactic Nuclei (AGNs), and hence reduced possible ΛCDM tension (S. Fujimoto et al. 2023a; D. D. Kocevski et al. 2023). Massive ($\geqslant 10^{11} M_{\odot}$) quiescent galaxies at $z \approx 4$ also appear to challenge theories of galaxy evolution, given the old stellar populations implied by their star formation histories (SFHs; A. Carnall et al. 2024; C. M. Casey et al. 2024; K. Glazebrook et al. 2024).

Initial overlap of galaxy candidates between independent studies was poor, but has since improved due to agreement on photometric calibration and reduction techniques (M. J. Rieke et al. 2023; N. J. Adams et al. 2024). Spectroscopic confirmation exists only for a fraction of potential candidates, but most spectroscopic programs have had a high success rate, along with a few notable low-z interlopers (P. Arrabal Haro et al. 2023b; E. Curtis-Lake et al. 2023; S. Fujimoto et al. 2023b; B. E. Robertson et al. 2023; M. Tang et al. 2023; B. Wang et al. 2023; A. J. Bunker et al. 2024; I. H. Laseter et al. 2024).

The combination of NIRCam's high sensitivity and infrared (IR) wavelength coverage allows characterization of the rest-frame optical emission of $0.5 \leqslant z \leqslant 10$ galaxies, which is crucial for accurate stellar mass estimates. A more complete census of the high-redshift Universe is also possible, as galaxies without a strong Lyman-break (so called "HST-dark" galaxies) were often missed in the Ultraviolet (UV) selected samples of pre-JWST studies (P. G. Pérez-González et al. 2023). Observations with Spitzer IRAC were available only for the brightest sources, due to low sensitivity and angular resolution. Intrinsically UV-faint galaxies are often found to be

dusty or evolved systems, and accurate characterization of this population is essential when measuring the total buildup of stellar mass in the Universe, which is typically done by measuring the Galaxy Stellar Mass Function (GSMF).

Stellar masses are typically estimated from fitting spectral energy distributions (SEDs) to broadband photometry, and inferring an SFH along with other physical parameters such as metallicity, dust obscuration, and ionization state of the gas (e.g., J. Brinchmann & R. S. Ellis 2000; K. Bundy et al. 2006; A. Mortlock et al. 2011, 2015; K. Duncan et al. 2014; A. Grazian et al. 2015; M. Song et al. 2016; R. Bhatawdekar et al. 2019). This approach has generally been found to be reliable in the local Universe. At high redshift, there are a number of complicating factors that must be considered, which have different effects but overall act to increase the uncertainty in stellar masses beyond the statistical uncertainty from the fitting (S. Lower et al. 2020; B. Wang et al. 2024a). There is a growing consensus that the SFHs of many high-z galaxies are stochastic and characterized by repeated cycles of a short burst of rapid star formation followed by a temporary period of quiescence (C.-A. Faucher-Giguère 2018; Y. Asada et al. 2024; T. J. Looser et al. 2023; A. Dressler et al. 2024; T. Dome et al. 2024). Young, bright stars created in the most recent bursts of star formation can dominate the SEDs of galaxies and obscure older populations, a phenomenon known as "outshining," leading to the stellar mass being underestimated by up to 1 dex (R. Endsley et al. 2021; C. Giménez-Arteaga et al. 2023, 2024; C. Papovich et al. 2023; P. G. Pérez-González et al. 2023; S. Jain et al. 2024). For extremely stochastic SFHs, information loss for the first periods of star formation may occur, leading to large uncertainties in stellar mass (S. E. van Mierlo et al. 2023; X. Shen et al. 2023; D. Narayanan et al. 2024). Flexible "nonparametric" SFHs, such as those presented in J. Leja et al. (2019), S. Tacchella et al. (2022), and B. E. Robertson et al. (2023) are able to reproduce these bursty SFHs more accurately at high z, typically finding systematically larger stellar masses (C. Giménez-Arteaga et al. 2023; S. Jain et al. 2024), and may produce more reliable stellar mass estimates when compared to traditional parametric SFHs, which typically vary smoothly (e.g., delayed exponential; A. C. Carnall et al. 2019).

Another assumption is that of a possible universal initial mass function (IMF), which predicts the number of stars as a function of stellar mass (E. E. Salpeter 1955). The presence of low-mass stars, which dominate the stellar mass, is inferred entirely from the shape of the assumed IMF in most galaxies. A universal IMF (e.g., E. E. Salpeter 1955; G. Chabrier et al. 2000; P. Kroupa 2001), which is constant across time and space, has long been assumed in the majority of galaxy studies. Models of the the physics of high-z star formation suggest that it may have deviated from the universal IMF above redshift $z = 8$ (P. F. Hopkins et al. 2005; A. S. Jermyn et al. 2018; C. L. Steinhardt et al. 2021, 2023). Low metallicity, high star formation rates, an increasing CMB temperature, and high cosmic-ray density could all contribute to heating of star formation regions and lead to a top-heavy IMF at high redshift (M. L. P. Gunawardhana et al. 2011; P. P. Papadopoulos et al. 2011; B. Clauwens et al. 2016; E. R. Cueto et al. 2024). Observations of local elliptical galaxies have also found them to be inconsistent with the universal IMF, and instead find evidence for an IMF gradient, with evidence for a different IMF between younger and older stellar populations (e.g., C. Weidner et al. 2013; Z. Yan et al. 2021, and references

Table 1
Table Showing the Unmasked Areas and Depths of the Observations Used in This Work

Field	Area (arcmin^2)	HST/ACS_WFC		JWST/NIRCam								
		F606W	F814W	F090W	F115W	F150W	F200W	F277W	F335M	F356W	F410M	F444W
NEP	57.32	28.74	⋯	28.50	28.50	28.50	28.65	29.15	⋯	29.30	28.55	28.95
El Gordo*	3.90	⋯	⋯	28.23	28.25	28.18	28.43	28.96	⋯	29.02	28.45	28.83
MACS-0416*	12.3	⋯	⋯	28.67	28.62	28.49	28.64	29.16	⋯	29.33	28.74	29.07
CLIO*	4.00	⋯	⋯	28.12	⋯	28.07	28.21	28.675	⋯	28.91	⋯	28.71
CEERS	66.40	28.6	28.30	⋯	28.70	28.60	28.89	29.20	⋯	29.30	28.50	28.85
CEERSP9	6.08	28.31	28.32	⋯	29.02	28.55	28.78	29.20	⋯	29.22	28.50	29.12
SMACS-0723*	4.31	⋯	⋯	28.75	⋯	28.81	28.95	29.45	⋯	29.55	⋯	29.28
GLASS	9.76	⋯	⋯	29.14	29.11	28.86	29.03	29.55	⋯	29.61	⋯	29.84
NGDEEP HST-S	1.28	29.20	28.80	⋯	29.78	29.52	29.48	30.28	⋯	30.22	⋯	30.22
NGDEEP HST-D	4.03	30.30	30.95	⋯	29.78	29.52	29.48	30.28	⋯	30.22	⋯	30.22
JADES Deep GS	22.98	29.07	⋯	29.58	29.78	29.68	29.72	30.21	29.58	30.17	29.64	29.99

Notes. Depths are given at 5σ in AB magnitudes, measured in $0''16$ radius apertures. Depths are calculated by placing nonoverlapping apertures in empty regions of the image, as measured by the SExtractor segmentation maps and our image masks. The nearest 200 apertures are used to calculate the normalized mean absolute deviation to derive local depths for each individual source. Where depths are tiered across mosaics (e.g., HST Advanced Camera for Surveys Wide Field Channel observations in the Hubble Ultra Deep Field Parallel 2), we have listed the depths and areas separately. The four spokes of the NEP-TDF and 10 CEERS pointings have uniform depths (within 0.1 mag) with the exception of CEERS P9, which we list separately. Areas are given in arcmin^2 and measured from the mask to account for the masked areas of the image and unused cluster modules. Fields marked with an asterisk ("*") indicate that we have excluded the NIRCam module containing a lensing cluster from our analysis.

therein). Studies such as T. Jeřábková et al. (2018), C. L. Steinhardt et al. (2023), A. Sneppen et al. (2022), C. Woodrum et al. (2023), and E. R. Cueto et al. (2024) have introduced temperature/time-dependent IMF models for use in SED fitting, which can decrease stellar mass estimates by up to 1 dex at constant redshift. Constraining the IMF is extremely difficult, but recent studies are beginning to find possible evidence for a top-heavy IMF in the early Universe (e.g., H. Katz et al. 2022; A. J. Cameron et al. 2024; L. Mowla et al. 2024). Ultimate conclusions on this are, however, far from certain.

In the EPOCHS paper series, we have presented an independent and consistent reduction of deep JWST observations from available GTO, GO, and ERS data, including the CEERS, GLASS, SMACS-0723, JADES, and PEARLS fields. We found 1165 robust galaxy candidates above redshift $z = 6.5$, with a total area of 187 arcmin^2 (N. J. Adams et al. 2024; C. J. Conselice et al. 2024).

In this paper, we present a detailed examination of the inferred physical parameters of our high-redshift sample, with a particular focus on the stellar mass of our galaxy candidates. We derive a GSMF at $6.5 \leqslant z \leqslant 13.5$, and estimate the stellar mass density (SMD) in order to trace the buildup of stellar mass in the early Universe. Importantly, we explore the impact of some of the key assumptions used in deriving stellar masses at high redshifts, such as SFHs and the IMF.

In Section 2, we present a brief overview of the data products used in this work and detail our data reduction procedure. Section 3 describes our process for catalog creation and robust sample selection of high-z galaxy candidates. We detail our SED-fitting procedure and the impact of different assumptions on the inferred properties of high-z galaxies in Section 4. In Section 5, we use our stellar mass estimates to build on the UV luminosity function presented in N. J. Adams et al. (2024) and construct a GSMF at redshifts from $6.5 \leqslant z \leqslant 13.5$. We discuss our findings and make comparisons to the literature in Section 6. Finally,

Section 7 summarizes the findings of this work and looks at possibilities for future studies.

We assume a standard ΛCDM cosmology with $H_0 = 70 \text{ km s}^{-1} \text{ Mpc}^{-1}$, $\Omega_M = 0.3$, and $\Omega_\Lambda = 0.7$. All magnitudes listed follow the AB magnitude system (J. B. Oke 1974; J. B. Oke & J. E. Gunn 1983). All stellar masses measured in this work use a P. Kroupa (2002) IMF unless otherwise indicated.

2. Products and Data Reduction

This section briefly details the JWST programs and data products used in this analysis. For further details on the fields used, please see D. Austin et al. (2023), N. J. Adams et al. (2024), and C. J. Conselice et al. (2024). Table 1 shows the available unmasked areas, JWST NIRCam filters, and 5σ depths of each data set used.

2.1. PEARLS

We incorporate NIRCam observations from the proprietary GTO survey PEARLS (PI: R. Windhorst & H. Hammel, PID: 1176 & 2738, R. A. Windhorst et al. 2023). We use observations of three fields targeting gravitationally lensed clusters, and one blank field consisting of a mosaic of eight JWST NIRCam pointings. The gravitationally lensed clusters consist of MACS J0416.1-2403 (hereafter referred to as MACS-0416), El Gordo ($z \sim 0.87$, ACT-CL J0102-4915 in the Atacama Cosmology survey (F. Menanteau et al. 2012) and Clio $z \sim 0.42$, Designation GAMA100050 in the GAMA Galaxy Group Catalog v6+ (A. S. G. Robotham et al. 2011)). El Gordo and Clio have been visited once with JWST/NIRCam, with the cluster centered in one NIRCam module and the other observing a neighboring blank field $\sim 3'$ away (A. Griffiths et al. 2018). MACS-0416 has been observed three times, resulting in three separate parallel observations at different position angles. The PEARLS blank field is the North Ecliptic Pole Time Domain Field (R. A. Jansen & R. A. Windhorst 2018, NEP-TDF). The NEP-TDF is positioned so it can be observed throughout the year, making

it ideal for time-domain science and constructing a large deep field. Observations of the NEP-TDF consist of four pairs of overlapping NIRCam pointings (eight pointings total), with each of these four pairs oriented at 90° intervals like spokes on a windmill. NIRCam observations of the NEP-TDF, El Gordo and MACS0416 use the standard eight photometric bands; F090W, F115W, F150W, F200W, F277W, F356W, F410M, and F444W. Clio uses six of the eight previous bands, but lacks F115W and F410M. Within the NEP-TDF field, we incorporate HST Advanced Camera for Surveys Wide Field Channel (ACS/WFC) imaging in the F606W filter, collected as part of the GO-15278 (PI: R. Jansen) and GO-16252/16793 (PIs: R. Jansen & N. Grogin) surveys between 2017 October 1 and 2022 October 31. Mosaics of these data, astrometrically aligned to Gaia/DR3 and resampled on 0″03 pixels, were made available before publication by R. Jansen & R. O'Brien (2024, private communication; R. O'Brien et al. 2024). For full details of the PEARLS program, please see R. A. Windhorst et al. (2023).

2.2. ERS and GO Data

We incorporate Early Release Science (ERS) and public General Observer (GO) data from SMACS-0723 (PID: 2736, PI: K. Pontoppidan; K. M. Pontoppidan et al. 2022), the Cosmic Evolution Early Release Science Survey (CEERS; PID: 1345, PI: S. Finkelstein; see also M. B. Bagley et al. 2023a), the Grism Lens Amplified Survey from Space survey (GLASS; PID: 1324, PI: T. Treu; T. Treu et al. 2023) and the Next Generation Deep Extragalactic Exploratory Public Survey (NGDEEP; PID: 2079, PIs: S. Finkelstein, Papovich and Pirzkal; M. B. Bagley et al. 2024). We incorporate HST ACS/WFC observations of the Extended Groth Strip (M. Davis et al. 2007) into our CEERS data set in the F606W and F814W filters. This was obtained as part of the Cosmic Assembly Near-infrared Deep Extragalactic Legacy Survey (CANDELS; N. A. Grogin et al. 2011; A. M. Koekemoer et al. 2011), with updated astrometric alignment to Gaia EDR3 (A. G. Brown et al. 2021) by the CEERS team[27] and released as Hubble Data Release 1. The addition of these observations compensates for the lack of F090W observations in the CEERS survey.

We also incorporate NIRCam imaging of the Great Observatories Origins Deep Survey South (GOODS-South) field collected as part of JWST Advanced Deep Extragalactic Survey (JADES; PI: D. Eisenstein; D. J. Eisenstein et al. 2023b) and released publicly as JADES DR1 (M. J. Rieke et al. 2023). In the JADES and NGDEEP fields, which lie on the GOODS-South footprint, we add in existing HST data from F606W and F814W from the most recent mosaic (v2.5) from the Hubble Legacy Fields team (G. Illingworth et al. 2016; K. E. Whitaker et al. 2019).

2.3. JWST NIRCam Data Reduction

We have uniformly reprocessed all lower-level JWST data products following our modified version of the official JWST pipeline. This is a process similar to that used in L. Ferreira et al. (2022), N. J. Adams et al. (2023), D. Austin et al. (2023), and in particular N. J. Adams et al. (2024), but with updates based on new flat-fielding and techniques for dealing with NIRCam imaging artifacts.

We use version 1.8.2 of the official STScI JWST Pipeline[28] (H. Bushouse et al. 2022) and Calibration Reference Data System (CRDS) v1084, which contains the most up-to-date NIRCam calibrations at the time of writing and includes updated flat-field templates for the LW detectors, resulting in improved average depths across a single pointing of ∼0.2 dex in F444W. Next, we subtract templates of wisps, artifacts present in the F150W and F200W imaging, between stage 1 and stage 2 of the pipeline. After stage 2 of the pipeline, we apply the $1/f$ noise correction derived by Chris Willott,[29] which removes linear features caused by read noise from the images. We do not use the sky subtraction step included in stage 3 of the pipeline, instead performing background subtraction on individual NIRCam frames between stage 2 and stage 3 ("cal.fits" files), consisting of an initial uniform background subtraction followed by a two-dimensional background subtraction using photutils (L. Bradley et al. 2022). This allows for quicker assessment of the background subtraction performance and immediate fine-tuning of configuration parameters. After stage 3 of the pipeline, we align the final F444W image onto a Gaia-derived World Coordinate System (WCS; Gaia Collaboration et al. 2018; A. Vallenari et al. 2023) using tweakreg, part of the DrizzlePac Python package,[30] and then match all remaining filters to this derived WCS, ensuring the individual images are aligned to one another. In some cases (NEP and CEERS), we match to a WCS frame derived from other space- or ground-based imaging with a larger FOV, given the low number of Gaia stars in some individual NIRCam pointings. We then pixel-match the images to the F444W image with the use of astropy/reproject (Astropy Collaboration et al. 2013, 2022; S. L. Hoffmann et al. 2021).[31] The final resolution of the drizzled images is 0″03/pixel. Comparison of our reduction to the official PEARLS reduction pipeline (R. A. Windhorst et al. 2023) is given in N. J. Adams et al. (2024), finding excellent agreement in both observed fluxes (within 0.03 (0.01) mag in the blue (red) NIRCam photometric filters) and astrometry (within 2 pixels (0″07)).

3. Catalog Creation and Sample Selection

Full details of our catalog creation and sample selection pipeline, called GALFIND, is available in C. J. Conselice et al. (2024). We briefly summarize the procedure used here.

3.1. Catalog Creation

We use the code SExtractor (E. Bertin & S. Arnouts 1996) for source identification and photometric measurements. We use an inverse-variance-weighted stack of the NIRCam F277W, F356W, and F444W images for source detection in order to reliably identify faint sources and then carry out forced-aperture photometry in all photometric bands. This photometry is calculated within 0″32 diameter circular apertures, correcting for the aperture size with an aperture correction derived from simulated WebbPSF point spread functions (PSFs) for each band used (M. D. Perrin et al. 2012, 2014). This diameter was chosen to enclose the central/brightest 70%–80% of the flux of a point source without a large

[27] https://ceers.github.io/hdr1.html
[28] https://github.com/spacetelescope/jwst
[29] https://github.com/chriswillott/jwst
[30] https://github.com/spacetelescope/drizzlepac
[31] https://reproject.readthedocs.io/en/stable/

amount of contamination from neighboring sources. This reduces the reliance on a potentially uncertain PSF model while still using the brightest pixels when calculating fluxes.

We choose not to PSF homogenize our imaging, and instead rely on a band-dependent aperture correction to account for the changing PSF. Other studies have shown that the WebbPSF can underestimate the broadening of the PSF at small scales (e.g., T. Morishita et al. 2024; J. R. Weaver et al. 2024), and measuring an empirical PSF is extremely difficult in some of our fields, given both the limited number of isolated stars in single-pointing fields (e.g., NGDEEP, El Gordo, or CLIO), as well as the PSFs being more complex and position-dependent due to the stacking of exposures taken at different times and position angles (e.g., NEP and MACS-0416). In the JADES-Deep-GS field, we tested whether not PSF-matching had a systematic impact on the derived fluxes or the galaxy properties derived from SED fitting. We repeated our full analysis of this field, using PSF-matched imaging, and using PSF models and kernels derived following the methodology of J. R. Weaver et al. (2024) and K. A. Suess et al. (2024), finding very little impact (<0.05 mag) on the resultant aperture fluxes across all bands, which is well within the 10% flux uncertainty floor used when SED fitting.

As SExtractor requires all images to be on the same pixel grid, for aligned HST imaging on a different pixel grid, we use photutils to perform forced-aperture photometry in apertures of the same diameter (L. Bradley et al. 2022).

We next produce masks for our images by eye to cover diffraction spikes, any remaining snowballs, the cross pattern between SW detectors, image edges (including a ~50–100 pixel border around detector edges), and any large foreground galaxies. The total amount of unmasked area used in this study is listed alongside the average 5σ depths of each field in Table 1.

Following the generation of source catalogs and segmentation maps for each image, we calculate local depths for each source in each filter. This accounts for variation in background and noise across the image. Apertures of $0\farcs32$ diameter are placed in empty regions of the image, as calculated from the segmentation map to be $\geqslant 1''$ from the nearest source. For each source, the nearest 200 apertures are used to calculate the normalized mean absolute deviation of the fluxes measured in the apertures, which corresponds to the 1σ flux uncertainty. We convert this to a 5σ depth, displaying the average depth in AB magnitudes for each field in Table 1. Where fields consist of mosaics of multiple pointings, we display the average depth across the entire field, but we note that 9/10 CEERS pointings and 4/4 NEP-TDF have depths consistent within 0.1 mag. The exception in CEERS is pointing 9 (P9), which has an additional exposure in F115W and F444W, resulting in increased depths of ~0.2 mag (N. J. Adams et al. 2024). Due to correlated noise, the flux uncertainties calculated by SExtractor are underestimated (E. Schlawin et al. 2020). We replace these uncertainty estimates with the local-depth-derived flux errors (N. J. Adams et al. 2024).

3.2. Sample Selection

To select a sample of high-redshift galaxies, we introduce selection criteria based primarily on photometric SED fitting with EAZY-py (G. B. Brammer et al. 2008). We aim to select a robust sample of galaxies above $z \geqslant 6.5$, where the Lyman break is within the NIRCam F090W filter.

We use the default EAZY templates (tweak_fsps_QSF_12_v3), along with Set 1 and Set 4 of the SED templates generated by R. L. Larson et al. (2023). These additional templates were developed to have bluer rest-frame UV colors than the default templates, as well as stronger emission lines, both of which have been observed in high-redshift galaxies (S. L. Finkelstein et al. 2022; F. Cullen et al. 2023; T. Nanayakkara et al. 2023; S. Withers et al. 2023). These templates have young stellar populations, low metallicities, and active star formation. R. L. Larson et al. (2023) have shown that they improve the accuracy of photo-z estimates at high redshift.

We run EAZY-py initially with a uniform redshift prior of $0 \leqslant z \leqslant 25$, but then repeat the fitting with a reduced upper redshift limit of $z \leqslant 6$. This allows us to compare the goodness of fit of both a high- and a low-redshift solution for all galaxies in our sample. We use a minimum flux uncertainty of 10% to account for uncertainties in flux calibrations and aperture corrections (M. J. Rieke et al. 2023), as well as potential differences between the synthetic templates and our galaxies.

For reproducibility, our selection criteria are designed to be based as much as possible on specific cuts in computed quantities, rather than individual inspection of candidates, which can introduce hard-to-measure bias and incompleteness. To ensure robustness in our sample, our final selection criteria includes a visual review of the cutouts and SED-fitting solutions for all sources by authors T.H., D.A., N.A., and Q.L., but we reject less than 5% of our original sample by eye at this stage, which is much lower than comparable studies (reaching $\geqslant 50\%$ in some cases; e.g., K. N. Hainline et al. 2024a).

Our selection criteria for robust high-redshift galaxies are as follows.

1. We require that the bandpass of the lowest-wavelength photometric band must be entirely below the Lyman break, given the primary photo-z solution. This sets a lower limit of $z \approx 6.5$ in most of our fields.

2. We require a $\leqslant 3\sigma$ detection in band(s) blueward of the Lyman break.

3. We require a $\geqslant 5\sigma$ detection in the two bands directly redward of the Lyman break, and $\geqslant 2\sigma$ detection in all other redward bands, excluding observations in NIRCam medium bands (e.g., F335M and F410M). If the galaxy appears only in the long-wavelength NIRCam photometry (i.e., a F200W or higher dropout), we increase the requirement on the first band to 7σ detection.

4. The integral of the photo-z PDF is required to satisfy $\int_{0.90 \times z_{\rm phot}}^{1.10 \times z_{\rm phot}} P(z)\, dz \geqslant 0.6$, to ensure the majority of the redshift PDF is located within the primary peak and that the peak is sufficiently narrow to provide a strong constraint on the redshift. $z_{\rm phot}$ refers to the redshift with maximum likelihood from the EAZY-py redshift posterior.

5. We require the best-fitting EAZY-py SED to satisfy $\chi^2_{\rm red} < 3(6)$ to be classed as a robust (good) fit.

6. We require a difference of $\Delta\chi^2 \geqslant 4$ between the high-z and low-z EAZY-py runs. This ensures that the high-z solution is much more statistically probable.

7. If the half-light radius (FLUX_RADIUS parameter in SExtractor) is smaller than the FWHM of the PSF in the F444W band, then we require that $\Delta\chi^2 \geqslant 4$ between the best-fitting high-z galaxy solution and the best-fitting brown dwarf template. This requirement is designed to

remove Milky Way brown dwarf contaminants and is discussed further in Section 5.2.2.

8. We require the 50% encircled flux radius from SEx-tractor to be $\geqslant 1.5$ pixels in the long-wavelength wideband NIRCam photometry (F277W, F356W, and F444W). This avoids the selection of oversampled hot pixels in the LW detectors as F200W dropouts.

Given our requirement to observe the Lyman break, the lowest redshift at which we select "robust" galaxies with NIRCam photometry only is ~6.5, where the break falls within the NIRCam F090W filter. In the fields where HST ACS/WFC imaging is available, we can robustly identify the Lyman break at lower redshifts.

Our selection criteria are similar to other high-z galaxy studies, such as those of K. N. Hainline et al. (2024a), S. L. Finkelstein et al. (2023, 2024), R. P. Naidu et al. (2022b), and M. Castellano et al. (2022), who also fit galaxies using EAZY-py and select their samples using the rest-UV signal-to-noise ratio (SNR) of their candidates and the resultant redshift PDF and $\Delta\chi^2$ from the SED fitting. The $\Delta\chi^2 \geqslant 4$ requirement was chosen to ensure that the high-z solution is a better fit than any possible low-z explanation, and is consistent with the criteria used in other studies, such as S. L. Finkelstein et al. (2024). SNR requirements vary between studies, and are also somewhat dependent on the size of the extraction aperture used. Our $0.''16$ radius apertures are larger than the $0.''1$ radius apertures used in S. L. Finkelstein et al. (2024), resulting in a number of their candidates being removed from our sample because they do not meet our 5σ threshold, despite agreeing on the photo-z solution. Other studies, such as as Y. Harikane et al. (2023) and H. Yan et al. (2023), use a combination of color–color cuts and SED-fitting. A comprehensive comparison of the EPOCHS v1 galaxy sample to other studies is given in Appendix A of N. J. Adams et al. (2024).

Spectroscopy of high-redshift galaxies with NIRSpec (e.g., E. Curtis-Lake et al. 2023; S. Fujimoto et al. 2023b; B. Wang et al. 2023; A. J. Bunker et al. 2024) has shown that many high-redshift galaxies have strong emission lines, with Hβ +[O III] reaching observed equivalent widths of up to 2000–3000 Å (S. Withers et al. 2023). For our photometric observations, this can result in an excess in the band covering these emission lines of up to ~1 dex. The emission-line modeling in the SED-fitting codes used spans only a limited parameter space in equivalent width and line ratios, so this can result in high χ^2 values even if the model is a good fit to the rest of the photometry. To avoid removing these galaxies from our sample, we introduce a secondary group, referred to as "good" galaxies, which have $3 < \chi_r^2 < 6$ but meet the rest of our criteria. This applies to a very small fraction of our total sample, with only 23 galaxies meeting our other selection criteria but falling within this χ^2 range.

4. Galaxy Properties from SED Fitting

The basic properties, redshift distribution, number counts, and UVJ colors of the EPOCHS v1 sample are described in detail in C. J. Conselice et al. (2024). The UV properties (M_{UV} and β slopes) of this sample are explored in D. Austin et al. (2024). The UV luminosity function is presented in N. J. Adams et al. (2024), Here, we briefly summarize the basic statistics of the EPOCHS v1 sample, following the selection criteria described in Section 3.2.

For full transparency, we list the number of candidate objects removed by each stage of our selection criteria as follows. We note that, as we apply all our selection criteria to all galaxies, each object can fail multiple selection criteria. Across all the survey fields used, the parent sample consists of 211,469 objects that are unmasked in all available photometric bands. Of these, only 1545 have photometric redshifts between $6.5 \leqslant z \leqslant 13.5$ and also pass the SNR criteria (criteria 1–3, above). Thirty-two are removed because they fail criterion 4, as the photo-z is not well constrained. Nine are removed by criterion 5, as the χ^2 suggests that the best-fitting SED does not reproduce the observed photometry. Three hundred and thirty-three are removed by criterion 6, which requires that the high-z solution has a robust statistical improvement when compared with the low-z ($z < 6.5$) solution. Sixty-three brown dwarfs are identified and removed from the sample by criterion 7, which is discussed further in Section 5.2.2. Finally, five hot pixels that have unphysically small sizes are removed by criterion 8. Accounting for the 49 galaxies that fail multiple of the preceding criteria, this leaves 1214 galaxies that pass our initial selection criteria with $z \geqslant 6.5$ over a total unmasked area of 187.27 arcmin^2, comprising one of the largest samples of high-z JWST-selected galaxies.

Our requirement constraining the redshift PDF is important for confident photo-z values and does not significantly bias our sample, as only seven galaxies of the full parent sample are rejected for this reason alone, and visual inspection of these seven objects shows they have SNR < 10 and physically implausible SEDs.

Our visual inspection removes 49 completely, leaving 1165 galaxies, which we refer to as the EPOCHS v1 sample. Of these 1165, 1054 are classed as "certain" and 111 as "uncertain" by our visual inspection. In this work, we choose to include the visually "uncertain" candidates, in order to avoid potentially underestimating the stellar mass function. Filtering the sample to the $6.5 < z < 13.5$ redshift range used in this work, our fiducial sample consists of 1120 galaxies.

The next sections detail the Bagpipes and Prospector SED fitting performed for all galaxies in the EPOCHS v1 sample. We perform this SED fitting only for our EAZY-py-selected sample. The purpose of this SED fitting is to analyze the properties of the stellar and nebular components of these high-z galaxies. We note that, while the majority of galaxies in the EPOCHS v1 sample do not appear significantly extended beyond our SExtractor extraction aperture, all stellar masses quoted in the following results have been corrected by the ratio between the SExtractor *FLUX_AUTO_F444W* and the aperture-corrected *FLUX_APER_F444W* fluxes, if it exceeded unity, to account for any residual flux outside the aperture. We use the longest-wavelength band to correct stellar masses, as this is most representative of the rest-frame optical emission. We choose to perform all SED fitting using aperture fluxes, which ensures flux is measured from the same aperture in all filters and avoids catastrophic issues with the SExtractor Kron aperture estimates, which sometimes become unphysically small or large. Some studies (e.g., K. A. Suess et al. 2024) calculate total fluxes by scaling all the overall normalization of all fluxes by the ratio between a Kron and aperture flux in a detection or reference band. This has no impact on the inferred galaxy colors, as SED fitting depends on the measured colors to infer the SFH and other parameters, and the total stellar mass simply scales linearly with the

Table 2
Summary of Parameters, Hyperparameters, and Priors for Our `Bagpipes` SED Fitting

Common Parameters		
Parameter	Prior/Value (Min, Max)	Description
z_{phot}	`EAZY-py` Posterior PDF ($\pm 3\sigma$)	Redshift
SPS Model	G. Bruzual & S. Charlot (2003); BPASS v2.2.1	Stellar population synthesis model
IMF	P. Kroupa (2001); default BPASS IMF	Stellar IMF
Dust-law Parameterization	D. Calzetti et al. (2000), S. Salim et al. (2018)	Dust law
	S. Charlot & S. M. Fall (2000)	
A_V	Log-uniform: (10^{-3}, 10); uniform (0, 6)	V-band attenuation (all stars)
SFH	Log-normal; "continuity bursty"; delayed-τ	Star formation history
$\log_{10}(M_\star/M_\odot)$	Uniform: (5, 12)	Surviving stellar mass
$Z_\star/Z_\odot$	Log-uniform: (0.005, 5); uniform (0, 3)	Stellar metallicity
$Z_{gas}/Z_\odot$	Fixed to $Z_\star$	Gas-phase metallicity
$\log_{10} U$	Uniform: (-3, -1)	Ionization parameter

Model Specific Parameters			
Model	Parameter	Prior/Value (Min, Max)	Description
Fiducial	t_{max}	Uniform: (10 Myr, 15 Gyr)	Age of Universe at peak SFR
	FWHM	Uniform: (10 Myr, 15 Gyr)	FWHM of SFH
Delayed-τ SFH	τ	Uniform: (10 Myr, 15 Gyr)	e-folding timescale
	Age	Log-uniform: (10 Myr, $t_{univ}(z_{phot})$)	Time since SF began
"Continuity Bursty"	N_{bins}	Six bins (five fitted parameters)	First bin 0–10 Myr, SF begins at $z = 20$,
Nonparametric SFH			others distributed equally in $\log_{10}$ lookback time
	$d_{\log_{10}SFR}$	Student's t: $\nu = 2$, $\sigma = 1.0$	Ratio of $\log_{10}$SFR in adjacent bins, coupled by σ
S. Charlot & S. M. Fall (2000)	n	Clipped normal: $\mu = 0.7$, $\sigma = 0.3$	Power-law slope of attenuation curve ($A \propto \lambda^{-n}$)
Dust Law		(0.3, 2.5)	For D. Calzetti et al. (2000) $n \approx 0.7$
	η	clipped normal: $\mu = 2$, $\sigma = 0.3$	$A_{V, <10~Myr}/A_V$ ratio between young and old stars
		(1, 3)	
S. Salim et al. (2018) Dust Law	δ	Clipped normal: $\mu = 0$, $\sigma = 0.1$	Deviation from D. Calzetti et al. (2000) slope
		(-0.3, 0.3)	
	β	Uniform (0, 5)	Strength of 2175 Å bump
BPASS SPS Model			No additional components
Uniform A_V Prior			No additional components
Uniform $Z_\star$ Prior			No additional components

Notes. Parameters and priors for other iterations can be assumed to be the same as given for the "fiducial" bagpipes run unless otherwise specified. The top section of the table lists parameters that are common to all of our `Bagpipes` models, whereas the lower section gives the model-specific parameters for each of our chosen configurations.

normalization. Our tests using the JADES-Deep-GS field, in which we repeat our full catalog creation, selection, and SED-fitting procedure on PSF-matched imaging with "TOTAL" fluxes, finds resultant stellar masses consistent to within a mean (median) offset of 0.03 (0.01) dex. Given that this is well within the statistical uncertainty of our stellar mass estimates, we find that our methodology of using a per-band aperture correction and aperture-corrected stellar masses is completely consistent with the results of comparable studies.

4.1. Bagpipes

`Bagpipes` (A. C. Carnall et al. 2018, 2019) is a Python package that uses Bayesian methods to fit galaxy SEDs to photometry. Our fiducial `Bagpipes` run uses the G. Bruzual & S. Charlot (2003) 2016 stellar population synthesis models and a P. Kroupa (2001) IMF.

`Bagpipes` can construct and fit SEDs with a variety of SFH models, dust models, and priors. We perform multiple fits for each galaxy in order to test the consistencies in derived galaxy parameters. For simplicity, our approach is to define an initial "fiducial" model, and then swap out individual model components or priors for other choices. Our model parameters, priors, and hyperparameters are detailed in Table 2. This is

similar to the approach of L. J. Furtak et al. (2021), who define a reference model that is then compared to alternative models. In the rest of this section, we further explain our choices of models and priors.

For the SFH, we test both parametric and nonparametric models, which have been shown to impact the stellar mass estimates (J. Leja et al. 2019; S. Tacchella et al. 2022). For our fiducial model, we use a parametric log-normal SFH, which allows us to recreate the rising SFHs we expect in the early Universe. We compare this SFH with another commonly used parameterization, the delayed exponential. Details of the implementation of these parametric SFHs are available in A. C. Carnall et al. (2019). We also test a nonparametric "continuity" SFH model similar to the model added to `Prospector` in J. Leja et al. (2019). This SFH model fits the star formation rates in fixed time bins, with $\Delta \log$ SFR between bins linked by a Student's t-distribution. We recreate the methodology of S. Tacchella et al. (2022) by fitting both a "continuity" model, where the Student's t-distribution has hyperparameters $\sigma = 0.3$ and $\nu = 2$, which weights against rapid changes in star formation rate, as well as a "continuity bursty" model, with $\sigma = 1$ and $\nu = 2$, which allows more stochastic star formation, with rapid bursts and quenching more similar to the SFH inferred at high-z. As is done in S. Tacchella et al. (2022), we fit six SFH bins for both models, with the

first bin fixed to a lookback time of 0–10 Myr, the last bin ending at $z = 20$, and the other four bins equally log-spaced in lookback time. J. Leja et al. (2019) showed that this model is relatively insensitive to the number of bins used, as long as it is more than four. Like S. Tacchella et al. (2022), we assume there is no star formation at $z > 20$ (J. D. Bowman et al. 2018; J. Jaacks et al. 2019; S. Tacchella et al. 2022). It is important to note that this model allows but does not require "bursty" SFHs, and smooth or quenched SFHs are also possible if favored during the fitting.

We include emission lines and nebular continuum based on CLOUDY v17.03 (G. J. Ferland et al. 2017). We regenerate CLOUDY models in order to probe a wider range of the ionization parameter U between $-3 \leqslant \log_{10} U \leqslant -1$ using a CLOUDY configuration file distributed with Bagpipes.

We use the D. Calzetti et al. (2000) prescription for dust. R. A. A. Bowler et al. (2024) find that UV-selected high-z galaxies in the ALMA REBELS survey follow the local Calzetti-like IRX-β relation, so we do not fit a more complex dust law in our fiducial model. The allowed stellar metallicity ranges from $-2.3 \leqslant \log_{10} Z_\star/Z_\odot \leqslant 0.70$ with a logarithmic prior, as these galaxies are expected to have low metallicity, but theoretically could enrich their local environments quickly (M. Curti et al. 2023; D. Langeroodi et al. 2023).

In order to constrain the redshift parameter space, we fix the redshift prior to the PDF from our EAZY-py SED-fitting, which we approximate as a Gaussian. The redshift prior draws are capped at $\pm 3\sigma$. We use the default sampling method, using the Python package PyMultiNest (F. Feroz et al. 2009; J. Buchner 2014).

4.2. Prospector

In addition to our Bagpipes SED fitting, we also fit our sample using the Prospector package (B. D. Johnson et al. 2021) in order to compare the results of these two commonly used SED-fitting tools. Prospector allows greater flexibility and control of model parameters than Bagpipes, at the expense of computational time. Prospector uses Bayesian inference to determine galaxy stellar population properties and SFHs. Prospector is built on Flexible Stellar Population Synthesis (FSPS; C. Conroy & J. E. Gunn 2010), using python-fsps (B. Johnson et al. 2024) and the Modules for Experiments in Stellar Astrophysics Isochrones and Stellar Tracks (MIST) stellar isochrones (J. Choi et al. 2016; A. Dotter 2016). Prospector allows for very flexible SFHs, including the use of nonparametric SFHs, which have become increasingly popular in the JWST era. We generally follow the prescription of S. Tacchella et al. (2022) for our Prospector model. We test both a traditional parametric SFH as well as the "continuity bursty" nonparametric SFH used in Bagpipes. We allow the stellar mass to vary between $6 \leqslant \log_{10} M/M_\odot \leqslant 12$ with a uniform logarithmic prior. For our parametric SFH, we use the "delayed-τ" model, where $\text{SFR}(t) \propto (t - t_s)e^{-(t-t_s)\tau}$.

We note that, by default, Prospector provides the total stellar mass formed, rather than the surviving stellar mass. After fitting, we recalculate the return fraction within Prospector for the full posterior in order to derive a surviving stellar mass distribution for each galaxy. We allow the V-band optical attenuation due to dust to vary between 0 and 6 mag, with a uniform prior, assuming the D. Calzetti et al. (2000) law also used in our "fiducial" Bagpipes run.

We model IGM attenuation following P. Madau (1995). Following S. Tacchella et al. (2022) and due to possible line-of-sight variations in the optical IGM attenuation, we allow the IGM opacity to vary with a clipped Gaussian prior distribution centered on 1, clipped at 0 and 2, and with a dispersion of 0.3. The stellar metallicity is allowed to vary between $-4 \leqslant \log_{10} Z/Z_\odot \leqslant 0.16$ with a uniform prior. We do not link the gas-phase metallicity, which is also free to vary with the same range and prior. Gas-phase metallicity is expected to differ from stellar metallicity at some stages of galaxy evolution (e.g., following significant gas accretion into a galaxy, thus lowering gas-phase metallicity), and decoupling them permits more flexibility in the stellar and nebular emission-line modeling.

We use a P. Kroupa (2001) IMF for consistency with our Bagpipes SED fitting, but as Prospector allows tabulated IMFs, we also test the impact of a top-heavy IMF on the derived stellar masses. Top-heavy IMFs are predicted at high-z, and there is preliminary evidence for a top-heavy IMF in extreme nebular dominated galaxies at high-z (A. J. Cameron et al. 2024). The results for different choices of IMF are detailed in Section 4.4.

We run Prospector using nested sampling with dynesty (J. S. Speagle 2020), using the default sampling settings—with the exception of switching from uniform sampling to the more robust random walk, to efficiently probe the multidimensional parameter space. Since Prospector is computationally expensive to run, we fit only a subset of our galaxy sample, prioritizing those galaxies that are high-redshift or massive. Specifically, we fit all galaxies with z_{phot} (from EAZY-py) above $z \geqslant 8.5$, or with a fiducial Bagpipes stellar mass of $\log_{10}(M_\star/M_\odot) \geqslant 9.0$.

4.3. Stellar Mass Comparisons

In this section, we compare the consistency of the derived stellar masses between our fiducial and alternative Bagpipes models. Figure 1 shows a comparison of the derived galaxy properties of our fiducial Bagpipes run for all sources in our sample to our other Bagpipes results. The details of the models compared are shown in Table 2. As discussed in Section 4.1, we compare models with different priors, SPS models, and SFH parameterizations. The top plot shows the systematic mass offset found when varying the dust law and priors, while the second row shows the same offset for parametric and nonparametric SFHs, as well as a BPASS SPS model (E. R. Stanway & J. J. Eldridge 2018). For each Bagpipes model, we show the Locally Weighted Scatterplot Smoothing fit (LOWESS; W. S. Cleveland 1979). The LOWESS estimator is a nonparametric fitter for noisy data, and shows the overall trend between the mass discrepancy and fiducial stellar mass.

In Figures 2 and 3, we show examples of the photometry, best-fitting Bagpipes and Prospector SEDs, and posterior redshift and stellar mass estimates for a selection of high-mass and/or discrepant galaxies in our sample. We allow the redshift to vary within the EAZY-py posterior PDF for each Bagpipes fit, resulting in only small changes in redshift between individual Bagpipes results. We find that 99.6% of photo-z estimates fall within 15% of our fiducial Bagpipes redshift. The variation in stellar mass and other parameters between models will also depend on the available photometry, and in future surveys with more NIRCam medium bands or deep MIRI data, different systematics may be observed. For this reason, we place the detailed comparison of each model to the fiducial model, along with further discussion of other
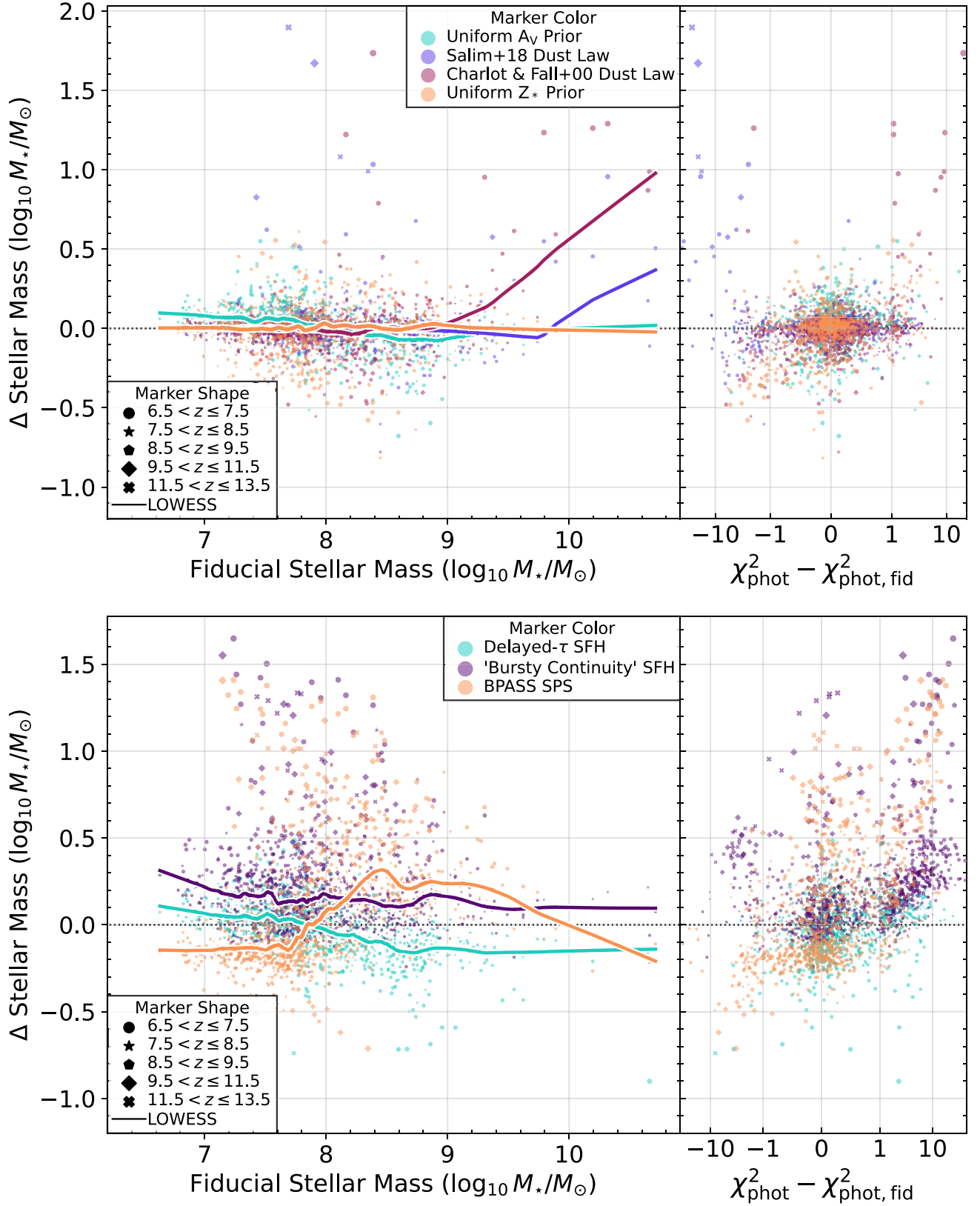
Figure 1. (Top) Comparison of the observed stellar mass offset between our fiducial `Bagpipes` model and alternative models for the entire EPOCHS v1 sample, as a function of fiducial stellar mass. The alternative models considered vary priors on the metallicity and dust attenuation, as well as the assumed dust law. Marker shapes show the redshift bin for each galaxy, based on the fiducial redshift, and each `Bagpipes` model considered is shown in a different color. The colored lines show the LOWESS fit (W. S. Cleveland 1979). The right-hand plots show the stellar mass offset as a function of $\Delta\chi^2$, between the two fits. (Bottom) Same as the upper plot, but the alternative models vary the assumed star formation history or stellar population synthesis model instead.
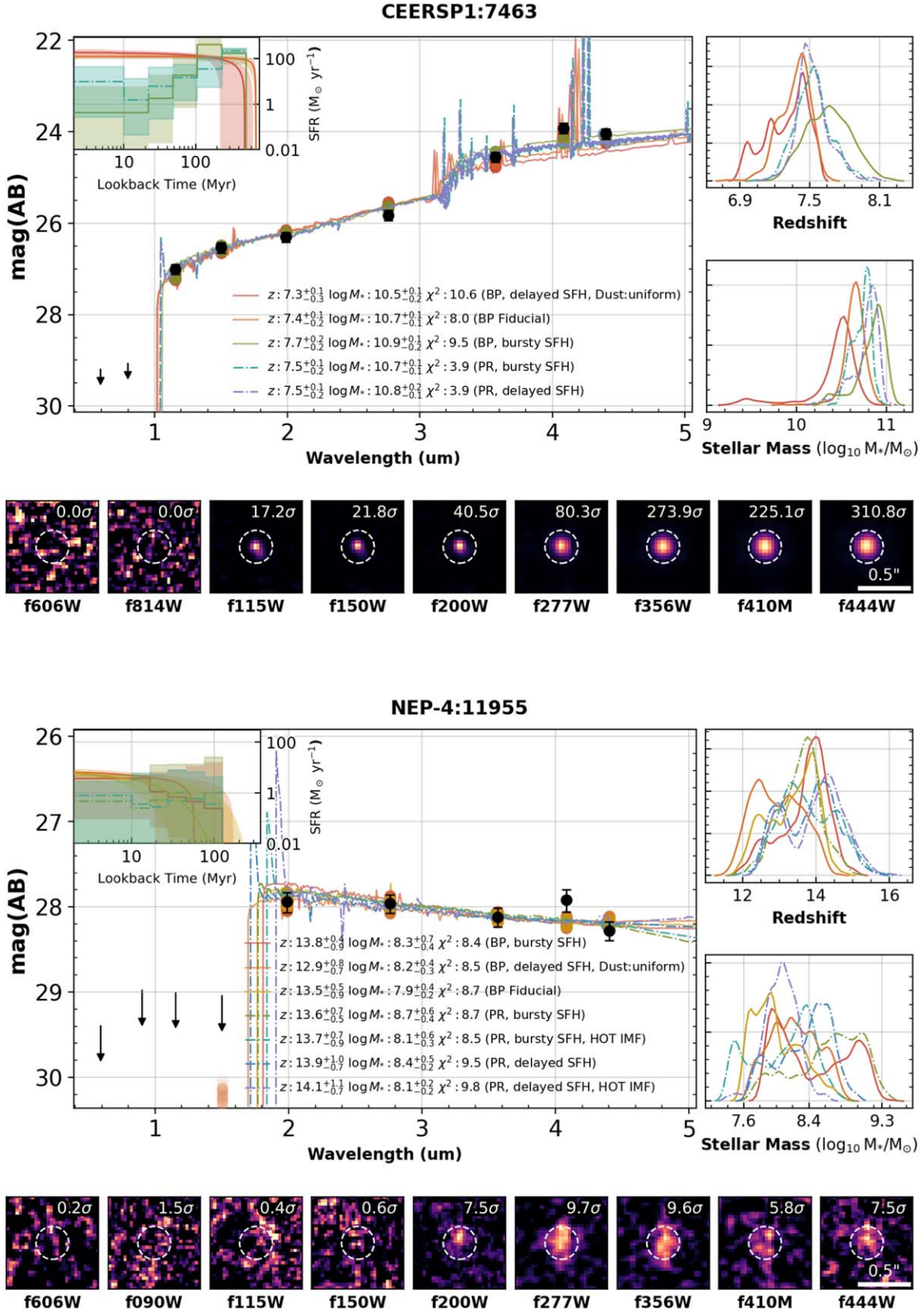
Figure 2. `Bagpipes` (labeled BP) and `Prospector` SEDs (labeled PR) for two of the galaxies in the EPOCHS v1 sample. The top row shows the galaxy labeled *7463_CEERSP1* with one of the largest fiducial stellar masses in the sample, which is a "little red dot" also identified by I. Labbé et al. (2023) and V. Kokorev et al. (2024). The bottom row shows *11955_NEP-4*, one of the more massive galaxies found at $z \geqslant 10$, although the range of stellar mass estimates shows how difficult it is to constrain stellar mass at these redshifts. We label the different SED fits by how they differ from our fiducial `Bagpipes` SED-fitting prescription, with a log-normal SFH, a D. Calzetti et al. (2000) dust model, logarithmic priors on age, dust, and metallicity, a G. Bruzual & S. Charlot (2003) SPS model, and a P. Kroupa (2001) IMF. For each alternative model, we also give the redshift, stellar mass, and χ^2 for the fit. On the right of each SED plot, we show the posterior redshift and stellar mass PDF distributions, and the best-fit SFH history is shown as an inset in the upper left.
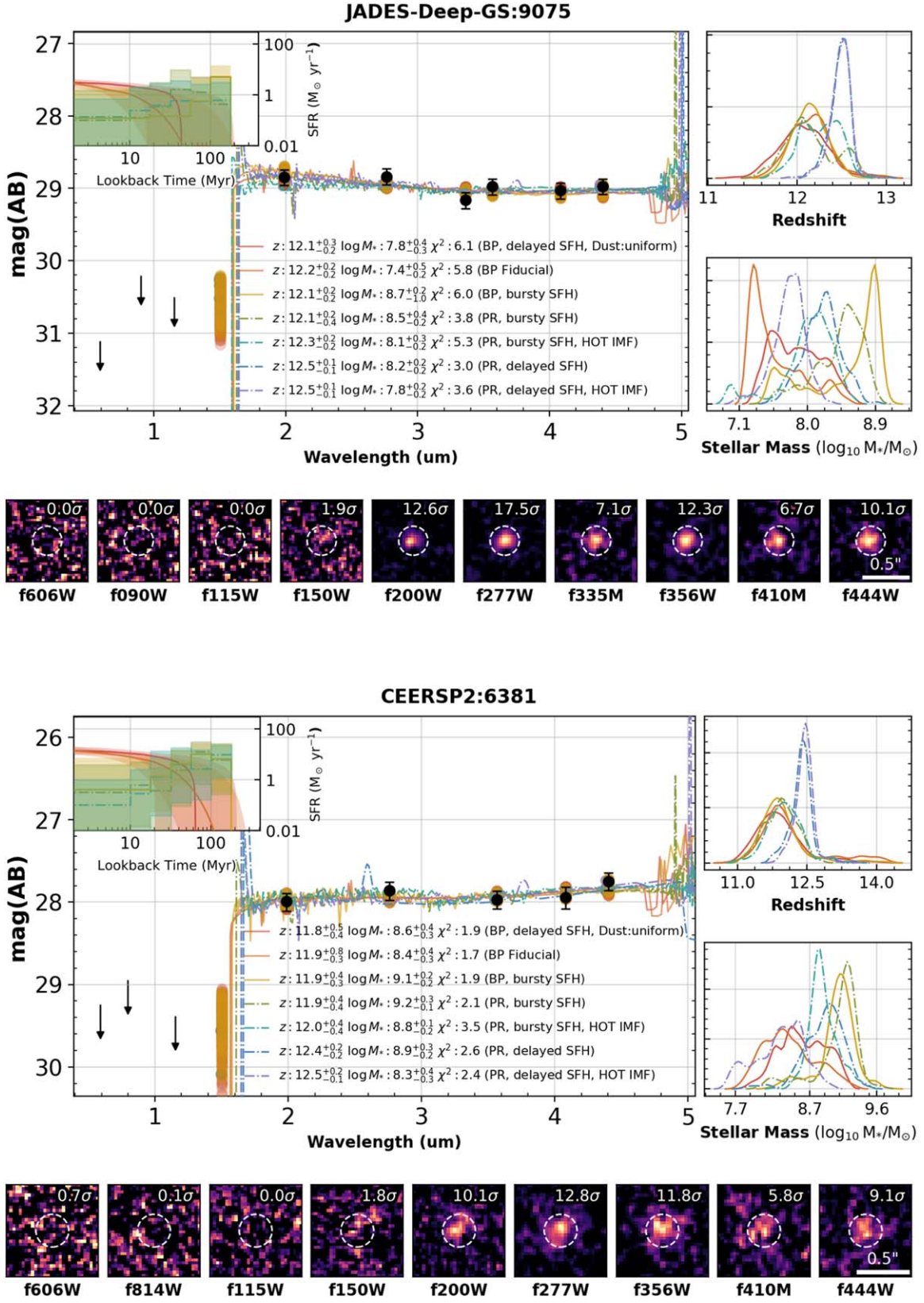
Figure 3. The same as Figure 2, except these galaxies are shown to demonstrate the stellar mass discrepancies observed between different `Bagpipes` and `Prospector` SED fits, depending on the chosen star formation history, SED-fitting tool, dust law, and IMF. *JADES-Deep-GS:9075* was observed with NIRSpec as part of the work of A. J. Bunker et al. (2024; NIRSpec ID `00002773`), who found $z_{spec} = 12.63$, meaning that `Bagpipes` and `Prospector` slightly underestimate the redshift in most cases.

galaxy properties, in Appendix A; in this section, we summarize the impact each model has on the resultant stellar masses. A comparison between the stellar masses derived with `Bagpipes` and `Prospector` can also be found in the appendix.

Focusing first on the the upper panel of Figure 1, the dust extinction and metallicity priors appear to have little systematic effect on the stellar masses, although there is significant scatter seen in a few individual galaxies. Replacing the D. Calzetti et al. (2000) dust law with S. Charlot & S. M. Fall (2000) or S. Salim et al. (2018), we see a significant increase in stellar mass for the most massive galaxies, with the more flexible dust law typically favoring a steeper attenuation power law than used in D. Calzetti et al. (2000). For these massive galaxies, when comparing to the default D. Calzetti et al. (2000) assumption, using the S. Salim et al. (2018) dust law typically results in a better-fitting SED with a lower χ^2, whereas the opposite is true for that of S. Charlot & S. M. Fall (2000).

When we test alternative SFH models, we see a larger stellar mass discrepancy when comparing to the nonparametric flexible SFH than when we compare to an alternative parametric SFH model (delayed exponential). In particular, with the "continuity bursty" SFH, we see offsets of >1 dex with the same goodness of fit, as well as systematically larger stellar masses across the galaxy sample. A good example of this is seen in *JADES-Deep-GS:9075*, as shown in Figure 3, where the observed flat photometry is consistent with a large range of possible SFHs, the inferred masses of which can vary by >1.3 dex with little variation in the χ^2. Exchanging the default BC03 SPS model for the BPASS model appears to have a complex effect on the derived stellar masses, with the magnitude and direction of the observed scatter dependent on the fiducial stellar mass.

4.4. Top-heavy IMF

As discussed in Section 1, one possibility to explain the high inferred stellar masses of high-z galaxies is a "top-heavy" IMF, which results in the production of more high-mass stars, compared to a local IMF, and lowers the inferred mass-to-light ratios in high-z galaxies. We use `Prospector` to investigate the impact of varying the IMF on the inferred stellar mass of a subset of the EPOCHS v1 sample. We implement the modified (P. Kroupa 2001) IMF suggested by C. L. Steinhardt et al. (2023), which assumes a gas temperature evolution $T_{gas} \propto (1+z)^2$. We produce two modified IMFs, one with $T_{gas} = 45$ K, which we use for $8 \leqslant z \leqslant 12$, and one with $T_{gas} = 60$ K, which we use at $z \geqslant 12$. A standard P. Kroupa (2001) IMF would have $T_{gas} = 20$ K in this parameterization, and given the broken-power-law shape, this modification results in an increasingly top-heavy IMF with increasing gas temperature. While it is theoretically possible to produce a unique IMF for each galaxy by assuming a z–T_{gas} relationship, we avoid doing this, for simplicity. We otherwise leave unchanged the `Prospector` configuration, in order to directly compare the impact of the IMF.

In Figure 4, we show the results of modifying the IMF on the stellar mass estimates. We compare the masses derived with a standard (P. Kroupa 2001) IMF to the two modified IMF models, finding significant decreases in stellar mass with very little change in the quality of the fits. We note that, due to the computational intensity of `Prospector` fitting, we only fit a subset of our full sample, and calculate the median decrease in mass for both SFH models and HOT IMFs. For the $z > 12$

sample where we use the HOT 60K IMF, we include our full parent sample; however, for the $z < 12$ model, we fit only galaxies with either $z \geqslant 8.5$ or fiducial `Bagpipes` stellar mass $\log_{10} M_{\star,\text{fid}} > 9.5$. In terms of numbers, there are 221 galaxies in the HOT 45K IMF group, and 21 galaxies in the HOT IMF 60K group. Given that this IMF model is predicted to be applicable in the region of $8 \leqslant z \leqslant 12$ (C. L. Steinhardt et al. 2023), and also given the lack of mass dependence in our results, we do not expect the excluded lower-mass galaxies at $8 \leqslant z \leqslant 8.5$ to significantly impact our findings.

For the nonparametric "delayed" SFH model, we find a median decrease in stellar mass of 0.33 dex for the $z \leqslant 12$ (HOT 45K IMF) galaxy sample. For the $z \geqslant 12$ sample, we find a median decrease of 0.46 dex. For the "continuity bursty" SFH model, we find a median stellar mass decrease of 0.26 dex for the $z \leqslant 12$ sample (HOT 45K IMF) and a decrease of 0.36 dex for the $z \geqslant 12$ sample (HOT 60K IMF). As expected, we see a larger decrease in stellar mass for the HOT 60K model, which is more "top-heavy" than the HOT 45K model.

For the galaxies with the largest fiducial `Bagpipes` stellar masses, which have the most tension with ΛCDM, we discuss the possible decrease in stellar mass using a top-heavy HOT IMF in Section 6.3.

5. Galaxy Stellar Mass Functions

The `Bagpipes` and `Prospector` fitting we perform in Section 4.3 explores the consistency of stellar mass estimates on an individual galaxy basis. In order to explore the overall effect of a particular choice of SED-fitting tool and model, we look at the overall distribution of galaxy masses via the GSMF. We focus primarily on constructing a GSMF from our fiducial `Bagpipes` results, and then demonstrate the effect of changing this to an alternative `Bagpipes` or `Prospector` model.

We make a further cut to our galaxy sample here, removing the fields of El Gordo, SMACS-0723, and Clio. The depths and available filters of these data sets mean that they do not contribute significant volume to our GSMF estimates, but they do increase the redshift uncertainties (N. J. Adams et al. 2024). This reduces the number of galaxies used in the GSMF to 1092 and the total area used to 175 square arcminutes.

The GSMF measures the abundance of galaxies of different masses at a given redshift. A stellar mass function $\Phi(M, z)\Delta M$ is formally defined as the number density of galaxies in a mass bin δM at a given redshift z. The evolution of the shape and normalization of the stellar mass function traces the global abundance of baryons across cosmic time, and hence indirectly traces star formation. The integral of the stellar mass function over mass gives the galaxy SMD, which is the cumulative formed stellar mass per unit volume at a given epoch.

We construct a GSMF from different mass estimates in order to investigate possible evolutions of the GSMF at high redshift. To derive the GSMF, we use the $1/V_{\text{max}}$ methodology (M. Rowan-Robinson & W. H. McCrea 1968; M. Schmidt 1968):

$$\phi(M)\,d\log(M) = \frac{1}{\delta M}\sum_i \frac{1}{C_i V_{\text{max},i}}, \qquad (1)$$

with associated uncertainty

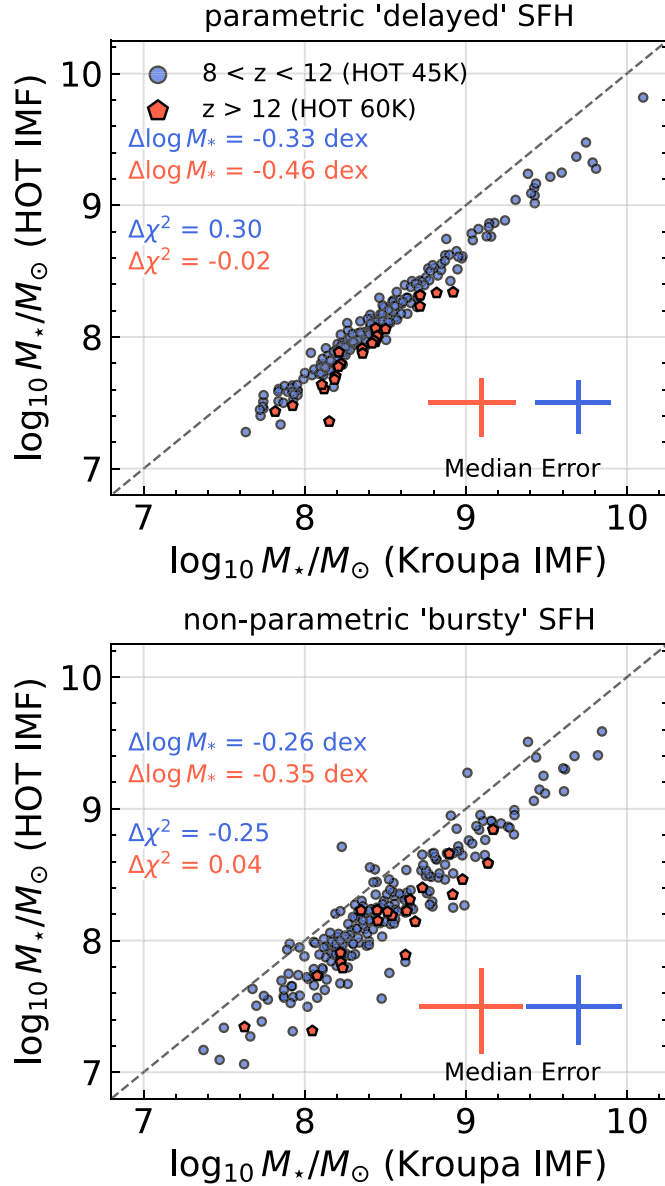$$d\phi(M) = \frac{1}{\delta M}\sqrt{\left(\sum_i \frac{1}{C_i V_{\text{max},i}}\right)^2}, \qquad (2)$$

parametric 'delayed' SFH

non-parametric 'bursty' SFH

Figure 4. (Top) Effect of modified top-heavy IMF on galaxy masses using a parametric delayed-τ SFH, for both the HOT 45K IMF (at $8 < z < 12$) and HOT 60K IMF (at $z > 12$) from C. L. Steinhardt et al. (2023). Overlaid on the plot are the median stellar mass and χ^2 offsets, showing that these IMF models systematically reduce the stellar mass with no impact on the goodness of fit. (Bottom) Effect of modified IMF on galaxy masses using a nonparametric "continuity bursty" SFH for both HOT models.

where δM is the bin width in stellar mass, C_i is the completeness of the galaxy in bin i, and $V_{\mathrm{max},i}$ is the total observable volume of the galaxy across all the fields. We use Equation (2) to calculate the uncertainty in the bin, except in the case where there are the bin has very low occupancy ($N \leqslant 4$), where we instead directly calculate the Poisson confidence interval with a more accurate estimator based on the χ^2 distribution: $I = [0.5\chi^2_{2N,a/2}, 0.5\chi^2_{2(N+1),1-a/2}]$ (K. Ulm 1990; N. J. Adams et al. 2024), which avoids uncertainties such as 1 ± 1, which appear infinite on a log-scale.

Other distribution function estimators have been used that are more statistically robust than $1/V_{\mathrm{max}}$, but $1/V_{\mathrm{max}}$ is very commonly used in estimates of the UV LF and GSMF (e.g., R. Bhatawdekar et al. 2019; M. Stefanon et al. 2021; J. Weaver

et al. 2023; N. J. Adams et al. 2024; D. J. McLeod et al. 2024; R. Navarro-Carrera et al. 2024; A. Weibel et al. 2024), so we choose to use it in order to compare our results directly with the literature. In N. J. Adams et al. (2024), we compare $1/V_{\mathrm{max}}$, to the Lynden-Bell C-method, which is more statistically robust, when estimating the UV LF and find results consistent within 0.5 dex (D. Lynden-Bell 1971; M. Woodroofe 1985).

We iteratively shift the galaxy SED from the fiducial Bagpipes SED fitting in small steps of $\Delta z = 0.01$ before recalculating the bandpass-averaged fluxes in the available NIRCam and HST filters for a given field. With these fluxes, we test if the galaxy would still be selected at every redshift step, given our selection criteria detailed in Section 3.2. For the selection criteria that are dependent on SNR requirements, we base the detection strength on the average depth for each field, as given in Table 1. This allows us to calculate a z_{max} and z_{min} redshift for each galaxy in each field, capped at the edges of each redshift bin. Accounting for a minimum redshift is essential for accurately measuring the detectable volume, given our requirement for the shortest-wavelength filter bandpass to fall blueward of the Lyman break. We convert these maximum and minimum redshifts within each bin to a volume by

$$V_{\mathrm{max},i} = \sum_{\mathrm{fields}} \frac{4\pi}{3} \frac{A_s}{4\pi \; \mathrm{sr}} (d_{z_{\mathrm{max}}}^3 - d_{z_{\mathrm{min}}}^3), \qquad (3)$$

where $d_{z_{\mathrm{max/min}}}$ are the comoving distances at the maximum/ minimum detectable redshifts (capped at bin edges). A_s represents the survey areas, which are given in Table 1.

The only field containing a significant lensing cluster that we include in the GSMF is the MACS-0416 field. We exclude the cluster itself, and assume there is no significant magnification for our galaxy candidates in the surrounding NIRCam pointings. None of our candidates show evidence of strong lensing, and we do not expect weak lensing by foreground neighbors to significantly affect our sample.

We account for the posterior stellar mass uncertainties using a Monte Carlo bootstrap methodology to bootstrap our GSMF. We draw stellar mass estimates for each galaxy from the posterior stellar mass probability distribution functions and compute 1000 independent realizations of the GSMF from these posterior PDFs. We compute the 16th, 50th, and 84th percentiles of the distribution in order to quantify the uncertainty introduced by our stellar mass estimates, and indirectly by the uncertainties on the photometry. Typically, these uncertainties are smaller than the Poisson error, but they can be large at the highest mass, where individual objects near bin edges can have a large impact. We require a bin to be occupied in more than 20% of realizations in order to avoid highly uncertain bins that have very low occupancy.

5.1. Detection Completeness

We carry out completeness simulations on JWST data by inserting simulated galaxies with an exponential light profile (Sérsic index of $n = 1$), as galaxies at high-z are typically not concentrated (see L. Ferreira et al. 2022, 2023; K. Ormerod et al. 2024), and with absolute UV magnitudes ranging from -16 to -24 in the detection image (inverse-variance-weighted stack of F277W, F356W, and F444W). We then run SExtractor on them using the same configuration as our normal catalog creation pipeline in order to measure the fraction recovered as a function of apparent magnitude.

The magnitude range was swept in steps of 0.2, with 1000 sources inserted into the image at a time in order to prevent introducing artificial overdensities. We assume a size–luminosity relation of $r \propto L^{0.5}$ (A. Grazian et al. 2012), with the reference size set to $r = 800$ pc at $M_{UV} = -21$, with M_{UV}-dependent intrinsic scatter modeled with a log-normal distribution calibrated from the results of L. Yang et al. (2022). The inclination angle of these sources was assumed to be uniformly random. We sweep a redshift range of 6.5–13.5 in steps of 0.5 to account for the changes in angular diameter distance and obtain a 2D dependence of completeness on redshift and absolute magnitude.

The above procedure was carried out on all fields considered in this paper. Given that we perform our detection on a stacked image of the LW bandpasses, our detection completeness is >90% across the redshift ranges and apparent magnitudes of our high-z sample, and the overall completeness is dominated by the impact of our selection criteria.

5.2. Selection Completeness and Contamination

To estimate the contamination and completeness of our sample selection as a function of stellar mass, we use version 1.2 of the JADES Extragalactic Ultra-deep Artificial Realization (JAGUAR) catalog of synthetic galaxies released by the JADES Collaboration (C. C. Williams et al. 2018). We choose this model for our completeness simulations because the catalogs and spectra are readily available, and S. M. Wilkins et al. (2023a) have shown that the JAGUAR model reproduces the observed color evolution of galaxies at high redshift.

JAGUAR is an empirical model based on observational constraints on the mass and luminosity functions at $z \leqslant 10$ from HST (A. R. Tomczak et al. 2014; R. J. Bouwens et al. 2015; M. Stefanon et al. 2017). Mock spectra and photometry are generated using BEAGLE (J. Chevallard & S. Charlot 2016). We combine five different realizations of the simulation in order to improve the statistics for rare high-z and high-mass sources. We filter the mock catalogs to the sources that are detectable given the average depths of our observations. This ranges between 8×10^5 and 1.2×10^6 realistic mock galaxies, which we run through our full galaxy selection procedure.

We generate mock observations from these catalogs by estimating 1σ errors in the measurements based on the average depths of our JWST reductions in each field (see Table 1). We then perturb the catalog photometry in flux space within a Gaussian centered on the catalog measurement and width equal to the 1σ error in that filter. These perturbed fluxes are then run through our full selection procedure to measure how well our pipeline recovers the true redshifts of the sources. This allows us to compare the robustness of our selection criteria given the differing depths and filters in each set of observations.

We test our ability to reconstruct the stellar masses of the JAGUAR galaxies by fitting their perturbed photometry with our Bayesian SED-fitting using Bagpipes. We estimate completeness and contamination for each redshift and mass bin in our mass function by testing the recovery of simulated galaxies into the correct bin. Completeness is defined as the number of galaxies that our pipeline places in the correct redshift and mass bin, divided by the total number of simulated galaxies within that bin. Contamination is defined as the number of galaxies we place in the incorrect bin, divided by the total number of galaxies in the bin. As an example, if there are 100 simulated galaxies in a given redshift/mass bin, and our

selection criteria selects 50, of which 10 are actually from a different bin, then the completeness would be 50% (50/100) and the contamination would be 20% (10/50).

We see reasonable agreement between the true stellar mass and our inferred stellar mass. Initially, 50% of galaxies fall within the correct stellar mass bin used in construction of the GSMF. In order to account for the different choice of IMF and SFH parameterization between the JAGUAR SEDs and our Bagpipes fitting, we derive a corrective scaling factor by which we scale the JAGUAR masses in order to increase the agreement between the mass estimates to 65%. As we bootstrap the GSMF using the stellar mass PDFs, we find that 80% of galaxies will contribute to the correct mass bin. The average offset between our recovered stellar mass and the simulated mass is 0.02 dex, with a standard deviation of 0.28 dex. Only 2% of the time is the deviation between the scattered and recovered masses greater than 0.75 dex, which is the bin width used in the stellar mass functions.

Figure 5 shows the completeness and contamination for the CEERS and JADES fields, which make up a significant fraction of our total volume.

To derive a single estimate of completeness and contamination for each galaxy, we calculate the area-averaged completeness and contamination for each galaxy in our sample, based on the fields in which the galaxy is found to be observable in when we calculate V_{max}. The bottom row of Figure 5 shows the total completeness, including both detection and selection, for each galaxy as as function of stellar mass. Completeness is strongly dependent on the stellar mass of the galaxy, and at masses below $\approx 10^8 M_\odot$ we are $\leqslant 50\%$ complete in the majority of our area and dependent on the derived completeness corrections.

In order to reduce the possible effects of contamination on our derived mass functions, we exclude objects where the estimated contamination fraction is $\geqslant 50\%$. In the cases where no simulated galaxies fall within a given bin, which occurs only for the highest-mass bins where we expect high completeness, we do not apply any correction factor. We also assume 100% completeness when the total number of simulated galaxies in a mass–redshift bin is $\leqslant 5$, due to the high uncertainty in deriving correction factors with low statistics.

Multiple classes of interlopers with photometry similar to high-redshift galaxies can contaminate estimates of the GSMF. In this section, we detail our methodology to remove common types of interlopers, including low-z galaxies, brown dwarfs, and AGN.

5.2.1. Low-z Galaxies

The misclassification of low-z galaxies as high-z through catastrophic errors in photo-z are commonly caused by misidentification of different spectral features, e.g., confusion of the Lyman and Balmer breaks, or strong rest-frame optical emission lines contributing to multiple wideband photometric observations, giving the appearance of continuum emission (e.g., the $z = 16$ candidate in C. T. Donnan et al. (2023) and P. Arrabal Haro et al. (2023a), which we do not select as a robust high-z galaxy with our EAZY-py SED fitting and selection criteria).

First, we compare our EAZY-py photo-z estimates with spectroscopic redshifts (spec-z) in N. J. Adams et al. (2024). In summary, we typically find >90% accuracy (within 15%). With our EAZY-py photo-z, which we use as an informative prior for Bagpipes and Prospector, we do not observe the systematic photo-z overestimation observed in other studies (P. Arrabal Haro et al. 2023b; S. Fujimoto et al. 2023b).
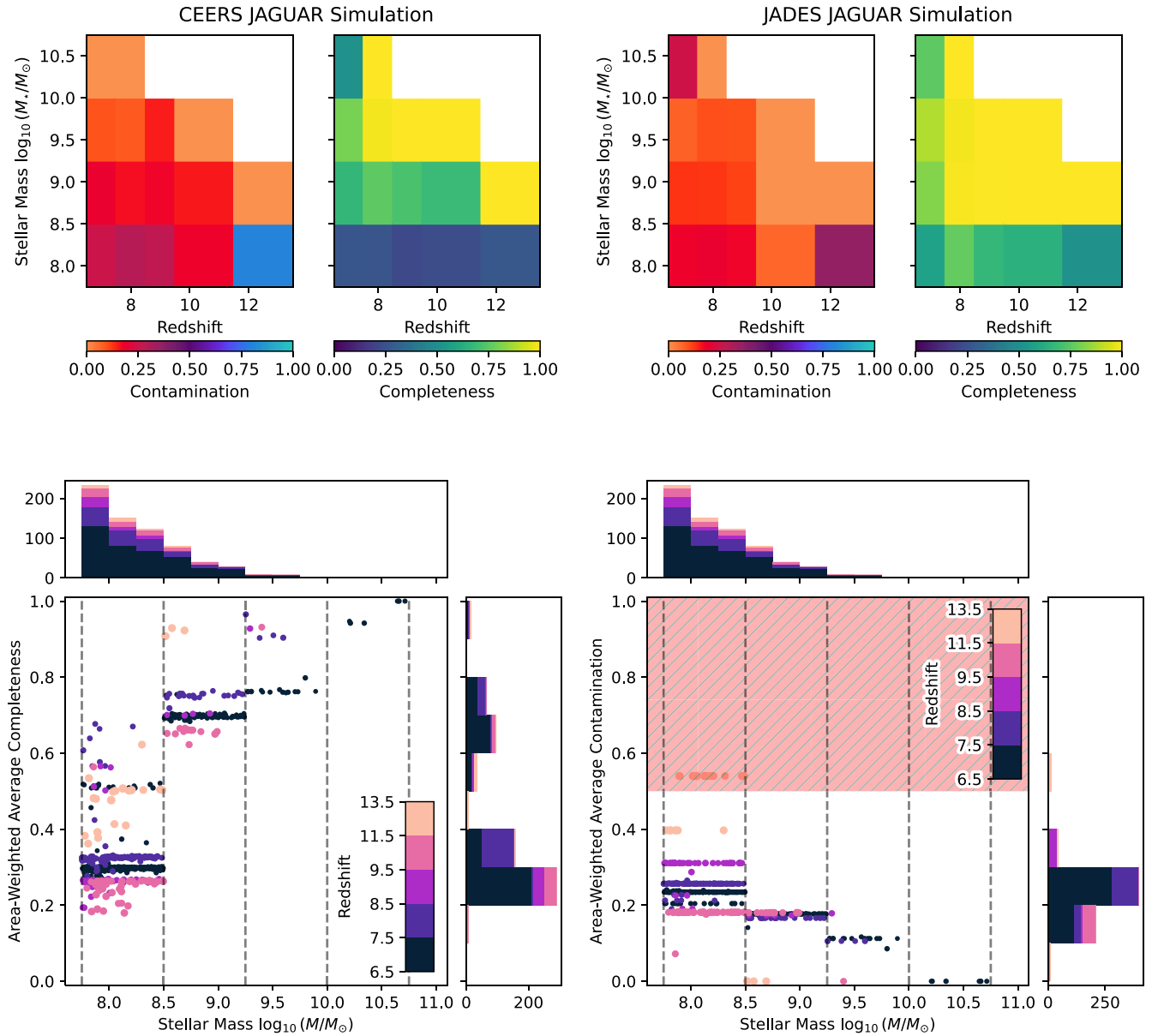
Figure 5. (Top) Selection completeness as a function of redshift and stellar mass for two example fields from our sample, based on our fiducial `Bagpipes` SED fitting and full selection procedure. Completeness and contamination are labeled as fractions, where $1 = 100\%$. (Bottom) Total area-weighted completeness and contamination for each of our galaxies as a function of stellar mass, colored by redshift bin. We see higher completeness and lower contamination at higher mass. The red shaded region in the contamination plot shows our 50% contamination limit.

We are able to fully test the rate of catastrophic photo-z failure using our `JAGUAR` completeness and contamination simulations. The rate of contamination increases as we approach our 5σ detection limits in the rest-frame UV, and the vast majority of the contaminants have $<8\sigma$ detections in the rest-frame UV. If we parameterize in terms of stellar mass, the highest rates of contamination are seen at lower stellar mass, where individual galaxies have less impact on the GSMF. Candidates with SNR close to our selection limit are also those most commonly rejected in our manual inspection of all candidates, providing another layer of protection against possible interlopers.

We restrict the redshift range and fields used when constructing the GSMF to exclude uncertain high-z candidates. We do not include observations of El Gordo, Clio, or SMACS-0723 when constructing the GSMF, because they are shallow and show high rates of contamination in our `JAGUAR`

simulations. Clio and SMACS-0723 also lack observations in F115W, which J. A. Trussler et al. (2023) show lead to inaccurate photometric redshifts at $8 < z < 10$. Despite our sample containing galaxies at $z \geqslant 14$, we do not attempt to measure the GSMF above $z \geqslant 13.5$, because we lack the appropriate medium-band observations (or spectroscopy) to remove interlopers such as the $z = 16$ candidate in C. T. Donnan et al. (2023). Below redshift 13.5, we have seen high accuracy in photo-z estimates when compared to NIRSpec spectroscopy (e.g., P. Arrabal Haro et al. 2023a; E. Curtis-Lake et al. 2023; B. Wang et al. 2023; A. J. Bunker et al. 2024).

5.2.2. Brown Dwarfs

Y- and T-type brown dwarfs within the Milky Way can masquerade as high-redshift galaxies, due to the appearance of a Lyman-break-like dropout caused by strong molecular
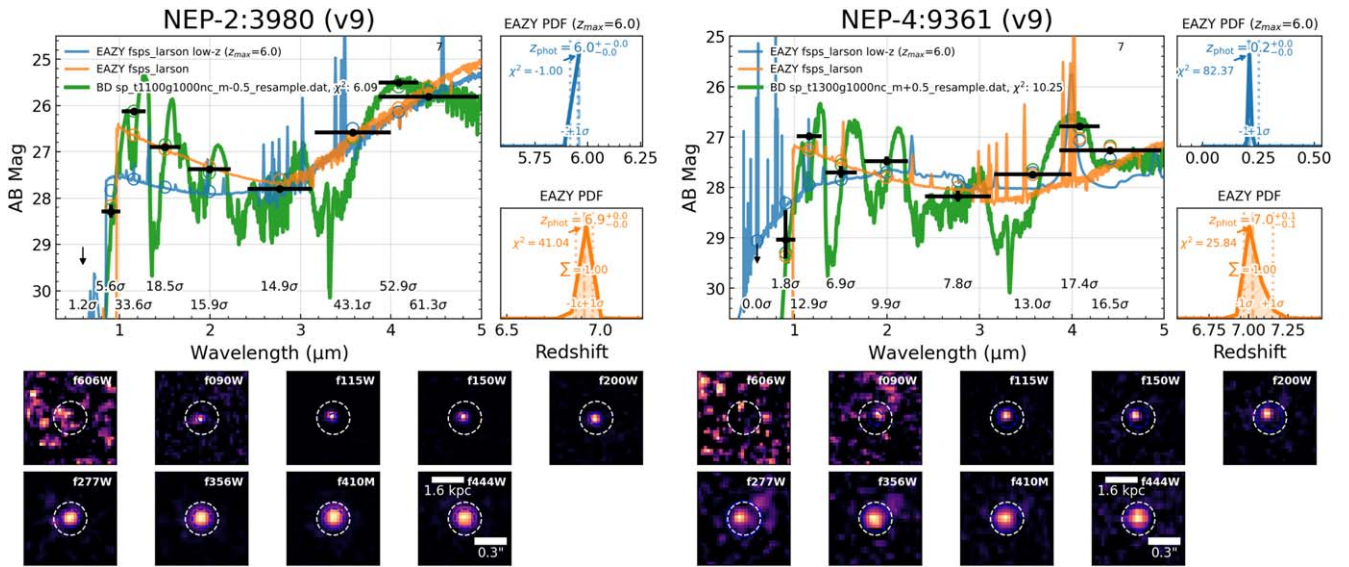
Figure 6. Two example SEDs from our sample of 59 brown dwarf candidates (in green) selected with the Sonora Bobcat models, shown along with their best-fitting high-z galaxy SEDs (in orange). The low-redshift galaxy solution (with an upper redshift limit of $z \leqslant 6$), which is used in our robust galaxy selection criteria, is shown in blue. The redshift posteriors from EAZY-py are shown for both the high- and low-redshift galaxy models, and are overlaid with the statistics used within our selection criteria, indicating the χ^2 and integral of the primary PDF peak. The cutouts of both brown dwarf candidates are shown below the best-fitting SEDs, demonstrating their compact PSF-like morphology. The cutouts are $0\farcs9$ across, as shown with the scalebar, and the white circle shows the extraction aperture used for SED-fitting ($0\farcs16$ radius). The scalebar showing physical size in kpc is calculated at the best-fitting galaxy photo-z and is not applicable to the brown dwarf solution. The coordinates for these brown dwarf candidates are $17^{\rm h}23^{\rm m}12\fs36 +65\arcdeg49\arcmin38\farcs8$ and $17^{\rm h}21^{\rm m}53\fs00 +65\arcdeg49\arcmin20\farcs82$, respectively.

absorption in the optical, coupled with bright near-infrared emission. When mistaken for high-z galaxies, brown dwarfs can have a large impact on the GSMF, due to their high inferred stellar masses.

We fit the photometry of all of our galaxy candidates with the synthetic Sonora Bobcat brown dwarf templates (M. Marley et al. 2021), using a simple χ^2 minimization to scale the flux of the templates to each candidate. We fit all the provided templates to each candidate, selecting the best-fitting template for each galaxy. We remove candidates from our sample that are both better fit by a brown dwarf template than a galaxy template and show a PSF-like morphology (50% encircled flux radius in F444W < F444W PSF FWHM). This removes 59 candidates in total (4% of the total sample). Figure 6 shows an example of several brown dwarf candidates that would otherwise have been selected as high-z galaxy candidates.

None of the brown dwarf candidates selected in K. N. Hainline et al. (2024b) are contained within our robust galaxy sample in the Goods-South or CEERS fields. As a check of our selection criteria, we confirm that all of the K. N. Hainline et al. (2024b) candidates located within the footprint of our data sets (GOODS-South and CEERS) are selected as brown dwarfs by our brown dwarf selection criteria.

5.2.3. Active Galactic Nuclei

Given the apparent prevalence of high-z AGN detected by multiwavelength and spectroscopic studies, it is likely there is a population of galaxies containing AGN within this sample. Our modeling does not fit AGN components to the photometry, so if galaxies contain a significant AGN component, it is likely we will overestimate the stellar mass. In particular, obscured AGN with red colors (e.g., D. D. Kocevski et al. 2023; I. Labbé et al. 2023) can mimic strong Balmer breaks, leading to inference of an aged stellar population and high stellar mass. Known as

LRDs, a number of studies have found numerous candidates up to $z \leqslant 9$ (see, e.g., I. Labbe et al. 2023; G. Barro et al. 2024; L. J. Furtak et al. 2024, 2023c; J. E. Greene et al. 2024; V. Kokorev et al. 2024; J. Matthee et al. 2024). Different selection techniques have been proposed for LRDs, and it is not clear that all the objects grouped as LRDs with a given criteria indeed have the same origin. The term originated to categorize spectroscopically identified obscured broad-line AGN at high redshift, but has become more generally used to describe photometrically selected compact red galaxies, which may or may not be dominated by AGN emission. Photometric selections typically rely on a rest-optical color cut (F277W − F444W for $z \approx 6$–7) as well as a compactness criteria, with spectroscopic analysis from J. E. Greene et al. (2024) suggesting that a F277W − F444W break exceeding 1.6 mag identifies LRDs with an 80% AGN purity, without requiring an additional compactness criteria. The criteria of I. Labbé et al. (2023) and V. Kokorev et al. (2024) require a weaker color selection, which may be selecting a mix of AGN and dusty star-forming systems. C. C. Williams et al. (2024) have used MIRI observations from 5 to 25 μm of a sample of likely AGN-dominated LRDs with strong breaks, finding a flattening of the red colors (in F_ν) at longer wavelengths, which they suggest as evidence for obscured AGN that lack toroidal hot dust. In contrast, P. G. Pérez-González et al. (2024) use MIRI observations of a wider population of LRDs, which may not be a single class of object, to suggest that the characteristic photometry is driven mostly by stellar emission, and that LRDs are mostly compact and highly obscured starburst galaxies with young stellar ages. Other studies have struggled to distinguish between AGN and stellar models (G. Barro et al. 2024) or favor an AGN model (A. Noboriguchi et al. 2023). Stacking deep X-Ray observations of LRDs have also revealed a surprising lack of X-Ray emission (M. Yue et al. 2024; T. T. Ananna et al. 2024; R. Maiolino et al. 2024), which is somewhat puzzling to explain under the AGN scenario, although high obscuration or

intrinsic X-ray weakness in the accretion disk have been proposed (R. Maiolino et al. 2024). Further spectroscopic or MIRI observations could break the degeneracy between AGN and old stellar populations.

While it is essentially impossible to distinguish between the contribution of AGN and stellar emission to an SED with only rest-optical photometry, we attempt to perform additional SED fitting using `Prospector` by including an AGN component, which models AGN emission lines for the most massive galaxies in our sample ($M_\star \geqslant 10^{9.5} M_\star$). In almost all cases, the AGN fraction is less than 10%, and we see no reduction in stellar mass due to the inclusion of AGN component. The addition of an AGN model does not statistically improve the fit for these galaxies, although we cannot strongly exclude the presence of AGN in some of our candidates, as the AGN model within `Prospector` models only obscured AGN (J. Leja et al. 2018). Further fitting with a wider range of AGN models, which is outside the scope of this paper, is required to constrain the potential contribution of AGN emission to the observed photometry. Given the uncertainty around the true nature of these sources, we choose not to remove them from our sample. We discuss the impact of LRDs on the GSMF in Appendix B.

We do, however, remove two galaxies from our sample that are spectroscopically confirmed as AGN, or with significant AGN components within the photometry. This includes the AGN within the CEERS field presented in R. L. Larson et al. (2023).

5.3. Cosmic Variance

Cosmic variance is the field-to-field variance of the distribution of galaxies at a given redshift due to galaxy clustering. Empirical measurements of cosmic variance do not exist at $z \geqslant 7$. Estimates of cosmic variance from simulations (e.g., *Bluetides*; A. K. Bhowmick et al. 2020) are available, but the accuracy of these estimates is difficult to measure, given the limited cosmological volume and dependence on the assumed cosmology and galaxy formation physics. A. K. Bhowmick et al. (2020) argue that cosmic variance will be a dominant source of uncertainty at these redshifts, as galaxies are predicted to be highly clustered (A. K. Bhowmick et al. 2018).

We caution that the following methodology provides only an approximation of the true cosmic variance, as the underlying quantities, such as the galaxy bias, are not well-quantified at $z \geqslant 7$ and are generally extrapolated from wider area clustering results at lower redshift or taken from *N*-body simulations (B. P. Moster et al. 2010). We estimate the uncertainty on the GSMF due to cosmic variance following the prescription of S. P. Driver & A. S. G. Robotham (2010), combining the cosmic variance from different surveys using the volume-weighted sum of squares from B. P. Moster et al. (2011). We treat nearby pointings as one observation and sum their areas (e.g., the multiple pointings of CEERS or the NEP, which are not widely separated enough on the sky to be considered independent). We add the uncertainty in quadrature to Equation (2).

We compute a cosmic variance estimate for each galaxy individually, based on which of our fields they are found to be detectable in. Given that this work combines multiple widely separated fields for the majority of our sample, cosmic variance is small compared to studies incorporating only a single field. We see little difference in cosmic variance across our redshift bins. In the best case, where a galaxy is detectable across every field, the average cosmic variance across all redshift bins is found to be 18%. The highest cosmic variance estimates are for faint galaxies that, given our selection criteria, are only detectable in the JADES GOODS-South field, where we find a cosmic variance of 42%.

5.4. Fitting the GSMF

The overall scientific consensus is that the stellar mass function at high-z is well-described by the *Schechter* function (P. Schechter 1976), given in logarithmic form in Equation (4):

$$\Phi(d \log M) = \ln(10) \Phi^\star e^{-10^{\log M - \log M^\star}}$$
$$\times (10^{\log M - \log M^\star})^{\alpha+1} \, d \log M. \tag{4}$$

The Schechter function, which consists of a power law with an exponential falloff, is parameterized by three parameters: α, $M^\star$, and $\Phi^\star$. α controls the slope of the low-mass end of the SMF, while $M^\star$ gives the turnover point at which the function turns from a power-law to an exponential falloff. $\Phi^\star$ controls the overall scaling of the SMF, and is the only parameter that has been confidently shown to evolve with cosmic time (P. Popesso et al. 2023).

Before JWST, the mass function was constrained up to $z \approx 9$ using HST WFC3/IR, Spitzer/IRAC, and ground-based data (Visible and Infrared Survey Telescope for Astronomy (VISTA) and United Kingdom Infrared Telescope (UKIRT)) from observations obtained via the Hubble Ultra Deep Field (HUDF), CANDELS, Cluster Lensing and Supernova survey with Hubble (CLASH), and Hubble Frontier Fields (HFF) surveys (D. P. Stark et al. 2013; M. Bradač et al. 2014; K. Duncan et al. 2014; R. J. Bouwens et al. 2016; M. Song et al. 2016; M. Stefanon et al. 2017; R. Bhatawdekar et al. 2019; S. Kikuchihara et al. 2020). These studies generally agree that the mass function steepens out to $z \approx 10$, with the low-mass slope, α, $\rightarrow -2$. K. Duncan et al. (2014), R. Bhatawdekar et al. (2019), and M. Stefanon et al. (2021) find that the stellar mass to halo mass ratio in galaxies ($M_\star$–M_h) shows no evolution over $6 \leqslant z \leqslant 10$ despite a 3 dex increase in overall stellar mass, suggesting that stellar and halo mass grew together during reionization. Pre-JWST, the accuracy of stellar mass functions at these redshifts is limited by the uncertainty in stellar mass estimates from Spitzer data, where the broadband photometry can be affected by strong nebular emission causing scatter in stellar mass estimates, which is compounded by the limited number of spectroscopically confirmed galaxies at these redshifts (G. W. Roberts-Borsani et al. 2016; V. Strait et al. 2020). Previously, measurements of the mass function above $z \geqslant 6$ have relied on UV-selected samples of galaxies, with mass indirectly inferred through a calibrated L_{UV}–$M_\star$ relationship (Y. Harikane et al. 2016; M. Song et al. 2016) rather than direct measurements of the rest-frame optical wavelengths. Photometric mass-selected samples above $z \geqslant 2$ often have significant unavoidable mass uncertainties at higher redshift (J. Retzlaff et al. 2010; C. Laigle et al. 2016; J. Weaver et al. 2023), due to the lack of available rest optical or NIR photometry. Many studies combine ground- and space-based observations in order to probe the entire mass function, although combining these data sets robustly is difficult due to systematics between different surveys, including differing selection functions, SED-fitting techniques, detection bands, and survey depths.

Table 3
Tabulated GSMF from Our Fiducial Bagpipes SED Fitting

Redshift Bin	$\log_{10}\left(\frac{M_\star}{M_\odot}\right)$	Med($\log_{10} M_\star$)	Φ (10^{-4} dex^{-1} Mpc^{-3})	Comp (%)	Cont (%)	N_{gal}
$6.5 < z \leqslant 7.5$	8.125 ± 0.375	8.07	$49.65^{+10.69}_{-10.29}$	31	23	273
(6.94)	8.875 ± 0.375	8.75	$7.37^{+1.79}_{-1.57}$	70	18	103
	9.625 ± 0.375	9.47	$1.32^{+0.53}_{-0.42}$	79	10	18
	10.375 ± 0.375	10.40	$0.64^{+0.46}_{-0.35}$	60	0	5
	11.125 ± 0.375	10.81	$0.04^{+0.09}_{-0.04}$	100	0	1
$7.5 < z \leqslant 8.5$	8.125 ± 0.375	8.09	$16.06^{+3.68}_{-3.48}$	35	25	109
(8.02)	8.875 ± 0.375	8.73	$1.64^{+0.60}_{-0.45}$	75	17	30
	9.625 ± 0.375	9.45	$0.17^{+0.17}_{-0.08}$	91	11	4
$8.5 < z \leqslant 9.5$	8.125 ± 0.375	8.02	$8.16^{+2.30}_{-2.13}$	28	30	40
(8.86)	8.875 ± 0.375	8.71	$0.50^{+0.35}_{-0.20}$	70	17	8
	9.625 ± 0.375	9.48	$0.05^{+0.10}_{-0.05}$	93	18	1
$9.5 < z \leqslant 11.5$	8.125 ± 0.375	8.10	$4.53^{+1.12}_{-1.00}$	26	18	42
(10.40)	8.875 ± 0.375	8.73	$0.64^{+0.25}_{-0.19}$	65	18	16
	9.625 ± 0.375	9.42	$0.03^{+0.10}_{-0.02}$	93	0	1
$11.5 < z \leqslant 13.5$	8.125 ± 0.375	8.09	$2.13^{+0.99}_{-0.90}$	34	40	5
(11.94)	8.875 ± 0.375	8.70	$0.22^{+0.22}_{-0.12}$	90	0	5

Notes. We give the average number of galaxies in each bin, as well as the estimated average completeness and contamination estimates based on our JAGUAR simulations, along with the median redshift (in brackets) and stellar mass for all the objects in a given bin. See Section 5.2 for the definition of completeness and contamination used in this work. This table is available for download at https://github.com/tHarvey303/EpochsIV.

We derive a mass function for five redshift bins: $6.5 \leqslant z < 7.5$, $7.5 \leqslant z < 8.5$, $8.5 \leqslant z < 9.5$, $9.5 \leqslant z < 11.5$, and $11.5 \leqslant z < 13.5$, which cover a time period of $\sim$500 Myr. We cover a mass range from $7.75 \leqslant \log_{10} M_\star/M_\odot \leqslant 11.5$ in steps of 0.75 $\log_{10} M_\star/M_\odot$. Our lower mass limit is driven by our completeness simulations, and the bin width is chosen to ensure adequate statistics in the majority of bins. Given the quantization of our completeness correction to each stellar mass/redshift bin, we ensure our mass bins are wide enough to ensure our SED fitting places galaxies within the correct mass bin, so that the completeness corrections are calculated correctly because we can recover the masses of the simulated galaxies to within the correct stellar mass bin. We fit the GSMF using Bayesian methods, specifically Markov Chain Monte Carlo via the emcee package (D. Foreman-Mackey et al. 2013).

For our highest redshift bin ($11.5 \leqslant z < 13.5$), we do not attempt to fit the mass function for a number of reasons. First, given the low number of available data point, a meaningful fit is not possible without fixing multiple parameters. Second, the increasing uncertainties in stellar mass estimates reduce the reliability of candidates at these redshifts. Furthermore, the stellar mass estimates are less reliable when there is less rest-frame optical photometry available during SED fitting. Our JAGUAR simulations also suggest that this bin has high contamination at lower mass, with many galaxies below $10^{8.5} M_\odot$ having $\geqslant$50% average contamination across the fields they are detectable in.

We use wide uniform priors on $\Phi^\star$, $M^\star$, and α, with $-8 \leqslant \log \Phi^\star \leqslant -2$, $8.0 \leqslant \log M^\star \leqslant 12.5$ and $-3.5 \leqslant \alpha \leqslant -1.0$ in our MCMC fitting procedure, and run until it has converged before taking 50,000 independent draws from the posterior. We calculate the median posterior, the $\pm 1\sigma$ uncertainty from the 16th/84th percentiles, as well as the maximum likelihood draw.

5.5. Mass Functions at $6.5 < z < 13.5$

Table 3 gives our tabulated GSMF for each redshift bin, as well as the associated 68% (1σ) uncertainties. We also list the median number of galaxies, which contribute to each mass bin, as well as the average completeness and contamination estimates. As discussed in Section 5, bootstrapping the GSMF means that the estimates for completeness, contamination, and occupation shown are only averages, as they will vary in each realization of the GSMF.

Figure 7 shows our derived GSMF (red circles) and associated Schechter fit for each redshift bin, with a comparison to relevant literature results. For the lower redshift bins, which have the most comparisons in the literature, we split our comparison into observational and simulated results, to aid readability. The shaded regions shown represent the 68% (1σ) uncertainty combining the cosmic variance, Poisson error, and bootstrapping via the mass PDFs. Mass bins with $\leqslant$50% completeness are plotted without a black border. We also show GSMF estimates without completeness corrections applied with red diamonds. We convert the GSMF estimates from the literature to a P. Kroupa (2001) IMF where necessary, using the assumptions of P. Madau & M. Dickinson (2014).

The uncertainty regions are likely underestimated; B. Wang et al. (2024a) argue the statistical uncertainties encoded in the posterior distributions used for bootstrapping the GSMF do not represent the true uncertainty on the stellar mass estimates, due to underlying modeling assumptions, such as the SPS model, IMF, nebular modeling, and assumed SFH. We explore the impact of these assumptions on the GSMF further in Section 6.4.6, showing that alternative GSMF estimates fall outside the uncertainty region.

Table 4 gives the maximum likelihood and median posterior estimates for our Schechter function parameters for each redshift bin. Uncertainties correspond to the 16\84th percentile
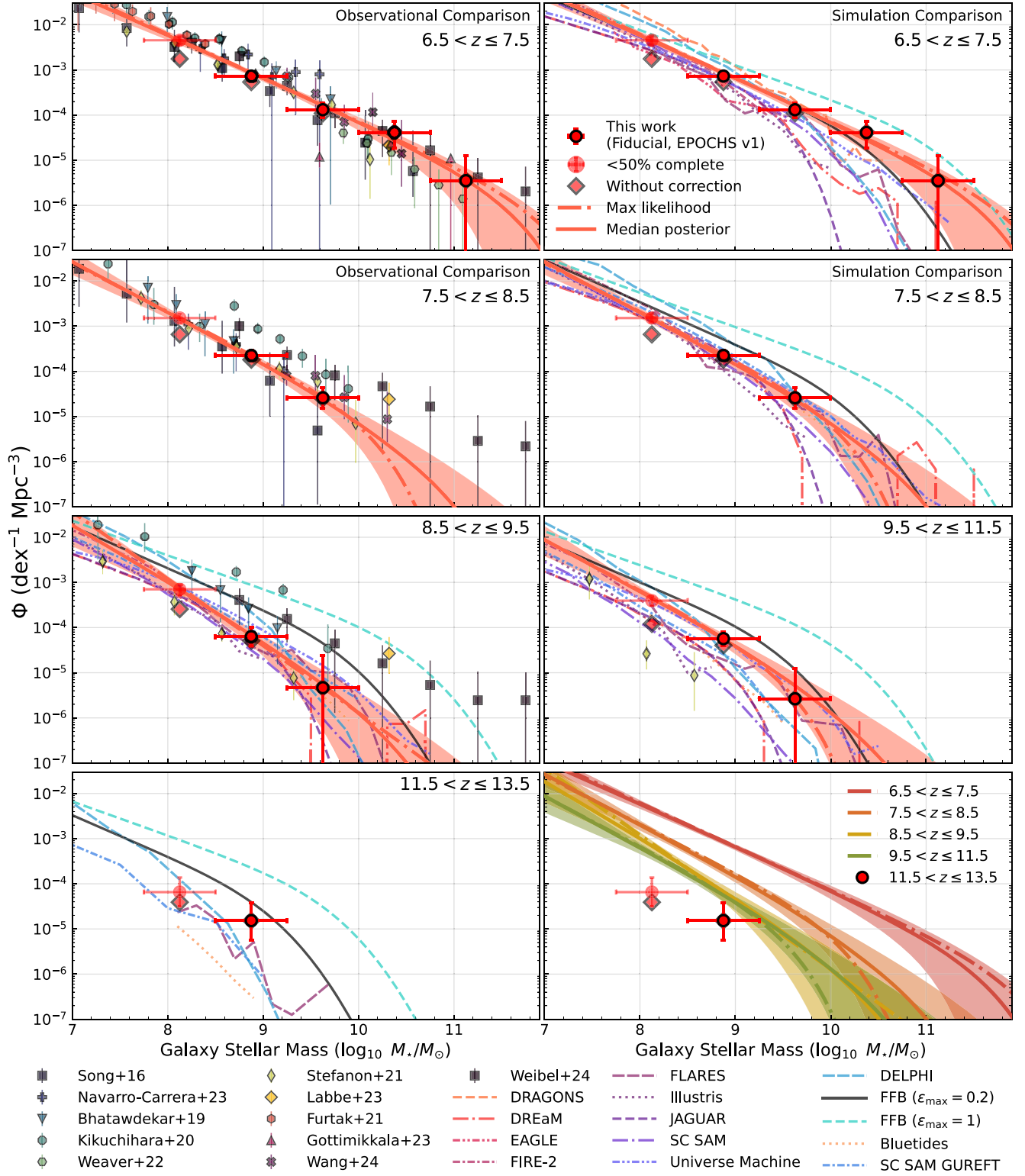
Figure 7. Galaxy stellar mass functions (red markers) and the best-fitting Schechter functions (red solid and dashed–dotted lines indicate the median and maximum likelihood draws from the fit posterior, and the 16th and 84th percentiles are shown by the red shaded region) for the EPOCHS v1 sample derived from the fiducial `Bagpipes` masses and photometric redshifts. We do not fit the $z \sim 12.5$ bin, due to low statistics, uncertain stellar masses, and the potential for high contamination. The bottom right plot shows a comparison of the best-fitting Schechter functions for all redshift bins. Comparison to the following simulations are shown: *BLUETIDES* ($z \leqslant 13$, Y. Feng et al. 2016; S. M. Wilkins et al. 2017), *DRAGONS* ($z \leqslant 7$, S. J. Mutch et al. 2016), *DREaM* ($z \leqslant 10$, N. E. Drakos et al. 2022), *EAGLE* ($z \leqslant 7$, M. Furlong et al. 2015; J. Schaye et al. 2015), *FIRE-2* ($z \leqslant 10$, X. Ma et al. 2018), *FLARES* ($z \leqslant 15$, C. C. Lovell et al. 2021; S. M. Wilkins et al. 2023b), *Illustris* ($z \leqslant 10$, S. Genel et al. 2014), *Jaguar* ($z \leqslant 10$, C. C. Williams et al. 2018), *DELPHI* ($z \leqslant 20$, V. Mauerhofer & P. Dayal 2023), *Santa Cruz SAM (GUREFT*, ($z \leqslant 17$, L. Y. A. Yung et al. 2019, 2024), *Universe Machine* ($z \leqslant 10$, P. Behroozi et al. 2019), and the Feedback Free Burst model of Z. Li et al. (2024; $\epsilon_{max} = 0.2$, $5 \leqslant z \leqslant 20$). We also show the SMF upper limit from Z. Li et al. (2024), assuming a maximum star formation efficiency (ϵ_{max}) of unity. Comparisons to observational results from M. Song et al. (2016), R. Bhatawdekar et al. (2019; disk-like galaxies), S. Kikuchihara et al. (2020), M. Stefanon et al. (2021), L. J. Furtak et al. (2021), J. Weaver et al. (2023), R. Navarro-Carrera et al. (2024), R. Gottumukkala et al. (2024), T. Wang et al. (2024), and A. Weibel et al. (2024). The observational results have been converted to a P. Kroupa (2001) IMF where necessary. In a minority of cases, there is $\Delta z \leqslant 0.5$ between the redshift of our SMF and literature comparisons.
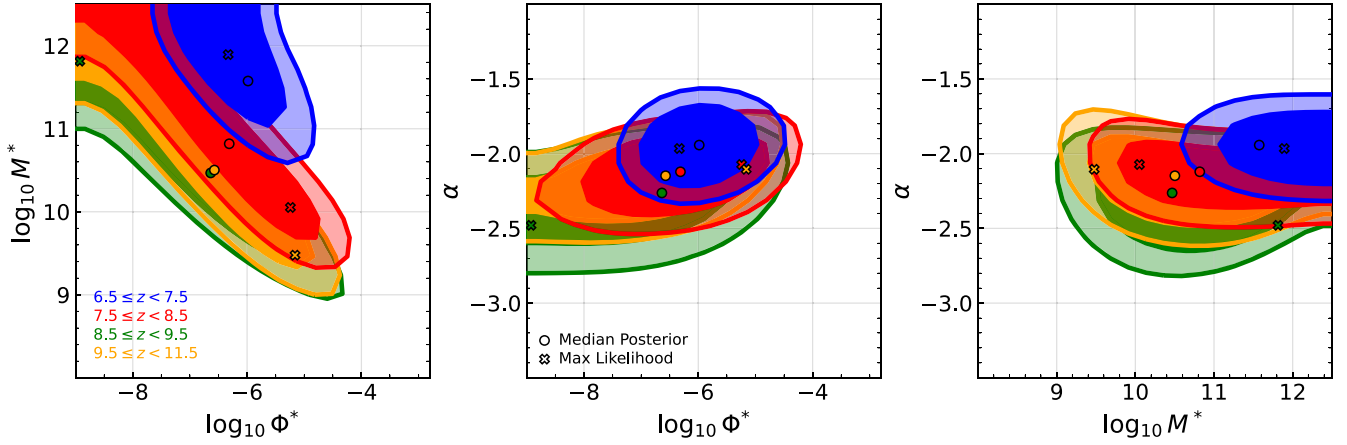
Figure 8. Confidence intervals for our best-fitting Schechter parameters for all fitted redshift bins. Overlaid are the locations of the median posterior value (filled circles) and maximum likelihood draw (filled crosses). Filled (shaded) regions show the 68% (95%) confidence levels.

Table 4
Best-fitting Schechter Function Parameters and Uncertainties Derived from Fitting the Derived GSMF

Redshift Bin	α	$M^\star$	$\log_{10} \phi^\star$
$6.5 < z \leqslant 7.5$	$-1.94^{+0.10}_{-0.10}(-1.97)$	$11.57^{+0.63}_{-0.85}(11.89)$	$-5.98^{+0.87}_{-0.69}(-6.33)$
$7.5 < z \leqslant 8.5$	$-2.12^{+0.18}_{-0.17}(-2.07)$	$10.82^{+1.11}_{-1.07}(10.05)$	$-6.31^{+1.45}_{-1.36}(-5.24)$
$8.5 < z \leqslant 9.5$	$-2.26^{+0.31}_{-0.30}(-2.48)$	$10.47^{+1.15}_{-1.18}(11.81)$	$-6.63^{+1.78}_{-1.50}(-8.93)$
$9.5 < z \leqslant 11.5$	$-2.15^{+0.26}_{-0.22}(-2.10)$	$10.51^{+1.18}_{-1.10}(9.48)$	$-6.58^{+1.61}_{-1.48}(-5.16)$

Notes. We give both the median posterior parameter values (with 1σ uncertainties derived from the 16th–84th percentiles), as well as the values corresponding to the maximum likelihood draw from the posterior (given in brackets). This table is available for download at https://github.com/tHarvey303/EpochsIV.

of each parameter distribution. Figure 8 shows contours that correspond to the 68% (1σ) and 95% (2σ) confidence levels.

Figure 8 shows the covariance of the Schechter parameters for each GSMF fit. A range of parameters are able to fit our GSMF estimates, demonstrating the highly covariant nature of the Schechter parameters. We note that the confidence intervals for the turnover mass, $M^\star$, and the normalization, $\phi^\star$, appear somewhat unconstrained at the high and low ends, respectively. The lack of constraint on $M^\star$ is a consequence of the wide stellar mass bins used and consequential low number of overall mass bins. Wherever we find $M^\star > 11.5$, the GSMF is fit by a pure power law only, and there is no reason to continually extend the prior outside the range where we have available data to constrain $M^\star$.

Figure 9 shows the redshift evolution of these Schechter parameters, with a comparison to those derived in the literature. It is difficult to measure any significant redshift evolution, given the large uncertainty and covariance of the results. We observe some evidence of evolution of the low-mass slope α, which steepens toward higher redshift in all but the highest redshift bin.

In Figures 9 and 8, we see that often our highest-likelihood Schechter function does not coincide with the median posterior, despite the model being fully converged and a large number of posterior sample drawn.

5.6. Stellar Mass Density

The SMD measures the cumulative buildup of stellar mass across cosmic time. This is given by the integration of the stellar mass function $\phi(M, z)$ at a given epoch (redshift) between two limiting masses, as shown in Equation (5). Care must be taken when comparing different estimates of the SMD, as the choice of IMF means mass estimates must be converted; for example, to convert from a G. Chabrier et al. (2000) IMF to a E. E. Salpeter (1955) IMF, masses must be multiplied by a factor of 1.64 (P. Madau & M. Dickinson 2014):

$$\rho_\star(M, z) = \int_{M_l}^{M_u} M\phi(M, z)\, dM. \tag{5}$$

The upper and lower integration limits M_u and M_l are normally taken to be $10^{13} M_\odot$ and $10^8 M_\odot$ (see, e.g., I. Davidzon et al. 2017; R. Bhatawdekar et al. 2019; J. Weaver et al. 2023).

We perform the integration given in Equation (5), where $\phi(M, z)$ is the best-fitting Schechter function fit for each redshift bin. We make use of the quad function from SciPy (P. Virtanen et al. 2020), integrating between $10^8 M_\odot$ and $10^{13} M_\odot$. We compare the integration of both the maximum likelihood fit as well as the median posterior fit. For comparison, we also integrate the best-fitting Schechter functions from the literature in each redshift bin, converting to a P. Kroupa (2001) IMF if necessary.
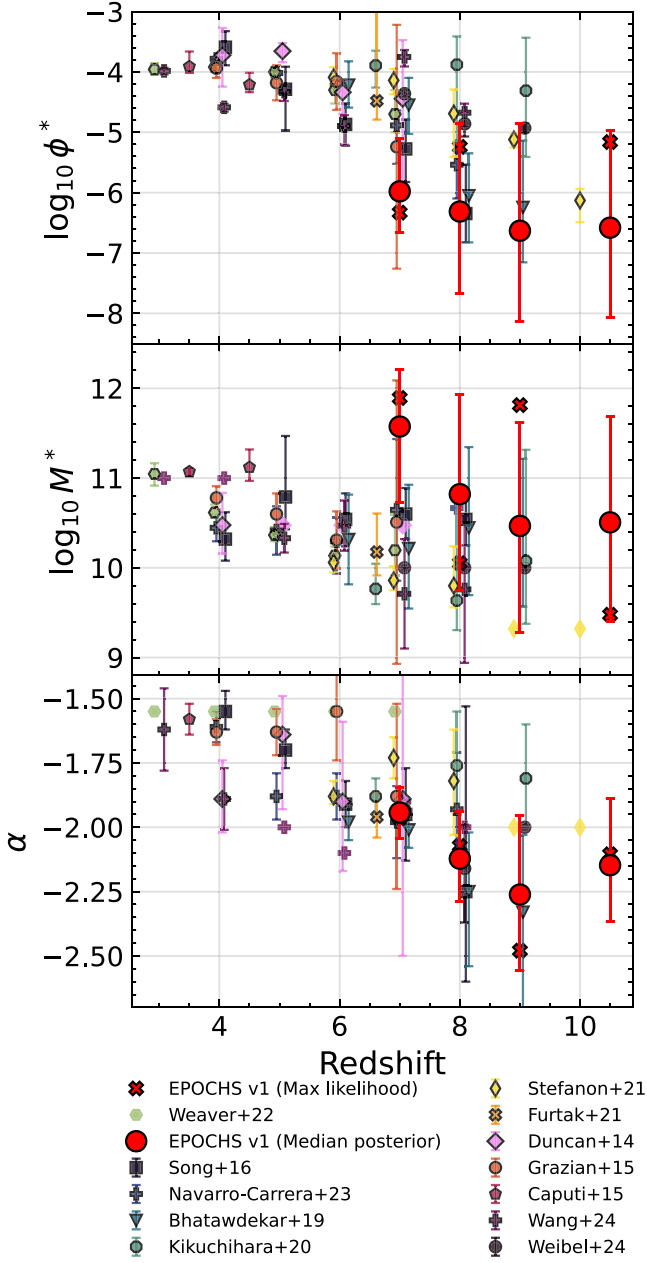
Figure 9. Evolution of best-fitting Schechter function parameters with redshift, with the results of this study shown by the red circles (median posterior) and red crosses (maximum likelihood). Comparisons to K. Duncan et al. (2014), A. Grazian et al. (2015), K. I. Caputi et al. (2015), M. Song et al. (2016), R. Bhatawdekar et al. (2019), S. Kikuchihara et al. (2020), M. Stefanon et al. (2021), L. J. Furtak et al. (2021), J. Weaver et al. (2023), R. Navarro-Carrera et al. (2024), and A. Weibel et al. (2024) are shown. Markers showing literature values without black outlines were fixed during fitting. $M^\star$ values have been adjusted to reflect a P. Kroupa (2001) IMF.

Figure 10 shows our estimate for the SMD at $6.5 \leqslant z \leqslant 11.5$ from integration of the GSMF derived from our fiducial `Bagpipes` mass functions. We show comparisons to observational SMD results at $z \geqslant 5.5$. Estimates of the SMD at $z \leqslant 5$ can be found in the literature (P. Madau & M. Dickinson 2014; S. P. Driver et al. 2018). We also tabulate our SMD values in Table 5.

We integrate all independent posterior draws in order to propagate our mass function uncertainties into the SMD. We show comparisons to predictions and measurements of the
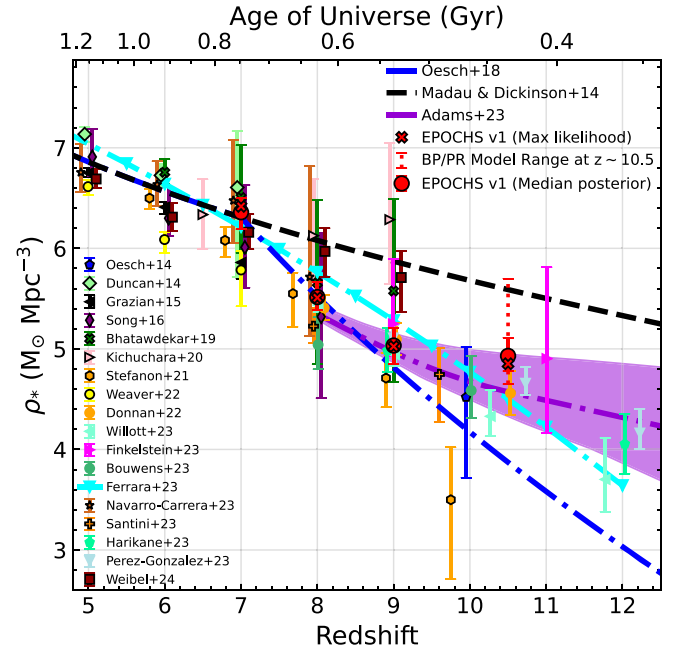
Figure 10. Stellar mass density as a function of redshift derived from the integration of the `Bagpipes` fiducial GSMF. Markers with black borders show comparisons to observational SMD results from P. A. Oesch et al. (2014), K. Duncan et al. (2014), A. Grazian et al. (2015), M. Song et al. (2016), R. Bhatawdekar et al. (2019), S. Kikuchihara et al. (2020), J. Weaver et al. (2023), M. Stefanon et al. (2021), and A. Weibel et al. (2024). Markers with colored borders show the results of integrating the SFRD predictions of JWST-era studies, which include C. T. Donnan et al. (2023), P. Santini et al. (2023), R. Bouwens et al. (2023), S. L. Finkelstein et al. (2024), C. J. Willott et al. (2024), Y. Harikane et al. (2023), and P. G. Pérez-González et al. (2023). Where necessary, we convert literature results to a P. Kroupa (2001) IMF. Markers may be shifted by up to $\Delta z = 0.1$ for clarity. We also show the theoretical predictions of the P. Madau & F. Haardt (2015; constant star formation efficiency) and P. A. Oesch et al. (2018; DM halo evolution) models, as well as the model of A. Ferrara et al. (2023). The purple-shaded area shows the integral of the SFRD presented by N. J. Adams et al. (2024) for our sample, which is consistent with the SMD derived from our `Bagpipes` SED fitting. The red dotted errorbar at $z \sim 10.5$ shows the SMD range we find using different SED-fitting tools and models, calculated from the Schechter fits in Figure 12. We do not show the range of models at every redshift, but it typically exceeds the uncertainty derived from the fit itself.

cosmic star formation rate density (SFRD, ψ) using Equation (6) from P. Madau & M. Dickinson (2014) in order to estimate the inferred SMD:

$$\rho_\star(z) = (1 - R) \int_z^\infty \psi \frac{dz}{H(z')(1 + z')}. \tag{6}$$

The return fraction R is estimated as 0.423 under the assumptions of P. Madau & M. Dickinson (2014) for a P. Kroupa (2001) IMF (a well-mixed closed-box model with constant IMF and metal yield and instantaneous recycling of metals). We integrate the predictions of P. Madau & M. Dickinson (2014) and P. A. Oesch et al. (2018) and the UV luminosity density derived results of N. J. Adams et al. (2024), as well as other JWST-era measurements. For N. J. Adams et al. (2023), we propagate uncertainties in the inferred SMD via a Monte Carlo integration of their SFRD measurements and uncertainties. Star formation is assumed to begin at $z = 20$, but the results are relatively insensitive to the exact formation redshift as long as it exceeds the redshift $z \geqslant 13.5$ limit used in this work.

Table 5
Stellar Mass Density Results from Our Fiducial `Bagpipes` SED Fits for Each Redshift Bin

Redshift Bin	$\rho_{\star}$ ($\log_{10} M_{\odot}$ Mpc^{-3})
$6.5 < z \leqslant 7.5$	$6.36^{+0.14}_{-0.17}(6.42)$
$7.5 < z \leqslant 8.5$	$5.52^{+0.14}_{-0.13}(5.51)$
$8.5 < z \leqslant 9.5$	$5.03^{+0.18}_{-0.18}(5.02)$
$9.5 < z \leqslant 11.5$	$4.93^{+0.18}_{-0.15}(4.85)$

Notes. Values with uncertainties come from the 16th, 50th, and 84th percentiles of the posterior, and values in brackets are for the highest-likelihood Schechter function. This table is available for download at https://github.com/tHarvey303/EpochsIV.

The inferred SMD is heavily dependent on the best-fitting Schechter function, and therefore indirectly dependent on the GSMF and stellar mass estimates. For the alternative GSMF estimates in Figure 12, we find that the use of the "continuity bursty" SFH, or stellar masses derived with our `Prospector` fitting, can increase the SMD at redshift 10.5 by up to 0.75 dex, which is shown with a dashed errorbar. Similar variations are possible in the other redshift bins, but for simplicity we do not show every alternate GSMF and SMD derived for all redshift bins.

6. Discussion

We have presented our fiducial GSMF using `Bagpipes` at redshifts $6.5 \leqslant z \leqslant 13.5$, finding a steep low-mass slope ($\alpha \lesssim -1.95$ and a high stellar mass exponential cutoff ($M^{\star} \gtrsim 10.5$) in all redshift bins. We have also estimated the SMD implied by our results, finding an apparent flattening of the SMD at $z > 9$. In the following section, we will discuss our results in the context of theory and previous work. This includes examining the uncertainties in the GSMF derived from our other SED-fitting results, as well as considering how a modified top-heavy IMF or contamination by hidden AGN would affect our results.

6.1. Massive Galaxies in the Early Universe

Numerous studies have reported an excess of galaxies with high inferred stellar mass at high redshift (H. B. Akins et al. 2023; R. Endsley et al. 2023a; I. Labbé et al. 2023; M. Xiao et al. 2024). If galaxies of the inferred masses do exist in the number densities implied by these studies, this could represent a challenge to ΛCDM cosmology or our understanding of high-redshift galaxy astrophysics, given the available timescale and available gas reservoirs (M. Boylan-Kolchin 2023; I. Labbé et al. 2023; C. C. Lovell et al. 2023).

In order to test whether our derived stellar mass and redshift estimates are in tension with ΛCDM, we use the Extreme Value Statistics (EVS) approach, presented in C. C. Lovell et al. (2023) and available online.[32] We follow the methodology of C. C. Lovell et al. (2023) throughout this section. EVS is a method for predicting the distribution of the most extreme values from a given distribution. In this case, we use a parameterization of the high-z halo mass function (P. S. Behroozi et al. 2013), and predict the PDF of the highest-mass halo in some volume (given by a redshift interval, sky fraction, and assumed cosmology).
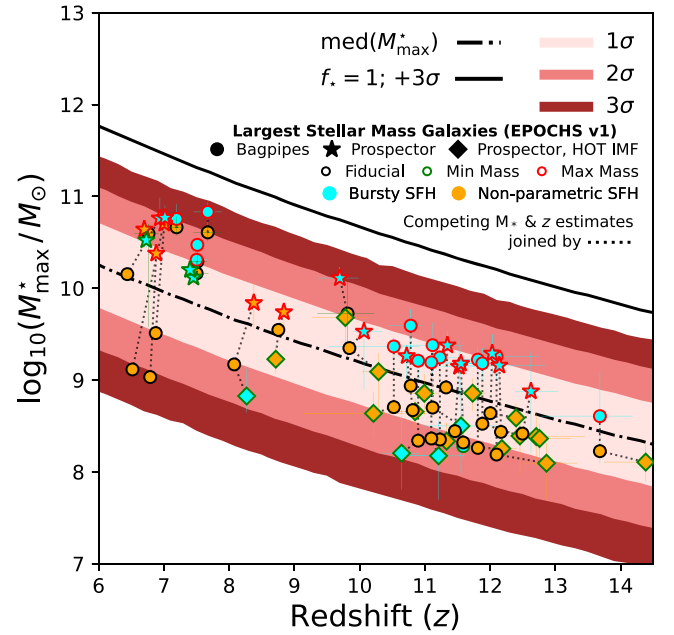
---

[32] https://github.com/christopherlovell/evstats

Figure 11. Photometric redshifts and stellar mass estimates for the most massive galaxies in the EPOCHS v1 galaxy sample. We use the extreme value statistics methodology of C. C. Lovell et al. (2023) to place constraints on the most massive galaxy at a given redshift expected for our given survey area (187 arcmin^2) and a fiducial ΛCDM cosmology (with fixed baryon fraction of 0.16; Planck Collaboration et al. 2016). The contours show the upper and lower limits for the most massive galaxy, assuming a truncated log-normal distribution for the stellar fraction, with the median shown by the dashed–dotted line. The solid line shows the extreme upper 3σ limit, assuming a stellar fraction of unity. For galaxies in the EPOCHS v1 sample with a stellar mass estimate greater than $1.5\times$ the limit for a realistic stellar fraction (dashed–dotted line), we show the maximum, minimum, and fiducial stellar mass and redshift estimates for our `Bagpipes` and `Prospector` fits, joined with a dotted black line. The shapes and colors of the points indicate the SED-fitting tool, SFH, and IMF used, as explained by the inset legend. No galaxies exceed the maximum stellar mass predicted by ΛCDM, although some galaxies do require a high stellar fraction, in particular the "little red dots" with high inferred masses at $z \sim 7$.

Figure 11 shows these individual PDF contours projected into the mass-redshift plane. We show the 1σ, 2σ, and 3σ contours around the median prediction for the most massive galaxy at a given redshift with a dotted–dashed line and shaded contours. A unique aspect of the EVS approach is that it predicts both upper and lower bounds to the most massive object; the most massive galaxy can be too small for the assumed cosmology and astrophysics, as well as too massive. A universal baryon fraction of 0.16 is assumed, based on cosmological results (Planck Collaboration et al. 2016), and we compute the EVS limits for a range of stellar fractions (the fraction of baryons that form stars). In Figure 11, we show the 3σ upper limit, assuming a stellar fraction of unity, with a solid black line.

Overlaid on Figure 11, we show the SED-fitting-derived redshifts and corrected stellar masses for our sample. We correct our derived stellar masses for Eddington bias (A. S. Eddington 1913) following $\ln M_{\mathrm{Edd}} = \ln M_{\mathrm{obs}} + \frac{1}{2}\epsilon\sigma^2_{\ln M}$. Here, $\ln M_{\mathrm{obs}}$ is the stellar mass estimate, $\sigma_{\ln M}$ is the uncertainty in the stellar mass taken from the posterior PDF, and ϵ is the local slope of the halo mass function. C. K. Jespersen et al. (2024) look at the impact of cosmic variance on the predictions of EVS, as this is not accounted for in the method of C. C. Lovell et al. (2023) we use here. Given that our sample consists of multiple widely separated

fields, we do not believe cosmic variance will play a significant role on this EVS analysis. No galaxies in our sample fall above the 3σ limit, given a stellar fraction of unity, shown with a black line, which would require more stellar mass than the available baryons to form stars. For galaxies with redshift and stellar mass estimates that place them in possible tension with the EVS limits, assuming a realistic stellar fraction (more than $1.5\times$ the mean value of the log-normal distribution, shown by the dashed–dotted line in Figure 11), we show the individual mass measurements on the figure. Galaxies below this limit are not shown. For each of these galaxies, we show the "fiducial" `Bagpipes` photo-z and stellar mass, as well as the maximum and minimum stellar mass estimate for that galaxy in our `Bagpipes` and `Prospector` fitting, including the modified IMF results we discuss in Section 4.4. We link individual mass estimates for the same object with dotted lines. In the majority of cases, while the maximum stellar mass estimate may suggest a possible tension, the minimum and often the fiducial mass estimates are not in tension.

It is worth noting that all galaxies that show a possible tension at redshift $z \leqslant 8$ in this figure are classed as "little red dots" (LRDs), which are discussed further in Section 5.2.3 and potentially contain a significant AGN component we do not account for. The mass estimates for these galaxies may be overestimated by up to 1 dex (C. C. Williams et al. 2024), as it is impossible to disentangle the relative contributions of stellar and AGN emission to the broadband photometry, and difficult even with spectroscopy (e.g., B. Wang et al. 2024b). It is clear from Figure 11 that none of our candidates are in tension with the predictions of ΛCDM, as seen by the lack of sources above the solid black line; however, a number of objects do require very high stellar fractions at these redshifts. The galaxies that require the highest star formation efficiencies seem to be found at $z \sim 7$–8, rather than the higher redshift probed in this study. This has also been found for HST-dark galaxies observed as part of FRESCO, where the galaxies with highest implied stellar mass densities are between $5 \geqslant z \geqslant 6$ (M. Xiao et al. 2024).

Further evidence for the compatibility of our results with standard cosmological models can be seen in Figure 7, where we are below the SMF upper limit calculated by Z. Li et al. (2024) in all redshift bins, which is shown with a black line. Z. Li et al. (2024) present a bursty SFH model consisting of a series of feedback-free bursts (on timescales of ~ 10 Myr per burst) for galaxies in halos above a given mass/redshift cutoff, resulting in higher star formation efficiency, cosmic SFR density, and SMD above $z \geqslant 8$. The upper limit shown is computed assuming a maximum star formation efficiency ($\epsilon_{\max}$) of unity. Our fiducial GSMF results at $z \approx 7$ are close to the Feedback Free Burst (FFB) model predictions with $\epsilon_{\max} = 0.2$, but fall below this value at higher redshifts.

T. Wang et al. (2024) have shown that stellar masses of high-mass galaxies are typically overestimated by ~ 0.4 dex when $>1 \mu$m rest-frame emission is not used in SED fitting, which requires MIRI observations in this redshift regime, and as much as 0.6–1 dex for the reddest sources (C. C. Williams et al. 2024). As MIRI observations are not used in this study, the degeneracies in age–attenuation and the relative contributions of strong emission lines and the stellar continuum observed by T. Wang et al. (2024) are not constrained, possibly leading to an overestimation in stellar mass. Outshining and stochastic star formation are, however, still likely to have an effect on

stellar masses derived from SED fitting, even when MIRI data are used (X. Shen et al. 2023; D. Narayanan et al. 2024), and the derived discrepancy in stellar mass without MIRI will likely depend on the assumed SFH, dust law, and parameter priors, as we have shown they can also systematically change stellar mass estimates. T. Wang et al. (2024) also find that high-mass galaxies at $6 \leqslant z \leqslant 8$ may require a higher star formation efficiency ($\epsilon \sim 0.3$) than the local Universe, but they do not find any incompatibility with standard cosmological models. Alternative explanations that do not require high SFE, such as a blue-tilted primordial power spectrum, have also been proposed in the literature (e.g., P. Parashari & R. Laha 2023).

In Figure 2, we show examples of the photometry, best-fitting `Bagpipes` and `Prospector` SEDs, and posterior redshift and stellar mass estimates for a few of the most massive galaxies in the EPOCHS v1 sample at a range of redshifts. For the galaxy labeled *CEERSP1:7463*, which is representative of the LRDs we observe, the inferred SFH for the nonparametric SED fits suggest the bulk of stellar mass was formed ~ 100–200 Myr ago, which may put it and some of the other high-mass LRD galaxies in greater tension at ΛCDM at earlier points in their SFHs, if the integrated SFH is considered. However, as we discuss in Section 6.2, the masses and SFHs of the LRDs are highly uncertain, in particular when they contribution of AGN is not considered.

6.2. Contamination of the GSMF by Hidden AGN

The study by I. Labbé et al. (2023) discovered unexpectedly massive, high-redshift galaxies in the CEERS field, known as "little red dots," as discussed in Section 5.2.3. V. Kokorev et al. (2024) used similar selection criteria to extend this to the GOODS-S field. In this section, we compare our photometric redshifts and mass estimates, and investigate the impact on the GSMF. We cross-matched their 13 candidates with our catalog to compare masses and redshifts. Of these, 11 are in our catalog, seven of which meet our selection criteria and are among the most massive galaxies we identified. Two candidates were not recovered, due to blending with neighboring sources in our `SExtractor` segmentation maps. Four others we detected but did not select: *5346_CEERSP6 (11184)* is near a detector gap, and the other three did not meet our UV signal-to-noise requirement. Notably, *2683_CEERSP3 (13050)* is a spectroscopically confirmed broad-line AGN at $z = 5.6$ (D. D. Kocevski et al. 2023).

We did not detect *37888* or *39575*, the lowest-mass candidates in I. Labbé et al. (2023), as they were blended with neighbors. Two galaxies were excluded from our study because their redshifts were below our limit. For these, we found lower redshifts than I. Labbé et al. (2023): *8750_CEERSP3 (7274)* at $6.03^{+0.36}_{-0.14}$ and *2499_CEERSP1 (25666)* at $6.45^{+0.10}_{-0.18}$. For five galaxies, our photo-z estimates matched well, except for *1516_CEERSP2 (21834)*, where our estimate was $z = 10.4^{+1.3}_{-0.6}$ with `EAZY-py`, differing from `Bagpipes`, which found $z = 8.63^{+0.24}_{-0.32}$, aligning with their result of $z = 8.54^{+0.32}_{-0.51}$. On average, our stellar mass estimates are $2.1\times$ smaller than those of I. Labbé et al. (2023), largely due to differing IMFs. The most massive candidate, *7463_CEERSP1 (38094)*, with a stellar mass of $\log_{10}(M_\star/M_\odot) = 10.89^{+0.09}_{-0.08}$, is the second-most massive in our sample, with a `Bagpipes` mass of $10.65^{+0.09}_{-0.10}$. Given our larger survey area, this suggests the CEERS field might be overdense, as suggested by G. Desprez et al. (2024). We computed the GSMF implied by I. Labbé

et al. (2023), showing their data points at $z = 8$ and $z = 9$ are above our best-fitting Schechter functions, due to smaller cosmic volume and higher stellar masses. T. Wang et al. (2024) show that including MIRI data in SED fitting reduces high-z galaxy masses by ~ 0.4 dex, indicating potential overestimation without MIRI data. When comparing to I. Labbé et al. (2023), we find eight of their CEERS and GOODS-South candidates in our robust sample, with 28 more being detected but below our $z < 6.5$ cutoff or below our rest-UV SNR requirements. We see good agreement in redshift, with a maximum offset of $\Delta z \approx 0.4$, and a mean offset of $\Delta z \approx 0.14$. These galaxies are found to have high stellar masses in our SED fitting, with a median stellar mass of $\log_{10} M_\star / M_\odot = 10.30$ in our fiducial `Bagpipes` results, with five of them forming the most massive galaxies in our fiducial sample. They are all at $z \leqslant 8$ in our sample. Further observations with NIRSpec or MIRI are essential to ascertain the true nature of these sources. In Appendix B, we recompute the $z = 7$ GSMF without any LRDs and show that these sources dominate the high-mass end of the GSMF. J. C. D'Silva et al. (2023) have shown that accounting for the contribution of AGN lowers the cosmic star formation rate density by 0.4 dex at $z \geqslant 9.5$, which will also lower the inferred SMD, and they have found that a significant fraction of the LRDs are hidden AGN.

Our sample is primarily selected in the rest-frame UV, potentially missing galaxies with weak UV emission but significant stellar mass, such as submillimeter galaxies. These high-mass but low-spatial-density galaxies are excluded from our selection. Additionally, our high-resolution detection favors compact, high-surface-brightness sources over extended, low-surface-brightness ones, possibly excluding a population of extended, diffuse galaxies at these redshifts.

6.3. Impact of Modified IMF

Our modified top-heavy IMF implementation in `Prospector` reduces masses by up to ~ 0.5 dex for galaxies at $z \geqslant 12$ (HOT 60K) compared to the standard P. Kroupa (2001) IMF, as shown in Figure 4 . The mass decrease depends on the star formation model, with a larger reduction seen in the parametric "delayed" SFH model (0.46 dex) compared to the nonparametric "continuity bursty" SFH model (0.35 dex). The best-fitting models show the χ^2 is almost unaffected by the IMF change, indicating the modified IMF models match the observed photometry as well as the original data. For the modified IMF model used at $8 \leqslant z \leqslant 12$ (HOT 45K), we see smaller mass decreases (≈ 0.3 dex).

Comparable studies also examine the impact of a top-heavy IMF on high-redshift galaxy masses. C. L. Steinhardt et al. (2023), using the same top-heavy IMF model with a different SED-fitting tool, observed decreases of 0.5–1 dex in stellar mass, while our implementation shows smaller decreases of 0.3–0.5 dex. This discrepancy may be due to differences between the standard `EAZY-py` templates and their models, or variations in SFHs resulting from the IMF change. C. Woodrum et al. (2023) also studied top-heavy IMF modifications using `Prospector`, focusing on a modification to the G. Chabrier et al. (2000) IMF rather than P. Kroupa (2001). They found similar reductions in stellar mass (0.38–0.5 dex) with no change in the goodness of fit.

Our analysis shows that a modified top-heavy IMF can decrease the stellar masses of high-z galaxies without altering the simulated photometry. However, our examination of the

ΛCDM limits on stellar mass growth (Section 6.1) does not require a nonstandard IMF for compatibility with ΛCDM. As shown in Figure 1, stellar masses can vary significantly with other SED-fitting assumptions (e.g., dust law and assumed SFH) before considering any IMF changes. For galaxies with high stellar masses across all models, it is challenging to distinguish between a modified IMF and high star formation efficiency based on photometry alone.

6.4. Comparing the Measured GSMF with Other Observations and Theory/Simulations

In Figure 7, we compare our GSMF estimates to a wide range of observational and theoretical/simulation-based predictions of the GSMF. Here, we briefly discuss our GSMF estimates for each of the redshift bins. In order to make direct comparisons, where necessary, all results have been converted to use a P. Kroupa (2001) IMF. The overall evolution of the derived Schechter parameters and a comparison to the results derived by other studies can be seen in Figure 9. While the Schechter parameters are highly covariant and our results typically have large uncertainties, we observe an evolution in α and $\phi^\star$, with both parameters decreasing compared to the results at $z \sim 4$ of K. I. Caputi et al. (2015), K. Duncan et al. (2014), and A. Grazian et al. (2015). We see little evolution of $M^\star$ within the large range of uncertainties.

6.4.1. Redshift z = 7 GSMF

We derive a mass function at $z \sim 7$, primarily as a proof of concept of our method. We do not take advantage of galaxy lensing in this work, so any reasonable mass completeness limit is higher than previous studies, nor do we have the area of wide-field studies like J. Weaver et al. (2023) in order to detect rare, bright, and high-mass galaxies. However, with JWST, we have seen a surprising excess of UV-faint LRD-like objects with high inferred stellar masses, as discussed in Section 6.2. The majority of these sources were previously undetected with HST, due to relatively weak Lyman breaks, and so do not appear in pre-JWST stellar mass estimates. Their inclusion in our GSMF has resulted in an excess at the high-mass end of the GSMF when compared to other observational studies, and consequently a higher and poorly constrained estimate of $M^\star$, as we see little evidence for any exponential turnover. The highest-mass GSMF data points of J. Weaver et al. (2023) fall within our 1σ uncertainty region, but our results are significantly above the measurements of M. Stefanon et al. (2021). At the low-mass end, we fall below the results of S. Kikuchihara et al. (2020) and R. Navarro-Carrera et al. (2024), but agree within the uncertainties of L. J. Furtak et al. (2021) and R. Bhatawdekar et al. (2019). The works of M. Stefanon et al. (2021), S. Kikuchihara et al. (2020), R. Bhatawdekar et al. (2019), and L. J. Furtak et al. (2021) are all based on HST+Spitzer observations of the HFF, and they incorporate lensing, which means they probe the low-mass end of the GSMF more accurately then this study. Our low-mass slope $\alpha = -1.94^{+0.1}_{-0.1}$ is in good agreement with L. J. Furtak et al. (2021), but steeper than the results of M. Stefanon et al. (2021) and S. Kikuchihara et al. (2020). At the time of writing, R. Navarro-Carrera et al. (2024), R. Gottumukkala et al. (2024), T. Wang et al. (2024), and A. Weibel et al. (2024) are the only other studies to incorporate JWST observations into their GSMF estimates. We see reasonable agreement with the

results of R. Navarro-Carrera et al. (2024), as our data are within their GSMF uncertainties. This work relies almost entirely on JWST observations, whereas they combine deep JWST observations of small volumes ($\leqslant$20 arcmin^2) with HST and ground-based catalogs. These ground-based data allows them to find more rare, high-mass galaxies than our study, but at lower masses, the small volumes probed with their JWST data are potentially vulnerable to cosmic variance. Reliance on ground-based and HST data also limits the maximum redshift they can probe to $z \leqslant 8$. T. Wang et al. (2024) use PRIMER observations with NIRCam and MIRI to measure the GSMF, notably finding that the use of MIRI observations systematically reduces stellar masses measured with SED fitting. We see good agreement in the measured GSMF within the uncertainties of both studies, despite this work not incorporating MIRI data or correcting for any systematic offset in mass arising from the lack of rest frame $>1\,\mu$m observations. Our GSMF does extend to higher stellar mass than the results of T. Wang et al. (2024), resulting in a higher value for $M^\star$, as can be seen in Figure 9.

R. Gottumukkala et al. (2024) examine the contribution of high-mass, dusty galaxies at $3 < z < 8$ to the GSMF using data from the CEERS survey. Given that our GSMF probes a wider galaxy population, we do not expect to see overlap at all stellar masses. We see good overlap at the highest stellar masses $M_\odot \sim 10^{10.5}$, where our SMF estimate is dominated by dusty LRD galaxies (as discussed in Section 6.2). At $z = 7$, we see good agreement with A. Weibel et al. (2024), who construct the GSMF at $4 \leqslant z \leqslant 9$ using data from JADES, CEERS, and PRIMER.

When we compare our results to predictions from models and simulations, we see agreement with the majority of models at the low-mass end but a significant excess at higher masses that is not reproduced by any of the models. We find in particular that the JAGUAR model we use for our completeness simulations shows a more rapid decline at high stellar mass than the other models, but given that we are not reliant on our completeness correction in this mass regime, this does not impact our estimate of the GSMF. We are closest to the prediction of *Universe Machine* (P. Behroozi et al. 2019) at the highest stellar mass bin.

6.4.2. Redshift z = 8 GSMF

Our fiducial GSMF estimate at $z \sim 8$ shows reasonable agreement with most predictions. As we do not bootstrap in redshift when constructing the GSMF, we do not account for galaxies scattering between redshift bins: for example, a galaxy found to be at $z = 7.49$ with Bagpipes would contribute only to the $z = 7$ GSMF, even if a significant fraction of the redshift PDF is above $z \geqslant 7.50$. This does not affect the majority of galaxies within our sample, but it does explain some of the discrepancy between our results and the implied results of I. Labbé et al. (2023), shown in purple in Figure 7, assuming 100% completeness. The LRD galaxies of I. Labbé et al. (2023) that we also select are all found to be at $z \leqslant 7.5$, meaning they do not contribute at all to our estimate of the $z = 8$ GSMF. The best-fitting redshift for these objects in some cases is quite close to this boundary, however, meaning that these objects could theoretically contribute to the $z = 8$ GSMF instead, which would boost the high-mass end significantly. Our GSMF is also lower than the results of S. Kikuchihara et al. (2020), which incorporates strong gravitational lensing in order to

probe to lower stellar mass. Our GSMF agrees with the results of M. Song et al. (2016), R. Bhatawdekar et al. (2019), and M. Stefanon et al. (2021), and appears to validate the majority of pre-JWST GSMF estimates. We can also draw a comparison to the results of T. Wang et al. (2024), whose GSMF results at $z = 8$ are systematically above our results, but within the derived uncertainties of both studies. We are also below the results of A. Weibel et al. (2024).

We see good agreement with most theoretical predictions of the GSMF at this redshift, with *Universe Machine* (P. Behroozi et al. 2019), *SC SAM GUREFT* (L. Y. A. Yung et al. 2024), and *FLARES* (C. C. Lovell et al. 2021; S. M. Wilkins et al. 2023b) having the most similar results.

6.4.3. Redshift z = 9 GSMF

Our GSMF estimate at $z \sim 9$ is below the results of R. Bhatawdekar et al. (2019) and S. Kikuchihara et al. (2020), but within the uncertainties of M. Stefanon et al. (2021). We are below the implied result of I. Labbé et al. (2023), which is derived from two galaxies in their sample in this redshift bin, but assuming 100% completeness. We include one of these galaxies in our GSMF at this redshift, as the other does not meet our selection criteria, because we do not detect the Lyman break at 5σ. We additionally include one other candidate from their sample in this GSMF, as our fiducial Bagpipes photo-z places it within this redshift bin, rather than the $z \sim 8$ redshift bin based on their photo-z. For both of their galaxies we do include in this redshift bin, we find ~ 0.4 dex lower stellar masses, meaning they contribute to a lower stellar mass bin. Our reliance on the rest-frame UV to robustly detect sources is one limitation of this work, although the increased depth of JWST observations when compared to HST has reduced this in some fields. We investigated less-stringent constraints on the Lyman-break, but found that this dramatically increased rates of contamination within our sample. We are also below the results of A. Weibel et al. (2024), but within the uncertainties where they consider their $z = 9$ GSMF reliable, at $8.5 \leqslant \log_{10}(M_\star/M_\odot) \leqslant 9.5$, as they suspect low-$z$ contamination at higher inferred masses. When compared to simulations, *FLARES* and *Universe Machine* are close to our GSMF estimate, but almost all the predictions are within our posterior region. Interestingly, in this redshift bin, we are below the predictions of two recent JWST-era studies, namely V. Mauerhofer & P. Dayal (2023) and Z. Li et al. (2024), both of which incorporate higher star formation efficiencies than typical models.

6.4.4. Redshift z = 10.5 GSMF

At $z \sim 10.5$, observational comparisons can be made only to the pre-JWST results of M. Stefanon et al. (2021). In comparison to their results, we find a significant excess of high-mass galaxies in our observations. Our results show that, above $z \geqslant 10$, JWST observations are essential to accurately sample the high-z galaxy population. Our results are above the majority of theoretical and simulation-derived predictions, but do show good agreement with *Universe Machine* (P. Behroozi et al. 2019) and *FLARES* (C. C. Lovell et al. 2021; S. M. Wilkins et al. 2023b).

6.4.5. Redshift z = 12.5 GSMF

In our highest redshift bin, $11.5 < z \leqslant 13.5$, which covers only ≈ 80 Myr, there are no published observationally derived results and few theoretical or simulation-based GSMF comparisons at this redshift. Pre-JWST estimates of the GSMF were not possible at this redshift, and even with JWST, our GSMF estimate is also uncertain due to the difficulty in accurate stellar mass estimates as well as the possible contribution of contaminants. At $z = 12.5$, the longest-wavelength NIRCam filter falls within the rest-frame UV, which is dominated by young stars, leading to highly uncertain SFHs and stellar masses. As we explored briefly in Section 4.4, the more likely possibility of a top-heavy IMF or exotic stellar populations in these early galaxies further increases the systematic uncertainties in the stellar mass estimates. As an example, three galaxies within this redshift bin are shown in the lower plot of Figure 2 and in Figure 3. The range of stellar mass estimates (~ 0.8–1 dex) for different Bagpipes and Prospector SEDs with very little difference in the fitted rest-UV spectra shows the difficulty in estimating stellar mass at these redshifts. Previous studies at lower redshift with HST and Spitzer have found that stellar masses estimated by HST alone, with no measurement of the rest optical emission, typically underestimate stellar masses by 0.62 dex, compared to measurements including HST and Spitzer NIR observations (L. J. Furtak et al. 2021). At this redshift range, our JWST NIRCam observations are probing comparable rest-frame UV wavelengths to HST observations at $z \sim 6$–7, and it possible that our stellar masses are also underestimated unless there is a significant change in stellar populations or IMF. The possibility of more stochastic SFHs at this redshift compared to $z \sim 6$–7 may also lead to outshining, which further increases the stellar mass discrepancy (D. Narayanan et al. 2024). In order to test whether the reliance of the rest UV is impacting the stellar masses compared to lower redshifts, we refit all galaxies using Bagpipes in the $z = 9$ bin without F410M or F444W, which gives rest-frame coverage equivalent to that of a $z = 12$ galaxy. We see no systematic shift in the stellar masses, with a median offset of 0.07 dex and a standard deviation of 0.3 dex, when comparing to the stellar mass estimate including the longer-wavelengths filters.

We note that several galaxies in this bin have been excluded from the GSMF in this case, due to our requirement that the contamination is less than 50%. The inclusion of these possible contaminants would result in an ≈ 0.3 dex increase in the lowest-mass bin. The results of this are shown in Appendix D. While we do not attempt to fit the GSMF, we can make approximate comparisons to the few available predictions. We see the closest agreement with *DELPHI* (V. Mauerhofer & P. Dayal 2023) and are within 1.5σ of *FLARES* (C. C. Lovell et al. 2021; S. M. Wilkins et al. 2023b) in the higher-mass bin, but have an excess of $\approx 10^8 \, M_\odot$ galaxies when comparing to *FLARES* and *SC SAM GUREFT* (L. Y. A. Yung et al. 2024). Our results are significantly above the predictions of *BLUE-TIDES* (Y. Feng et al. 2016; S. M. Wilkins et al. 2017) at all stellar masses. Our fiducial GSMF prediction is slightly below the prediction of Z. Li et al. (2024) with maximum star formation efficiency $\epsilon_{max} = 0.2$, and significantly below the upper limit of $\epsilon_{max} = 1$.
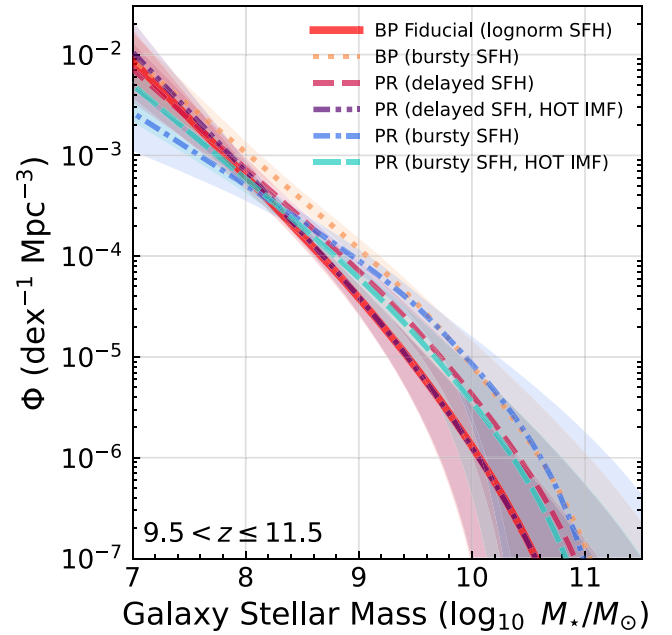

Figure 12. GSMF Schechter parameterization for the $z \sim 10.5$ redshift bin derived for our fiducial Bagpipes SED-fitting compared to alternative GSMF estimates. We show the GSMF derived using Bagpipes with the nonparametric "continuity bursty" SFH (labeled "bursty") as well as two GSMFs derived using Prospector SED fitting for a parametric and a nonparametric SFH. For comparison, we also show the GSMF inferred with the alternative top-heavy IMF model. The derived GSMF is clearly dependent on the choice of model and SED-fitting tool, with the "continuity bursty" SFH model typically shifting the GSMF toward higher stellar mass. These Schechter functions are tabulated in Appendix C.

6.4.6. Alternative GSMF Estimates

Following on from the comparison of galaxy stellar mass estimates with different choices of SFH and priors in Section 4.3, it is possible to estimate the GSMF for any of the different SED-fitting models. A full comparison of the derived GSMF for every model, given the many possible combinations of possible IMF and SFH models, is beyond the scope of this work, but we give a representative example of the GSMF derived at $z \sim 10.5$ for the models that show the most variation in stellar mass when compared to our fiducial Bagpipes fitting. Here, we choose to investigate the GSMF dependence on the chosen SFH model and SED-fitting tool, rather than the choice of parameter prior or dust law. This is because, in Section 4.3, there was larger variation in stellar mass with little variation in χ^2 for these alternative models. Additionally, as discussed, the use of nonparametric SFHs is more common in the literature (e.g., S. Tacchella et al. 2022; C. Giménez-Arteaga et al. 2023, 2024; S. Jain et al. 2024) for high-z galaxies, due to problems such as outshining.

We derive these GSMF estimates using the same method as described in Section 5 for the fiducial Bagpipes GSMF, replacing the stellar mass PDFs, best-fitting SEDs, and redshift estimates with those of the chosen model. Figure 12 shows a comparison of the fiducial Bagpipes GSMF to a GSMF derived from the "continuity bursty" nonparametric SFH model, which increases the stellar mass estimates by 0.2 dex on average, but $\geqslant 1$ dex in some cases. This results in the largest change in the overall GSMF when compared to the fiducial Bagpipes result.

We also show mass functions derived from our `Prospector` SED fitting, which are offset above our fiducial `Bagpipes` GSMF for both the parametric and nonparametric results. These results are somewhat comparable to the spread seen in the `Bagpipes` results, although the low-mass end of the GSMF in the "continuity bursty" SFH model produces a shallower slope than the other models. Crucially, we can see that the derived GSMFs are in tension with each other, and do not typically fall within the confidence intervals across the majority of the stellar mass range. This is consistent with B. Wang et al. (2024a), who argue that the stellar mass uncertainties are typically underestimated by SED-fitting procedures.

The change in inferred stellar mass we observe with a modified IMF does not appear to vary strongly with stellar mass, so the the impact on the GSMF can generally be seen as a shift toward lower stellar mass of 0.3–0.4 dex. This is comparable in magnitude and opposite in direction to the shift seen when moving from `Bagpipes` to `Prospector` when using a parametric SFH, which results in little overall change in the resulting GSMF.

These results demonstrate the overall systematic uncertainty caused in the GSMF by different assumptions that are not represented by the uncertainty contours. Most GSMF estimates do not consider the overall uncertainty introduced by the assumptions of their modeling, which often dwarfs the statistical uncertainty in the fit itself. The variation in the derived GSMF can also significantly impact the implied SMD, as discussed in the next section.

6.5. Stellar Mass Density Evolution in the Early Universe

The growth of SMD in the early Universe is highly uncertain. Some observational studies (e.g., P. A. Oesch et al. 2014; M. Stefanon et al. 2021; C. J. Willott et al. 2024) have found a sharp decline in SMD at $z \geqslant 8$, whereas others see a flatter evolution (R. Bhatawdekar et al. 2019; S. Kikuchihara et al. 2020). On the theoretical side, P. A. Oesch et al. (2018) use dark matter halo evolutionary models to predict a deviation from the constant star formation efficiency (CSFE) model of P. Madau & F. Haardt (2015), which follows a significantly steeper slope at $z \geqslant 7$. A. Ferrara et al. (2023) have also recently presented a new model for the UV LF and SMF incorporating obscured star formation, as well as a lack of dust within high-z galaxies, that most closely matches our SMD results, despite predicting a steeper slope than we observe at $z > 9$.

Our results from our fiducial `Bagpipes` model fall between the predictions of P. Madau & F. Haardt (2015) and P. A. Oesch et al. (2018). We see a flatter evolution with redshift than predicted with P. A. Oesch et al. (2018), but an overall lower SMD than the CFSE model of P. Madau & F. Haardt (2015). For our other GSMF estimates at $z = 10.5$, shown in Figure 12, we find that $\rho_\star$ increases by up to 0.75 dex, which would bring it closer to the CSFE prediction of P. Madau & F. Haardt (2015). While we do not show the SMD scatter measured in other redshift bins, we typically see the same behavior at $z > 7$, with our fiducial `Bagpipes` SMD result producing lower $\rho_\star$ estimates than our alternative models. With our fiducial `Bagpipes` results, we see significant evolution of the GSMF between $z = 7$ and $z = 8$, with $\rho_\star$ decreasing by $\sim$0.85 dex. However, we see a significantly flatter evolution in the SMD derived from the "continuity bursty" model GSMF, with a decrease of only $\sim$0.4 dex across the same redshift range. This is due partly to the overall increase in stellar mass estimates observed with this SFH

model when compared to our fiducial model, as detailed in Section 4.3, but is also due to the scattering of the high-mass LRD galaxies between the $z = 7$ and $z = 8$ redshift bins caused by uncertain photo-z estimates, which significantly impacts the GSMF at higher stellar masses.

We see a good agreement between the integration of the star formation rate density of N. J. Adams et al. (2024), which uses the same sample, and our fiducial SMD results. There are very few JWST-era GSMF estimates to directly compare against, and so we have computed the inferred SMD based on the integral of the cosmic star formation rate density of other studies. We note, however, the numerous works showing the increased scatter in mass-to-light ratios observed due to bursty star formation (P. Santini et al. 2023; Y. Asada et al. 2024), which will impact the assumptions made to convert these UV luminosity densities into stellar mass densities.

In Figure 10, we show the overall SMD range we find when we use a different SED-fitting tool or SFH model (dotted red uncertainty). This is significantly larger than the statistical uncertainty in the SMD from our fiducial `Bagpipes` results. A change of up to 0.75 dex at $z \approx 10.5$ is possible when only the SED-fitting tool or SFH model is varied and the overall sample is unchanged. More significant variations are possible between the results of independent studies, which also have to consider differences in reduction, source detection, photo-z estimation, selection procedure, cosmic variance, and completeness corrections. Not accounting for the contribution of AGN to the observed photometry may cause overestimation of the SMD at high redshift (J. C. D'Silva et al. 2023).

The range of stellar mass densities possible with our alternative GSMF estimates at $z \sim 10.5$ is mostly above the 1σ range of N. J. Adams et al. (2024). A discrepancy between the integrated star formation rate density and SMD measured for the same sample could hint at a different IMF, since the assumed return fraction is strongly dependent on the chosen IMF, and the SMF and UVLF probe different stellar populations with different characteristic stellar mass. However, there are a number of other possible issues with the conversion of the UVLF into an SMD estimate. For example, the conversion of UV flux to SFR (κ_{UV}) is often assumed to be a constant factor, but it is actually dependent on the age and metallicity (P. Madau & M. Dickinson 2014), as well as the other assumptions used to calculate the return fraction (closed-box model, constant IMF and metal yield, and instantaneous recycling of metals), which may not be valid at high redshift.

As we show in Section 4.3, in some cases, discrimination between models or priors based on the goodness of fit may be possible, but in others (e.g., assumed SFH model), significant scatter in stellar mass estimates is possible with no difference in χ^2. Other studies that use only one method for measuring stellar mass estimates will underestimate the overall uncertainty in the derived GSMF and SMD estimates.

7. Conclusions

In this paper, we present an investigation into the properties of the EPOCHS v1 sample of 1120 high-redshift galaxies at $6.5 \leqslant z \leqslant 13.5$ taken from a uniform reduction of 187 arcmin^2 of JWST data, including the GTO program PEARLS as well as other public ERS/GO JWST programs.

We examine the consistency of galaxy properties, including stellar mass, under different assumptions and using different SED-fitting tools, including `Bagpipes` and `Prospector`. In

particular, we examine the impact of different SFH parameterizations as well as switching between a parametric and nonparametric SFH models. We also also investigate the possible reduction in stellar mass when assuming a top-heavy IMF. We then use this sample and our range of stellar mass estimates to construct possible realizations of the GSMF. Finally, we integrate our mass function estimates to probe the buildup of stellar mass in the early Universe via the SMD.

The major conclusions from this study are as follows:

1. We find that the stellar mass of high-redshift galaxies can depend strongly on assumed models, their priors, and the SED-fitting package used. In particular, the estimated stellar mass can increase by >1 dex when a parametric SFH is exchanged for a nonparametric SFH, with no change in the goodness of fit. Higher stellar mass discrepancies are seen at $z > 10$, due to a lack of rest-optical emission.

2. We find that the assumption of a modified top-heavy P. Kroupa (2001) IMF, which may more accurately model the hot star-forming regions within high-z galaxies, can reduce stellar mass estimates by up to 0.5 dex with no impact on the goodness of fit.

3. While some of the stellar mass estimates imply a high star formation efficiency, in our analysis of the most massive galaxies in our sample using the EVS methodology of C. C. Lovell et al. (2023), we do not find any galaxies that are incompatible with the existing ΛCDM cosmology. The largest stellar mass estimates are typically found when fitting the nonparametric SFH models, and often can be significantly reduced with an alternative model. We not require a top-heavy IMF

4. Across all of the fitted models, the highest-mass galaxies in our sample are "little red dots," with inferred masses of $>10^{10} \, M_\odot$ at $z \approx 7$. These galaxies dominate the highest-mass bins of our GSMF estimates, so understanding their true stellar populations and accounting for the likely contribution of AGN (L. J. Furtak et al. 2024, 2023c; J. E. Greene et al. 2024; C. C. Williams et al. 2024) will be essential to more accurately constrain further GSMF estimates.

5. With the GSMF derived from our fiducial `Bagpipes` results, we typically see good agreement with existing constraints on the GSMF at $z \leqslant 9.5$. At the limits of HST +Spitzer ($z \geqslant 10$), we see an excess of galaxies when compared to pre-JWST observations, but our GSMF results fall within predictions of simulations and theory.

6. The systematic variation in stellar mass estimates we find can dramatically impact the inferred GSMF and therefore the SMD. We show that the choice of SFH model or SED-fitting tool can cause up to a 0.75 dex shift in the overall SMD at $z \approx 10.5$ with the same sample of galaxies. We predict larger offsets between independent samples, where different reductions, selection techniques, and photo-z estimates will increase the uncertainties.

7. We see a flatter evolution of the cumulative SMD than predicted by dark matter halo evolution models, while the slope of our results is more consistent with CSFE models. Our results suggest that significant stellar mass had already formed at $z \geqslant 11.5$.

This is only the beginning of GSMF estimates at $z > 10$, and the use of ultra-deep observations (the second NGDEEP epoch

(M. B. Bagley et al. 2024), the JADES Origins Field (D. J. Eisenstein et al. 2023a; B. Robertson et al. 2024) and others) and magnification by lensing clusters (PEARLS, UNCOVER, and CANUCS; C. J. Willott et al. 2023a; R. A. Windhorst et al. 2023; R. Bezanson et al. 2024) will help constrain the GSMF at stellar masses below our completeness limit of $\sim 10^8 \, M_\odot$, while wide-field surveys (e.g., PRIMER, UNCOVER, and Cosmos-Webb; J. S. Dunlop et al. 2021; J. Kartaltepe et al. 2021; R. Bezanson et al. 2024) will add area and rare higher-mass sources. Deep MIRI F560W or F770W observations (e.g., the MIRI HUDF survey; H. U. Norgaard-Nielsen & P. G. Perez-Gonzalez 2017) will be crucial to provide better constraints on stellar mass estimates at these redshifts by extending the wavelength range further into the rest-frame optical, although the sensitivity of MIRI decreases rapidly with increasing wavelength (e.g., T. Wang et al. 2024). More complete NIRSpec coverage is also important to identify interlopers, confirm photometric redshifts, and distinguish between AGN emission and star-forming galaxies.

All of the raw JWST data used in this work are the same as used in N. J. Adams et al. (2024) and can be accessed via this MAST doi:10.17909/5h64-g193. All proprietary data from the PEARLS program will all become accessible over 2024. Catalogs for all high-z galaxies will be published with the EPOCHS I paper (C. J. Conselice et al. 2024). The fiducial GSMF and SMD results from this work are available on GitHub,[33] and results for our alternative models will be made available upon request.

---

[33] https://github.com/tHarvey303/EpochsIV

Appendix A
Effect of SED-fitting Assumptions on Derived SPS Quantities

Here, we give a more detailed comparison between our fiducial Bagpipes results and the alternative models discussed in Section 4.1. In Figure 13, we show the equivalent of Figure 1 for other derived parameters, in order to understand what drives the observed discrepancies in stellar mass between different models.
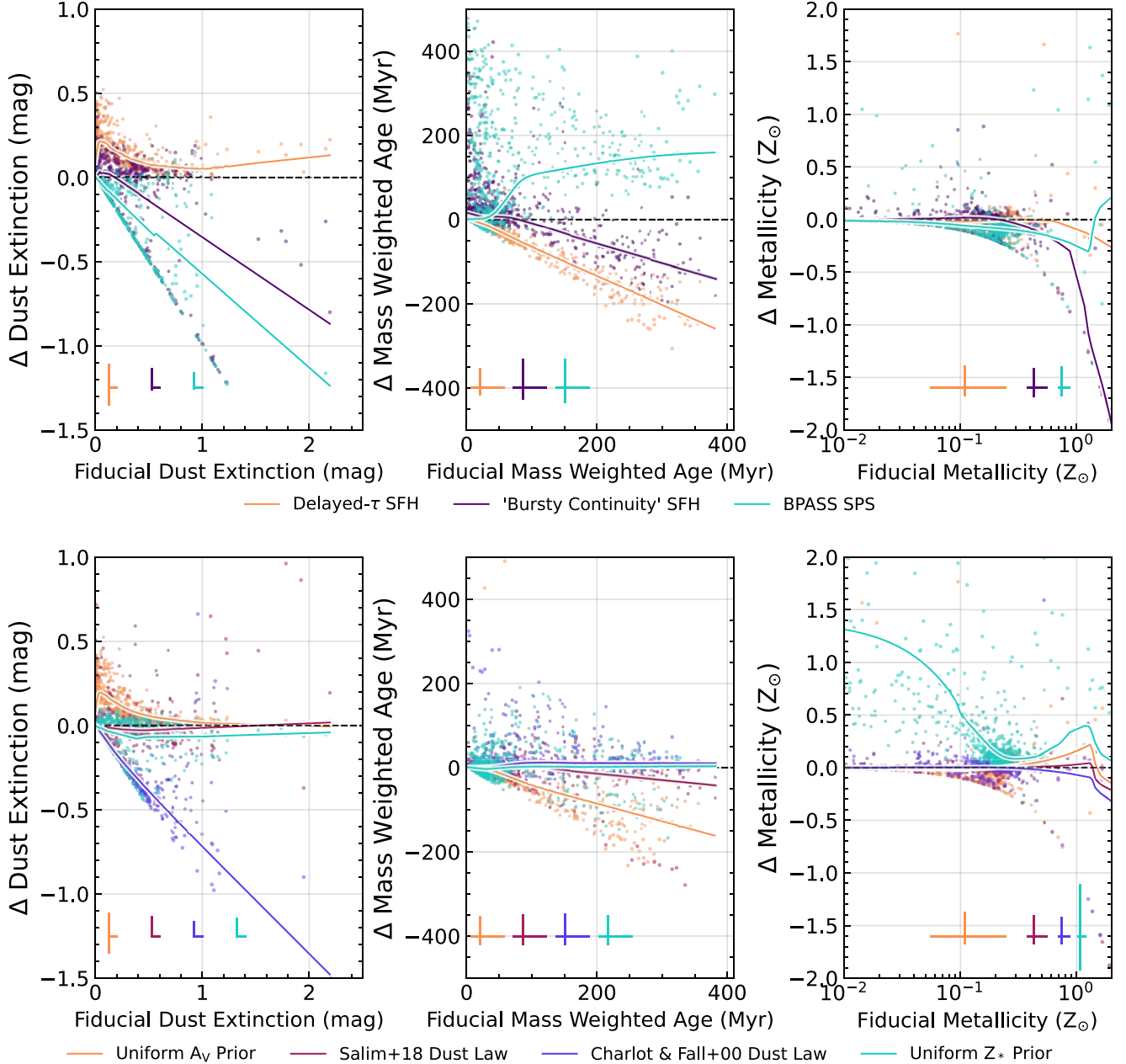

Figure 13. Comparison of the derived SPS parameters for our fiducial Bagpipes model when compared to the alternative models listed in Table 2. On the y-axis, we plot Δ = fiducial model − alternative model for the given parameter. From left to right, we show the dust extinction A_V, the mass-weighted age, and the stellar metallicity. The top row compares SFH and SPS models, while the bottom row considers the impact of priors and the chosen dust law. Average uncertainties are given in the bottom left of each point, and the LOWESS trend is shown with a line, where the color corresponds to the Bagpipes model.

A.1. Impact of Priors

The first comparison we make is a substitution of the default logarithmic prior on the V-band dust extinction, A_V, to a uniform prior. A uniform prior favors higher dust extinctions, and the largest difference to the fiducial model is seen in galaxies with $A_{V,\mathrm{fid}} < 0.2$ mag, where the dust content is poorly constrained. We see good agreement in photo-z, along with a few extreme outliers, which is unsurprising given the informative redshift prior from EAZY-py we use. The stellar mass offset is shown in light blue in the top plot of Figure 1 and shows good agreement within the posterior uncertainties. Galaxies with higher levels of dust are found to be significantly younger and more star-forming with a uniform dust prior, as can been seen in Figure 13, suggesting the inferred SFHs are dependent on the dust prior. Figure 13 also shows that the measured dust extinction, which is influenced by the prior, is primarily at $A_V < 0.3$, with both models agreeing on the dust extinction for the galaxies with higher dust extinction. Comparison of the best-fitting χ^2 values shows that both models are equally well-fitted to the photometry.

We also test the impact of our metallicity prior, which is logarithmic in our fiducial Bagpipes model. This favors low metallicity, which we expect in the early Universe. Here, we exchange this prior for a uniform distribution that favors higher metallicity, shown in orange in the top plot of Figure 1. We see little overall impact on the stellar mass from the metallicity prior, with individual galaxies scattering up to 0.5 dex and the majority consistent with results from our fiducial Bagpipes run. The metallicity itself, which is extremely difficult to constrain from photometry, is highly influenced by the prior chosen, as can be seen in Figure 13, although this does not appear to systematically impact the SFH or dust extinction.

Overall, the impact of the dust and metallicity priors alone appears to have only a small systematic effect on the derived galaxy masses. However, in a small number of individual cases, masses can scatter by ~ 0.5 dex with little difference in the goodness of fit.

A.2. The Assumed Dust Law

Our fiducial Bagpipes model assumes a simple one-component D. Calzetti et al. (2000) dust law. The slope of the dust law is known to vary in some galaxies, and numerous alternative models (e.g., S. Charlot & S. M. Fall 2000; S. Salim et al. 2018) including additional parameters have been suggested. S. Charlot & S. M. Fall (2000) fit a two-component dust law, with different amounts of extinction for young ($\leqslant 10$ Myr) and old stellar populations, to account for dust in stellar birth clouds. The resultant deviations in stellar mass are shown in magenta in the top plot of Figure 1, with a significant deviation at the highest stellar masses, which can be seen in the LOWESS trend. For galaxies with a fiducial stellar mass of $\geqslant 10^{10} M_\odot$, the majority are found to have $\geqslant 1$ dex larger stellar masses with the S. Charlot & S. M. Fall (2000) dust law. However, for these galaxies, the goodness of fit is considerably poorer, with $\Delta \chi^2 \geqslant 10$ with the S. Charlot & S. M. Fall (2000) model.

Despite the same prior, the dust attenuation (A_V) posteriors are quite different between the two models, due to the degeneracy between A_V and slope, as can be seen in Figure 13. Galaxies with moderate dust extinction in the fiducial results ($\leqslant 1$ mag) are typically found to have very little

dust extinction on the old stellar population, with higher dust extinction on the young stellar populations. The majority of galaxies favor a steeper slope (n) for the attenuation power law than given by D. Calzetti et al. (2000), in this mode with a distribution centered on $n \approx 1.3$, which is 2σ from the prior value of 0.70.

S. Salim et al. (2018) allow a deviation in slope compared to the D. Calzetti et al. (2000) and an additional UV bump at 2175 Å. The UV bump in the S. Salim et al. (2018) model is driven primarily by Polycyclic Aromatic Hydrocarbon emission, which is expected when emission is strongly reprocessed. We replace the D. Calzetti et al. (2000) dust law with the S. Salim et al. (2018) model, and fit for these additional components, as shown in Table 2. We find that the inferred stellar mass can increase by >1 dex in some cases, in particular at the highest fiducial stellar mass, but the average offset (see the LOWESS fit in Figure 1) is smaller than for the S. Charlot & S. M. Fall (2000) case. In a number of cases, the goodness of fit for the S. Salim et al. (2018) model is considerably better than our fiducial model, with $\delta \chi^2 \leqslant -10$ in a number of galaxies.

A.3. Comparison to "Delayed" SFH

To test the consistency of galaxy stellar mass estimates with different parametric SFHs, we replace our "log-normal" SFH with another commonly used SFH; a delayed-τ SFH. We find systematically slightly lower stellar masses above $10^8 M_\odot$, but reasonable agreement at the lowest stellar masses. This is likely due to the log-uniform prior on age used in the delayed-τ model, which results in a systematically younger stellar population, as can be seen in Figure 13. We also see some impact on the dust attenuation, likely driven by the change in inferred SFH, with systematically higher dust attenuation inferred with this SFH. Comparison of the goodness of fit via the χ^2 parameter suggests the models typically have slightly poorer fits than the fiducial model, but in some cases the stellar masses are reduced by ~ 0.5 dex with very little impact on the goodness of fit.

A.4. Comparison to "Continuity Bursty" SFH

Here, we replace our fiducial Bagpipes "log-normal" SFH with a "continuity bursty" SFH model described in detail in Section 4.1. We reproduce the result of S. Tacchella et al. (2022) that this SFH increases the galaxy stellar mass, finding an average increase of 0.2 dex. The stellar mass discrepancy between the two models is shown in purple in the lower figure of 1. In individual cases, the increase in stellar mass can reach ≈ 1 dex, with only small changes in photo-z. The largest offsets in stellar mass are typically seen for galaxies with a fiducial stellar mass of $10^8 M_\odot$, with the highest fiducial stellar mass galaxies ($\geqslant 10^{10} M_\odot$) seeing considerably smaller increases.

We see the largest discrepancies in stellar mass between the two models when the χ^2 significantly favors the fiducial model, suggesting the higher stellar mass estimate of the "continuity bursty" model may not be accurate in these cases. However, there are a small number of galaxies in which the offset exceeds 1 dex with minimal χ^2 difference, and even a few galaxies where the offset exceeds 0.5 dex and the "continuity bursty" model is significantly preferred. An example of the discrepancy between the stellar mass PDFs of our fiducial and the "continuity bursty" model can be seen for the individual

galaxy SED of JADES-Deep-GS:9075 shown in Figure 3, where there is a 1.3 dex difference between the stellar mass estimates, with only a difference of $\Delta\chi^2 = 0.2$ between the two solutions.

Star formation rates (SFRs) are typically higher; however, the model does not reproduce the highest SFR estimates of the fiducial model. Individual inspection of these highly star-forming galaxies show that the "continuity bursty" model struggles to reproduce SFRs high enough to match the measured Hβ+[O III] equivalent widths inferred from the photometry. Despite the greater flexibility (and number of fitted parameters), the "continuity bursty" model has a higher χ^2 than our fiducial model for the majority of galaxies. This may suggest that the fitting procedure is struggling to accurately constrain the SFH in the nonparametric case.

Looking at the other derived properties in Figure 13, we also see significant scatter in dust extinction, where the galaxies with the highest extinctions in our fiducial model are found to contain significantly less dust with this SFH model. For galaxies older than 50 Myr in our fiducial model, they are typically found to be systematically younger with this nonparametric SFH, but some of the youngest galaxies in the fiducial model are found to be much older.

A.5. Comparison to BPASS SPS Models

By default, Bagpipes uses the 2016 version of the G. Bruzual & S. Charlot (2003, hereafter BC03) stellar population synthesis (SPS) models. However Bagpipes can also employ Binary Population and Spectral Synthesis (BPASS; E. R. Stanway & J. J. Eldridge 2018) models. Specifically, we use models generated with v2.2.1 of BPASS, with the default IMF (slope of 1.35, 300 $M_\star$). The IMF parameterization of this SPS model differs slightly from the P. Kroupa (2001) IMF used in the BC03 models, causing an intrinsic offset in stellar mass. However as shown in orange in the lower plot of Figure 1, the comparison of the mass estimates is more complex. At the lowest and highest stellar masses ($\log_{10} M_\star/M_\odot \leqslant 7.5$ and $\log_{10} M_\star/M_\odot \geqslant 10$), we see systematically lower stellar masses than in the fiducial Bagpipes model, which is what we would expect based the IMF difference alone. However, for the majority of the sample, which falls between these two mass extremes, we see a significantly larger offset in stellar masses, which increases with redshift, as shown by the LOWESS trend.

The SFRs and redshifts are broadly correlated, with some outliers. However, the ages show a large scatter, and higher mass-weighted ages (MWA) are preferred in the majority of cases when using BPASS, which may be more reasonable than the young ages ($\langle$MWA$\rangle \sim 20$ Myr) inferred with our fiducial Bagpipes results. In particular, a significant subset of galaxies are found to have a $\geqslant 2$ dex shift in mass-weighted age.

The best-fit χ^2 shows some scatter, where fits with low χ^2 in the fiducial Bagpipes results typically have a similar or worse fit, but some galaxies with higher χ^2 have significantly improved. For these galaxies with improved χ^2 ($\Delta\chi^2 > 5$), the main difference is that the best-fitting SED reproduces the observed rest-UV fluxes more closely. Interestingly, this subset of galaxies with significantly improved χ^2 also typically have considerably higher MWA using BPASS than BC03, with their recreated SFHs suggesting a constant SFH, rather than the recent burst preferred when fitting with the BC03 SPS models.

In Figure 13, we also see the significant impact the BPASS SPS model has on the derived dust extinction, age, and metallicity. Despite using the same prior and dust model, when the BPASS SPS model is used, the dust extinction A_V is systematically much lower, often inferring essentially no dust extinction. Galaxy ages are also found to be systematically much larger, often by $\geqslant 100$ Myr.

A.6. Other Comparisons

Numerous other Bagpipes models were tested, and we have presented in detail the results of a subset of them above. Here, we summarize the effects of a few other variations that we do not include in Figure 1.

1. Fixed redshift to EAZY-py max $P(z)$: Little overall effect on stellar masses or star formation rates, with some individual scatter. This is the expected behavior, as the majority of redshifts are consistent within the EAZY-py posterior uncertainty, given that we use this as a prior in our fiducial model.

2. "Continuity" nonparametric SFH model: This variation tests the other nonparametric SFH model introduced in J. Leja et al. (2019) and S. Tacchella et al. (2022), which more tightly constrains the SFR in neighboring time bins to force more smoothly varying SFHs than the "continuity bursty" model. We find overall similar behavior to the "continuity bursty" model, with systematically higher masses and higher mass-weighted age. The models typically have worse χ^2 statistics than the "continuity bursty" model fits potentially indicating that more stochastic SFHs are preferred for the majority of galaxies, as suggested in the literature (C.-A. Faucher-Giguère 2018; R. Endsley et al. 2023b; T. J. Looser et al. 2023; Y. Asada et al. 2024).

A.7. Comparison to Prospector

In this section, we compare our fiducial Bagpipes model to our results from Prospector. Figure 14 shows a comparison of the stellar masses derived from Bagpipes and Prospector. We compare our "fiducial" Bagpipes model, as described in Section 4.1, to our parametric SFH Prospector model. These models are generally similar with a few key differences, but both provide a baseline for comparison to our other models. We also compare our nonparametric SFH models to each other, and they both employ the same "continuity bursty" SFH with the same time bins and priors. We use the same P. Kroupa (2001) IMF for both Bagpipes and Prospector, so we do not expect any different in stellar mass estimates due to the IMF parameterization.

For the comparison of the parametric SFH models (delayed-τ for Prospector and log-normal for Bagpipes), we see systematically larger photo-z and stellar mass estimates with Prospector. While in the Prospector model we allow the IGM attenuation to vary, which could impact photo-z estimates, we do not see the same offset with the nonparametric SFH model, where the IGM attenuation is also allowed to vary. Both SED-fitting tools are given the same redshift prior from EAZY-py. For both example galaxy SEDs in Figure 3, Prospector prefers higher-z solutions than Bagpipes, because it is inferring the presence of Lyα emission. While Lyα emitters have been found at $z \geqslant 9$ (e.g., A. J. Bunker et al. 2023), we do not expect to observe Lyα from the majority of galaxies at these redshifts, due to the attenuation from neutral
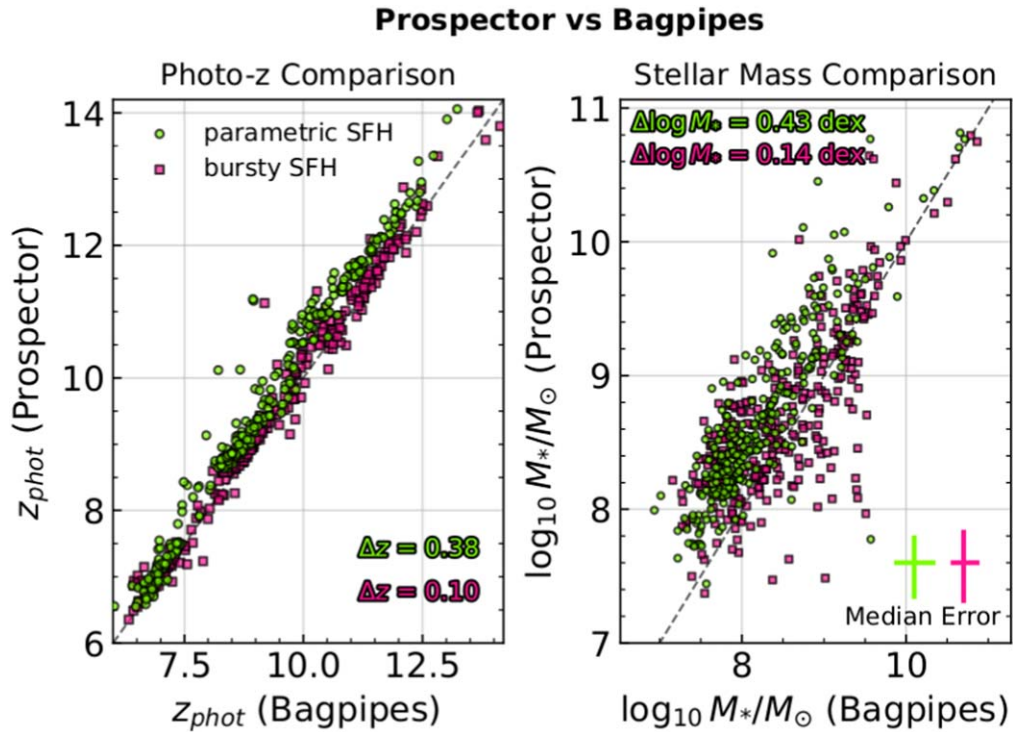
Prospector vs Bagpipes

Figure 14. (Top) Comparison of redshift estimates between `Bagpipes` and `Prospector`, both with the same Gaussian photo-z prior from `EAZY-py`. Photo-z estimates are systematically larger in `Prospector` when comparing the parametric SFH models. Median photo-z offset for each model is shown on the plot. (Bottom) Comparison of derived stellar mass estimates between `Prospector` and `Bagpipes` for both parametric and nonparametric SFH models. Median stellar mass offset is shown on the plot, as is the average uncertainty for both stellar mass estimates.

hydrogen during the Epoch of Reionization, and a systematic photo-z offset from `Prospector` is likely for galaxies without Lyα emission. However, given that we see a photo-z offset primarily for the "parametric SFH" only, Lyα emission is unlikely to be the only cause of the offset, as the `Prospector` SEDs in Figure 3 show Lyα emission for both SFH models. This offset will generally cause a slight increase in stellar mass estimates, as a more distant galaxy must be intrinsically brighter. We see a median increase of 0.43 dex in stellar mass.

For the "continuity bursty" SFH models, we see better agreement in redshift, with a median offset of only $\delta z = 0.1$. Stellar mass estimates are also more consistent on average, although we see large scatter, with individual mass differences reaching ≈ 1.5 dex.

We typically see comparable χ^2 values for both the parametric and nonparametric `Prospector` SFH models, in contrast to the result with `Bagpipes`. It is possible that the nested sampling with `dynesty` in `Prospector` provides a more robust constraint on the binned SFH than the nested sampling in `Bagpipes`, and this may warrant further investigation.

Appendix B
$z = 7$ Stellar Mass Function Without "Little Red Dots"

As discussed in Section 6.2, the LRDs dominate the high-mass end of our GSMF at $z = 7$. As the contribution of AGN to their photometry is still somewhat uncertain and likely differs on an individual basis between galaxies, in the main results of this paper we do not remove LRDs from the GSMF estimates or account for any possible AGN emission. In this appendix, we briefly present the alternative case, where we remove all
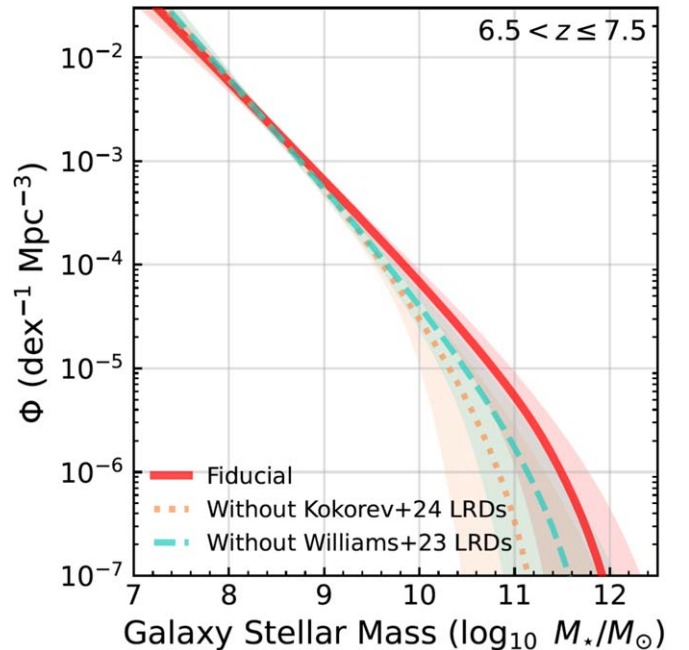

Figure 15. Galaxy Stellar Mass Function at $6.5 < z \leqslant 7.5$, excluding all "little red dots," compared to our fiducial `Bagpipes` results. We differentiate between the selections of V. Kokorev et al. (2024) and C. C. Williams et al. (2024), which differ primarily by the strength of the F277W – F444W color required to characterize a galaxy as a "little red dot."

objects that meet the color–color selection criteria of V. Kokorev et al. (2024) and reconstruct the $z = 7$ GSMF.

When we apply their "*red2*" color selection, compactness criterion and SNR requirements to our robust sample, we find 34

galaxies that meet these cuts. There are 13 in the NEP-TDF, 17 in CEERS, 3 in the JADES DR1 field, and 1 in the NGDEEP field. The median redshift is 7.16, with all candidates falling between $z = 6.5$ (our redshift cut) and $z = 8.7$. The median fiducial `Bagpipes` stellar mass is $\log_{10} M_\star/M_\odot = 8.90$, with a maximum stellar mass of $\log_{10} M_\star/M_\odot = 10.70$.

We exclude these 34 candidates from our sample and reconstruct the stellar mass function at $z = 7$. No other changes are made to our GSMF construction or fitting procedures. Figure 15 shows the GSMF derived without including any "little red dots," following the cut of V. Kokorev et al. (2024). Compared to the fiducial GSMF, this removes the two highest-mass bins entirely, which demonstrates our reliance on these galaxies at the high-mass regime. In terms of the derived Schechter parameters, the exponential mass cutoff $M^\star$, which is not well constrained, decreases from $11.57^{+0.63}_{-0.85}$ to $10.64^{+1.25}_{-0.98}$ when we exclude the LRDs. The median posterior $\phi^\star$ and α for the GSMF without LRDs are $-5.40^{+1.34}_{-1.43}$ and $-2.04^{+0.18}_{-0.13}$, respectively. We also test the more restrictive color cut of C. C. Williams et al. (2024), which requires a stronger

F277W – F444W color criterion in order to provide an 80% AGN purity (J. E. Greene et al. 2024). The majority of the LRDs we find above do not meet this criterion, with only 8/34 having F277W – F444W > 1.6 mag, but these LRDs with the reddest colors also typically have the highest inferred stellar masses, so excluding just these eight objects has a noticeable impact on the $z = 7$ GSMF, as shown in Figure 15.

Appendix C
Tabulated Schechter Parameters for Alternative GSMF Estimates at $z = 10.5$

We give the Schechter function parameters for our alternative GSMF fits at $z \sim 10.5$ in Table 6. These are the Schechter parameters representing the fits shown in Figure 12. These GSMF estimates are equivalent to the fits given in Table 3 for the fiducial GSMF, and are calculated using the same method—simply replacing the redshift and stellar mass PDF used in constructing the GSMF with those derived under the alternate SED-fitting assumptions.

Table 6
Schechter Function Parameters for the GSMF at $9.5 \leqslant z \leqslant 11.5$ for Each of the Alternative Models Shown in Figure 12

SED-fitting Tool	SFH Model	IMF	α	$M^\star$	$\log_{10} \phi^\star$
Bagpipes	"continuity bursty"	P. Kroupa (2001)	$-1.93^{+0.21}_{-0.16}(-1.80)$	$10.70^{+1.21}_{-1.06}(9.70)$	$-5.94^{+1.33}_{-1.28}(-4.70)$
Prospector	"continuity bursty"	P. Kroupa (2001)	$-1.72^{+0.26}_{-0.18}(-1.51)$	$10.51^{+1.34}_{-0.99}(9.54)$	$-5.57^{+1.13}_{-1.19}(-4.46)$
Prospector	delayed-τ	P. Kroupa (2001)	$-1.98^{+0.22}_{-0.17}(-1.89)$	$10.67^{+1.22}_{-1.07}(9.68)$	$-6.22^{+1.37}_{-1.35}(-4.98)$
Prospector	"continuity bursty"	HOT 45K	$-1.93^{+0.25}_{-0.20}(-1.81)$	$10.56^{+1.28}_{-1.10}(9.53)$	$-6.09^{+1.39}_{-1.39}(-4.83)$
Prospector	delayed-τ	HOT 45K	$-2.19^{+0.25}_{-0.22}(-2.18)$	$10.54^{+1.14}_{-1.10}(9.55)$	$-6.67^{+1.63}_{-1.45}(-5.31)$

Notes. For α, $M^\star$, and $\log_{10} \phi^\star$, we give both the median posterior and maximum likelihood values (in brackets). The details of the `Bagpipes` and `Prospector` configurations for each model are given in Sections 4.1 and 4.2.

Appendix D
$z = 12.5$ GSMF with No Contamination Limit

Our fiducial GSMF applies a 50% contamination limit on all galaxies. Given the fields a galaxy is selected in and its stellar mass, our JAGUAR contamination simulation computes a likelihood of contamination, based on simulated galaxies with the same stellar mass. The highest contamination is seen in the $z = 12.5$ GSMF, for the $10^{7.5} < M_\star/M_\odot \leqslant 10^{8.5}$ bin, and results in several galaxies being removed from our fiducial GSMF estimate. As the predictions of JAGUAR are uncertain at these redshifts, it is hard to judge how accurate our contamination predictions are. In Figure 16, we have recomputed the $z = 12.5$ GSMF with no contamination limit, which boosts the lower stellar mass bin by ~ 0.3 dex. This brings it closer to the predictions of the Z. Li et al. (2024) FFB model, which has higher star formation efficiency than most models. The FFB model shown is for $\epsilon_{\max} = 0.20$ specifically, and the models with higher SFE ($\epsilon_{\max} = 0.5$–1) overpredict the GSMF at this redshift compared to our observations. If our contamination is overestimated in this redshift bin, then the FFB model of Z. Li et al. (2024) or the DELPHI model of V. Mauerhofer & P. Dayal (2023) provide the closest predictions, suggesting high but not extreme star formation efficiency is required to produce the observed GSMF at this redshift.
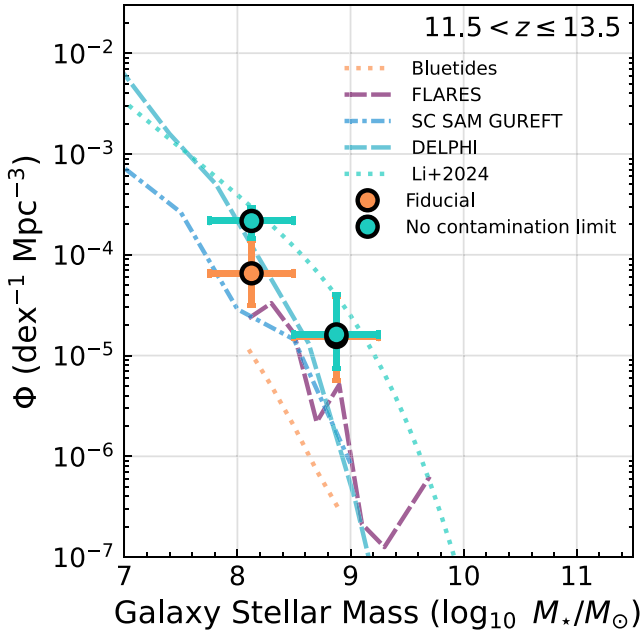
Figure 16. Galaxy stellar mass function at $11.5 < z \leqslant 13.5$ without a 50% contamination limit, compared to our fiducial Bagpipes results.

ORCID iDs

Thomas Harvey ⓘ https://orcid.org/0000-0002-4130-636X
Christopher J. Conselice ⓘ https://orcid.org/0000-0003-1949-7638
Nathan J. Adams ⓘ https://orcid.org/0000-0003-4875-6272
Duncan Austin ⓘ https://orcid.org/0000-0003-0519-9445
Ignas Juodžbalis ⓘ https://orcid.org/0009-0003-7423-8660
James Trussler ⓘ https://orcid.org/0000-0002-9081-2111
Qiong Li ⓘ https://orcid.org/0000-0002-3119-9003
Katherine Ormerod ⓘ https://orcid.org/0000-0003-2000-3420
Leonardo Ferreira ⓘ https://orcid.org/0000-0002-8919-079X
Christopher C. Lovell ⓘ https://orcid.org/0000-0001-7964-5933
Qiao Duan ⓘ https://orcid.org/0009-0009-8105-4564
Lewi Westcott ⓘ https://orcid.org/0009-0008-8642-5275
Honor Harris ⓘ https://orcid.org/0009-0005-0817-6419
Rachana Bhatawdekar ⓘ https://orcid.org/0000-0003-0883-2226
Dan Coe ⓘ https://orcid.org/0000-0001-7410-7669
Seth H. Cohen ⓘ https://orcid.org/0000-0003-3329-1337
Joseph Caruana ⓘ https://orcid.org/0000-0002-6089-0768
Cheng Cheng ⓘ https://orcid.org/0000-0003-0202-0534
Simon P. Driver ⓘ https://orcid.org/0000-0001-9491-7327
Brenda Frye ⓘ https://orcid.org/0000-0003-1625-8009
Lukas J. Furtak ⓘ https://orcid.org/0000-0001-6278-032X
Norman A. Grogin ⓘ https://orcid.org/0000-0001-9440-8872
Nimish P. Hathi ⓘ https://orcid.org/0000-0001-6145-5090
Benne W. Holwerda ⓘ https://orcid.org/0000-0002-4884-6756
Rolf A. Jansen ⓘ https://orcid.org/0000-0003-1268-5230
Anton M. Koekemoer ⓘ https://orcid.org/0000-0002-6610-2048
Madeline A. Marshall ⓘ https://orcid.org/0000-0001-6434-7845
Mario Nonino ⓘ https://orcid.org/0000-0001-6342-9662
Aswin P. Vijayan ⓘ https://orcid.org/0000-0002-1905-4194
Stephen M. Wilkins ⓘ https://orcid.org/0000-0003-3903-6935
Rogier Windhorst ⓘ https://orcid.org/0000-0001-8156-6281
Christopher N. A. Willmer ⓘ https://orcid.org/0000-0001-9262-9997
Haojing Yan ⓘ https://orcid.org/0000-0001-7592-7714
Adi Zitrin ⓘ https://orcid.org/0000-0002-0350-4488

References

Adams, N. J., Conselice, C. J., Austin, D., et al. 2024, ApJ, 965, 169
Adams, N. J., Conselice, C. J., Ferreira, L., et al. 2023, MNRAS, 518, 4755
Akins, H. B., Casey, C. M., Allen, N., et al. 2023, ApJ, 956, 61
Ananna, T. T., Bogdán, Á., Kovács, O. E., Natarajan, P., & Hickox, R. C. 2024, ApJL, 969, L18

Arrabal Haro, P., Dickinson, M., Finkelstein, S. L., et al. 2023a, Natur, 622, 707

Arrabal Haro, P., Dickinson, M., Finkelstein, S. L., et al. 2023b, ApJL, 951, L22

Asada, Y., Sawicki, M., Abraham, R., et al. 2024, MNRAS, 527, 11372

Astropy Collaboration, Price-Whelan, A. M., Lim, P. L., et al. 2022, ApJ, 935, 167

Astropy Collaboration, Price-Whelan, A. M., Sipőcz, B. M., et al. 2018, AJ, 156, 123

Astropy Collaboration, Robitaille, T. P., Tollerud, E. J., et al. 2013, A&A, 558, A33

Atek, H., Shuntov, M., Furtak, L. J., et al. 2023, MNRAS, 519, 1201

Austin, D., Adams, N., Conselice, C., et al. 2023, ApJL, 952, L7

Austin, D., Conselice, C. J., Adams, N. J., et al. 2024, arXiv:2404.10751

Bagley, M. B., Finkelstein, S. L., Koekemoer, A. M., et al. 2023a, ApJL, 946, L12

Bagley, M. B., Pirzkal, N., Finkelstein, S. L., et al. 2024, ApJL, 965, L6

Barro, G., Perez-Gonzalez, P. G., Kocevski, D. D., et al. 2024, ApJ, 963, 128

Behroozi, P., Wechsler, R. H., Hearin, A. P., & Conroy, C. 2019, MNRAS, 488, 3143

Behroozi, P. S., Wechsler, R. H., & Conroy, C. 2013, ApJ, 770, 57

Bertin, E., & Arnouts, S. 1996, A&AS, 117, 393

Bezanson, R., Labbe, I., Whitaker, K. E., et al. 2024, ApJ, 974, 92

Bhatawdekar, R., Conselice, C. J., Margalef-Bentabol, B., & Duncan, K. 2019, MNRAS, 486, 3805

Bhowmick, A. K., Di Matteo, T., Feng, Y., & Lanusse, F. 2018, MNRAS, 474, 5393

Bhowmick, A. K., Somerville, R. S., Di Matteo, T., et al. 2020, MNRAS, 496, 754

Bouwens, R., Illingworth, G., Oesch, P., et al. 2023, MNRAS, 523, 1009

Bouwens, R. J., Illingworth, G. D., Oesch, P. A., et al. 2015, ApJ, 803, 34

Bouwens, R. J., Oesch, P. A., Labbé, I., et al. 2016, ApJ, 830, 67

Bowler, R. A. A., Inami, H., Sommovigo, L., et al. 2024, MNRAS, 527, 5808

Bowman, J. D., Rogers, A. E. E., Monsalve, R. A., Mozdzen, T. J., & Mahesh, N. 2018, Natur, 555, 67

Boylan-Kolchin, M. 2023, NatAs, 7, 731

Bradač, M., Ryan, R., Casertano, S., et al. 2014, ApJ, 785, 108

Bradley, L., Sipőcz, B., Robitaille, T., et al. 2022, astropy/photutils: 1.5.0, v1.5.0, Zenodo, doi:10.5281/zenodo.6825092

Brammer, G. B., van Dokkum, P. G., & Coppi, P. 2008, ApJ, 686, 1503

Brinchmann, J., & Ellis, R. S. 2000, ApJL, 536, L77

Brown, A. G., Vallenari, A., Prusti, T., et al. 2021, A&A, 649, A1

Bruzual, G., & Charlot, S. 2003, MNRAS, 344, 1000

Buchner, J. 2014, A&A, 564, A125

Bundy, K., Ellis, R. S., Conselice, C. J., et al. 2006, ApJ, 651, 120

Bunker, A. J., Cameron, A. J., Curtis-Lake, E., et al. 2024, A&A, 690, A288

Bunker, A. J., Saxena, A., Cameron, A. J., et al. 2023, A&A, 677, A88

Bushouse, H., Eisenhamer, J., Dencheva, N., et al. 2022, JWST Calibration Pipeline, v1.8.2, Zenodo, doi:10.5281/zenodo.7325378

Calzetti, D., Armus, L., Bohlin, R. C., et al. 2000, ApJ, 533, 682

Cameron, A. J., Katz, H., Witten, C., et al. 2024, MNRAS, 534, 523

Caputi, K. I., Ilbert, O., Laigle, C., et al. 2015, ApJ, 810, 73

Carnall, A., Cullen, F., McLure, R., et al. 2024, MNRAS, 534, 325

Carnall, A. C., Leja, J., Johnson, B. D., et al. 2019, ApJ, 873, 44

Carnall, A. C., McLure, R. J., Dunlop, J. S., & Davé, R. 2018, MNRAS, 480, 4379

Casey, C. M., Akins, H. B., Shuntov, M., et al. 2024, ApJ, 965, 98

Castellano, M., Fontana, A., Treu, T., et al. 2022, ApJL, 938, L15

Chabrier, G., Baraffe, I., Allard, F., & Hauschildt, P. 2000, ApJ, 542, 464

Charlot, S., & Fall, S. M. 2000, ApJ, 539, 718

Chevallard, J., & Charlot, S. 2016, MNRAS, 462, 1415

Choi, J., Dotter, A., Conroy, C., et al. 2016, ApJ, 823, 102

Clauwens, B., Schaye, J., & Franx, M. 2016, MNRAS, 462, 2832

Cleveland, W. S. 1979, JASA, 74, 829

Conroy, C., & Gunn, J. E. 2010, ApJ, 712, 833

Conselice, C. J., Adams, N., Harvey, T., et al. 2024, arXiv:2407.14973

Cueto, E. R., Hutter, A., Dayal, P., et al. 2024, A&A, 686, A138

Cullen, F., McLure, R. J., McLeod, D. J., et al. 2023, MNRAS, 520, 14

Curti, M., D'Eugenio, F., Carniani, S., et al. 2023, MNRAS, 518, 425

Curtis-Lake, E., Carniani, S., Cameron, A., et al. 2023, NatAs, 7, 622

Davidzon, I., Ilbert, O., Laigle, C., et al. 2017, A&A, 605, A70

Davis, M., Guhathakurta, P., Konidaris, N. P., et al. 2007, ApJL, 660, L1

Desprez, G., Martis, N. S., Asada, Y., et al. 2024, MNRAS, 530, 2935

Dome, T., Tacchella, S., Fialkov, A., et al. 2024, MNRAS, 527, 2139

Donnan, C. T., McLeod, D. J., Dunlop, J. S., et al. 2023, MNRAS, 518, 6011

Dotter, A. 2016, ApJS, 222, 8

Drakos, N. E., Villasenor, B., Robertson, B. E., et al. 2022, ApJ, 926, 194

Dressler, A., Rieke, M., Eisenstein, D., et al. 2024, ApJ, 964, 150

Driver, S. P., Andrews, S. K., da Cunha, E., et al. 2018, MNRAS, 475, 2891

Driver, S. P., & Robotham, A. S. G. 2010, MNRAS, 407, 2131

D'Silva, J. C., Driver, S. P., Lagos, C. D., et al. 2023, ApJL, 959, L18

Duncan, K., Conselice, C. J., Mortlock, A., et al. 2014, MNRAS, 444, 2960

Dunlop, J. S., Abraham, R. G., Ashby, M. L. N., et al. 2021, PRIMER: Public Release IMaging for Extragalactic Research, JWST Proposal. Cycle 1, ID. #1837

Eddington, A. S. 1913, MNRAS, 73, 359

Eisenstein, D. J., Johnson, B. D., Robertson, B., et al. 2023a, arXiv:2310.12340

Eisenstein, D. J., Willott, C., Alberts, S., et al. 2023b, arXiv:2306.02465

Endsley, R., Stark, D. P., Chevallard, J., & Charlot, S. 2021, MNRAS, 500, 5229

Endsley, R., Stark, D. P., Lyu, J., et al. 2023a, MNRAS, 520, 4609

Endsley, R., Stark, D. P., Whitler, L., et al. 2023b, MNRAS, 524, 2312

Faucher-Giguère, C.-A. 2018, MNRAS, 473, 3717

Feng, Y., Di-Matteo, T., Croft, R. A., et al. 2016, MNRAS, 455, 2778

Ferland, G. J., Chatzikos, M., Guzmán, F., et al. 2017, RMxAA, 53, 385

Feroz, F., Hobson, M. P., & Bridges, M. 2009, MNRAS, 398, 1601

Ferrara, A., Pallottini, A., & Dayal, P. 2023, MNRAS, 522, 3986

Ferreira, L., Adams, N., Conselice, C. J., et al. 2022, ApJL, 938, L2

Ferreira, L., Conselice, C. J., Sazonova, E., et al. 2023, ApJ, 955, 94

Finkelstein, S. L., Bagley, M. B., Ferguson, H. C., et al. 2023, ApJL, 946, L13

Finkelstein, S. L., Bagley, M., Song, M., et al. 2022, ApJ, 928, 52

Finkelstein, S. L., Leung, G. C. K., Bagley, M. B., et al. 2024, ApJL, 969, L2

Foreman-Mackey, D., Hogg, D. W., Lang, D., & Goodman, J. 2013, PASP, 125, 306

Fujimoto, S., Arrabal Haro, P., Dickinson, M., et al. 2023b, ApJL, 949, L25

Fujimoto, S., Finkelstein, S. L., Burgarella, D., et al. 2023a, ApJ, 955, 130

Furlong, M., Bower, R. G., Theuns, T., et al. 2015, MNRAS, 450, 4486

Furtak, L. J., Atek, H., Lehnert, M. D., Chevallard, J., & Charlot, S. 2021, MNRAS, 501, 1568

Furtak, L. J., Labbé, I., Zitrin, A., et al. 2024, Natur, 628, 57

Furtak, L. J., Shuntov, M., Atek, H., et al. 2023b, MNRAS, 519, 3064

Furtak, L. J., Zitrin, A., Plat, A., et al. 2023c, ApJ, 952, L142

Gaia Collaboration, Brown, A. G. A., Vallenari, A., et al. 2018, A&A, 616, A1

Genel, S., Vogelsberger, M., Springel, V., et al. 2014, MNRAS, 445, 175

Giménez-Arteaga, C., Fujimoto, S., Valentino, F., et al. 2024, A&A, 686, A63

Giménez-Arteaga, C., Oesch, P. A., Brammer, G. B., et al. 2023, ApJ, 948, 126

Glazebrook, K., Nanayakkara, T., Schreiber, C., et al. 2024, Natur, 628, 277

Gottumukkala, R., Barrufet, L., Oesch, P., et al. 2024, MNRAS, 530, 966

Grazian, A., Castellano, M., Fontana, A., et al. 2012, A&A, 547, A51

Grazian, A., Fontana, A., Santini, P., et al. 2015, A&A, 575, A96

Greene, J. E., Labbe, I., Goulding, A. D., et al. 2024, ApJ, 964, 39

Griffiths, A., Conselice, C. J., Alpaslan, M., et al. 2018, MNRAS, 475, 2853

Grogin, N. A., Kocevski, D. D., Faber, S. M., et al. 2011, ApJS, 197, 35

Gunawardhana, M. L. P., Hopkins, A. M., Sharp, R. G., et al. 2011, MNRAS, 415, 1647

Hainline, K. N., Helton, J. M., Johnson, B. D., et al. 2024b, ApJ, 964, 66

Hainline, K. N., Johnson, B. D., Robertson, B., et al. 2024a, ApJ, 964, 71

Harikane, Y., Ouchi, M., Oguri, M., et al. 2023, ApJS, 265, 5

Harikane, Y., Ouchi, M., Ono, Y., et al. 2016, ApJ, 821, 123

Haslbauer, M., Kroupa, P., Zonoozi, A. H., & Haghi, H. 2022, ApJL, 939, L31

Hoffmann, S. L., Mack, J., Avila, R., et al. 2021, AAS Meeting, 53, 216.02

Hopkins, P. F., Hernquist, L., Cox, T. J., et al. 2005, ApJ, 630, 716

Hunter, J. D. 2007, CSE, 9, 90

Illingworth, G., Magee, D., Bouwens, R., et al. 2016, arXiv:1606.00841

Jaacks, J., Finkelstein, S. L., & Bromm, V. 2019, MNRAS, 488, 2202

Jain, S., Tacchella, S., & Mosleh, M. 2024, MNRAS, 527, 3291

Jansen, R. A., & Windhorst, R. A. 2018, PASP, 130, 124001

Jermyn, A. S., Steinhardt, C. L., & Tout, C. A. 2018, MNRAS, 480, 4265

Jespersen, C. K., Steinhardt, C. L., Somerville, R. S., & Lovell, C. C. 2024, arXiv:2403.00050

Jeřábková, T., Hasani Zonoozi, A., Kroupa, P., et al. 2018, A&A, 620, A39

Johnson, B., Foreman-Mackey, D., Sick, J., et al. 2024, dfm/python-fsps: v0.4.7, Zenodo, doi:10.5281/zenodo.12447779

Johnson, B. D., Leja, J., Conroy, C., & Speagle, J. S. 2021, ApJS, 254, 22

Kartaltepe, J., Casey, C. M., Bagley, M., et al. 2021, COSMOS-Webb: The Webb Cosmic Origins Survey, JWST Proposal. Cycle 1, ID. #1727

Katz, H., Rosdahl, J., Kimm, T., et al. 2022, MNRAS, 510, 5603

Kikuchihara, S., Ouchi, M., Ono, Y., et al. 2020, ApJ, 893, 60

Kocevski, D. D., Onoue, M., Inayoshi, K., et al. 2023, ApJL, 954, L4

Koekemoer, A. M., Faber, S. M., Ferguson, H. C., et al. 2011, ApJS, 197, 36

Kokorev, V., Caputi, K. I., Greene, J. E., et al. 2024, ApJ, 968, 38

Kroupa, P. 2001, MNRAS, 322, 231
Kroupa, P. 2002, Sci, 295, 82
Labbe, I., Greene, J. E., Bezanson, R., et al. 2023, arXiv:2306.07320
Labbé, I., van Dokkum, P., Nelson, E., et al. 2023, Natur, 616, 266
Laigle, C., McCracken, H. J., Ilbert, O., et al. 2016, ApJS, 224, 24
Langeroodi, D., Hjorth, J., Chen, W., et al. 2023, ApJ, 957, 39
Larson, R. L., Finkelstein, S. L., Kocevski, D. D., et al. 2023, ApJL, 953, L29
Larson, R. L., Hutchison, T. A., Bagley, M., et al. 2023, ApJ, 958, 141
Laseter, I. H., Maseda, M. V., Curti, M., et al. 2024, A&A, 681, A70
Leja, J., Carnall, A. C., Johnson, B. D., Conroy, C., & Speagle, J. S. 2019, ApJ, 876, 3
Leja, J., Johnson, B. D., Conroy, C., & van Dokkum, P. 2018, ApJ, 854, 62
Leung, G. C. K., Bagley, M. B., Finkelstein, S. L., et al. 2023, ApJL, 954, L46
Li, Z., Dekel, A., Sarkar, K. C., et al. 2024, A&A, 690, A108
Looser, T. J., D'eugenio, F., Maiolino, R., et al. 2023, arXiv:2306.02470
Lovell, C. C., Harrison, I., Harikane, Y., Tacchella, S., & Wilkins, S. M. 2023, MNRAS, 518, 2511
Lovell, C. C., Vijayan, A. P., Thomas, P. A., et al. 2021, MNRAS, 500, 2127
Lower, S., Narayanan, D., Leja, J., et al. 2020, ApJ, 904, 33
Lynden-Bell, D. 1971, MNRAS, 155, 95
Ma, X., Hopkins, P. F., Garrison-Kimmel, S., et al. 2018, MNRAS, 478, 1694
Madau, P. 1995, ApJ, 441, 18
Madau, P., & Dickinson, M. 2014, ARA&A, 52, 415
Madau, P., & Haardt, F. 2015, ApJL, 813, L8
Maiolino, R., Risaliti, G., Signorini, M., et al. 2024, arXiv:2405.00504
Marley, M., Saumon, D., Morley, C., et al. 2021, ApJ, 920, 85
Mason, C. A., Trenti, M., & Treu, T. 2023, MNRAS, 521, 497
Matthee, J., Naidu, R. P., Brammer, G., et al. 2024, ApJ, 963, 129
Mauerhofer, V., & Dayal, P. 2023, MNRAS, 526, 2196
McLeod, D. J., Donnan, C. T., McLure, R. J., et al. 2024, MNRAS, 527, 5004
Menanteau, F., Hughes, J. P., Sifón, C., et al. 2012, ApJ, 748, 7
Morishita, T., Stiavelli, M., Chary, R.-R., et al. 2024, ApJ, 963, 9
Mortlock, A., Conselice, C., Hartley, W. G., et al. 2015, MNRAS, 447, 2
Mortlock, A., Conselice, C. J., Bluck, A. F. L., et al. 2011, MNRAS, 413, 2845
Moster, B. P., Somerville, R. S., Maulbetsch, C., et al. 2010, ApJ, 710, 903
Moster, B. P., Somerville, R. S., Newman, J. A., & Rix, H.-W. 2011, ApJ, 731, 113
Mowla, L., Iyer, K., Asada, Y., et al. 2024, arXiv:2402.08696
Mutch, S. J., Geil, P. M., Poole, G. B., et al. 2016, MNRAS, 462, 250
Naidu, R. P., Oesch, P. A., Setton, D. J., et al. 2022a, arXiv:2208.02794
Naidu, R. P., Oesch, P. A., van Dokkum, P., et al. 2022b, ApJL, 940, L14
Nanayakkara, T., Glazebrook, K., Jacobs, C., et al. 2023, ApJL, 947, L26
Narayanan, D., Lower, S., Torrey, P., et al. 2024, ApJ, 961, 73
Navarro-Carrera, R., Rinaldi, P., Caputi, K. I., et al. 2024, ApJ, 961, 207
Noboriguchi, A., Inoue, A. K., Nagao, T., Toba, Y., & Misawa, T. 2023, ApJL, 959, L14
Norgaard-Nielsen, H. U., & Perez-Gonzalez, P. G. 2017, The MIRI HUDF Deep Imaging Survey, JWST Proposal. Cycle 1, ID. #1283
O'Brien, R., Jansen, R. A., Grogin, N. A., et al. 2024, ApJS, 272, 19
Oesch, P. A., Bouwens, R. J., Illingworth, G. D., Labbé, I., & Stefanon, M. 2018, ApJ, 855, 105
Oesch, P. A., Bouwens, R. J., Illingworth, G. D., et al. 2014, ApJ, 786, 108
Oke, J. B. 1974, ApJS, 27, 21
Oke, J. B., & Gunn, J. E. 1983, ApJ, 266, 713
Ormerod, K., Conselice, C. J., Adams, N. J., et al. 2024, MNRAS, 527, 6110
Papadopoulos, P. P., Thi, W.-F., Miniati, F., & Viti, S. 2011, MNRAS, 414, 1705
Papovich, C., Cole, J., Yang, G., et al. 2023, ApJL, 949, L18
Parashari, P., & Laha, R. 2023, MNRAS, 526, L63
Pérez-González, P. G., Barro, G., Annunziatella, M., et al. 2023, ApJL, 946, L16
Pérez-González, P. G., Barro, G., Rieke, G. H., et al. 2024, ApJ, 968, 4
Pérez-González, P. G., Costantin, L., Langeroodi, D., et al. 2023, ApJL, 951, L1
Perrin, M. D., Sivaramakrishnan, A., Lajoie, C.-P., et al. 2014, Proc. SPIE, 9143, 1174
Perrin, M. D., Soummer, R., Elliott, E. M., Lallo, M. D., & Sivaramakrishnan, A. 2012, Proc. SPIE, 8442, 1193
Planck Collaboration, Ade, P. A. R., Aghanim, N., et al. 2016, A&A, 594, A13
Pontoppidan, K. M., Barrientes, J., Blome, C., et al. 2022, ApJL, 936, L14
Popesso, P., Concas, A., Cresci, G., et al. 2023, MNRAS, 519, 1526
Retzlaff, J., Rosati, P., Dickinson, M., et al. 2010, A&A, 511, A50

Rieke, M. J., Kelly, D. M., Misselt, K., et al. 2023, PASP, 135, 028001
Rieke, M. J., Robertson, B., Tacchella, S., et al. 2023, ApJS, 269, 16
Roberts-Borsani, G. W., Bouwens, R. J., Oesch, P. A., et al. 2016, ApJ, 823, 143
Robertson, B., Johnson, B. D., Tacchella, S., et al. 2024, ApJ, 970, 31
Robertson, B. E., Tacchella, S., Johnson, B. D., et al. 2023, NatAs, 7, 611
Robotham, A. S. G., Norberg, P., Driver, S. P., et al. 2011, MNRAS, 416, 2640
Rowan-Robinson, M., & McCrea, W. H. 1968, MNRAS, 138, 445
Salim, S., Boquien, M., & Lee, J. C. 2018, ApJ, 859, 11
Salpeter, E. E. 1955, ApJ, 121, 161
Santini, P., Fontana, A., Castellano, M., et al. 2023, ApJL, 942, L27
Schaye, J., Crain, R. A., Bower, R. G., et al. 2015, MNRAS, 446, 521
Schechter, P. 1976, ApJ, 203, 297
Schlawin, E., Leisenring, J., Misselt, K., et al. 2020, AJ, 160, 231
Schmidt, M. 1968, ApJ, 151, 393
Shen, X., Vogelsberger, M., Boylan-Kolchin, M., Tacchella, S., & Kannan, R. 2023, MNRAS, 525, 3254
Sneppen, A., Steinhardt, C. L., Hensley, H., et al. 2022, ApJ, 931, 57
Song, M., Finkelstein, S. L., Ashby, M. L. N., et al. 2016, ApJ, 825, 5
Speagle, J. S. 2020, MNRAS, 493, 3132
Stanway, E. R., & Eldridge, J. J. 2018, MNRAS, 479, 75
Stark, D. P., Schenker, M. A., Ellis, R., et al. 2013, ApJ, 763, 129
Stefanon, M., Bouwens, R. J., Labbé, I., et al. 2017, ApJ, 843, 36
Stefanon, M., Bouwens, R. J., Labbé, I., et al. 2021, ApJ, 922, 29
Steinhardt, C. L., Jespersen, C. K., & Linzer, N. B. 2021, ApJ, 923, 8
Steinhardt, C. L., Kokorev, V., Rusakov, V., Garcia, E., & Sneppen, A. 2023, ApJL, 951, L40
Strait, V., Bradač, M., Coe, D., et al. 2020, ApJ, 888, 124
Suess, K. A., Weaver, J. R., Price, S. H., et al. 2024, ApJ, 976, 101
Tacchella, S., Finkelstein, S. L., Bagley, M., et al. 2022, ApJ, 927, 170
Tang, M., Stark, D. P., Chen, Z., et al. 2023, MNRAS, 526, 1657
Tomczak, A. R., Quadri, R. F., Tran, K.-V. H., et al. 2014, ApJ, 783, 85
Treu, T., Calabro, A., Castellano, M., et al. 2023, ApJL, 942, L28
Trussler, J. A., Adams, N. J., Conselice, C. J., et al. 2023, MNRAS, 523, 3423
Ulm, K. 1990, Am. J. Epidemiol., 131, 373
Vallenari, A., Brown, A., & Prusti, T. 2023, A&A, 674, A1
van Mierlo, S. E., Caputi, K. I., & Kokorev, V. 2023, ApJL, 945, L21
Virtanen, P., Gommers, R., Oliphant, T. E., et al. 2020, NatMe, 17, 261
Wang, B., de Graaff, A., Davies, R. L., et al. 2024b, arXiv:2403.02304
Wang, B., Fujimoto, S., Labbé, I., et al. 2023, ApJL, 957, L34
Wang, B., Leja, J., Atek, H., et al. 2024a, ApJ, 963, 74
Wang, T., Sun, H., Zhou, L., et al. 2024, arXiv:2403.02399
Weaver, J. R., Davidzon, I., Toft, S., et al. 2023, A&A, 677, A184
Weaver, J. R., Cutler, S. E., Pan, R., et al. 2024, ApJS, 270, 7
Weibel, A., Oesch, P. A., Barrufet, L., et al. 2024, MNRAS, 533, 1808
Weidner, C., Ferreras, I., Vazdekis, A., & La Barbera, F. 2013, MNRAS, 435, 2274
Whitaker, K. E., Ashas, M., Illingworth, G., et al. 2019, ApJS, 244, 16
Wilkins, S. M., Feng, Y., Di Matteo, T., et al. 2017, MNRAS, 469, 2517
Wilkins, S. M., Turner, J. C., Bagley, M. B., et al. 2023a, arXiv:2311.08065
Wilkins, S. M., Vijayan, A. P., Lovell, C. C., et al. 2023b, MNRAS, 519, 3118
Williams, C. C., Alberts, S., Ji, Z., et al. 2024, ApJ, 968, 34
Williams, C. C., Curtis-Lake, E., Hainline, K. N., et al. 2018, ApJS, 236, 33
Willott, C. J., Abraham, R. G., Asada, Y., et al. 2023, CANUCS: The CAnadian NIRISS Unbiased Cluster Survey, JWST Proposal. Cycle 3, ID. #4527
Willott, C. J., Desprez, G., Asada, Y., et al. 2024, ApJ, 966, 74
Windhorst, R. A., Cohen, S. H., Jansen, R. A., et al. 2023, AJ, 165, 13
Withers, S., Muzzin, A., Ravindranath, S., et al. 2023, ApJL, 958, L14
Woodroofe, M. 1985, AnSta, 13, 163
Woodrum, C., Rieke, M., Ji, Z., et al. 2023, arXiv:2310.18464
Xiao, M., Oesch, P., Elbaz, D., et al. 2024, Natur, 635, 311
Yan, H., Cohen, S. H., Windhorst, R. A., et al. 2023, ApJL, 2942, L8
Yan, H., Ma, Z., Ling, C., Cheng, C., & Huang, J.-S. 2023, ApJL, 942, L9
Yan, Z., Jeřábková, T., & Kroupa, P. 2021, A&A, 655, A19
Yang, L., Morishita, T., Leethochawalit, N., et al. 2022, ApJL, 938, L17
Yue, M., Eilers, A.-C., Ananna, T. T., et al. 2024, ApJL, 974, L26
Yung, L. Y. A., Somerville, R. S., Finkelstein, S. L., Wilkins, S. M., & Gardner, J. P. 2024, MNRAS, 527, 5929
Yung, L. Y. A., Somerville, R. S., Popping, G., et al. 2019, MNRAS, 490, 2855